Simulations Exploring Magnetic Fields in Spiral Galaxies

Simulations Exploring Magnetic Fields in Spiral Galaxies

By
HECTOR SMOOTHSTONE ROBINSON,
B.Sc., M.Sc.

A Thesis Submitted to the School of Graduate Studies
in the Partial Fulfillment of the Requirements for the Degree of

Doctor of Philosophy
in
Physics

McMaster University
Hamilton, Ontario

Doctor of Philosophy (2025)
Physics and Astronomy
McMaster University
Hamilton, Ontario, Canada

TITLE: Simulations Exploring Magnetic Fields in Spiral Galaxies

AUTHOR:
Hector Smoothstone Robinson,
B.Sc. (Physics), M.Sc. (Physics)

SUPERVISOR:
Dr. James Wadsley
Professor, Department of Physics and Astronomy,
McMaster University, ON, Canada

SUPERVISORY COMMITTEE CHAIR:
Dr. Willam Harris,
Professor, Department of Physics and Astronomy,
McMaster University, ON, Canada

SUPERVISORY COMMITTEE MEMBERS:
Dr. Ralph Pudritz
Professor, Department of Physics and Astronomy,
McMaster University, ON, Canada

Dr. Laura Parker
Professor, Department of Physics and Astronomy,
McMaster University, ON, Canada

Dr. Romain Teyssier
Professor, Department of Astrophysical Sciences,
Princeton University, NJ, USA

NUMBER OF PAGES: xi, 147

Abstract

Magnetism affects all scales in astrophysics because regular matter in the Universe is mostly ionized and couples to magnetic fields. Galaxy evolution entails many unanswered questions surrounding magnetic fields, including how they affect the flow and distribution of gas within the interstellar medium, how they affect the process of star formation, and how they evolve in a galactic environment. We investigate these questions through a series of isolated galaxy magnetohydrodynamic (MHD) simulations, which include additional physics such as stellar feedback, star formation, gas cooling and turbulence. To isolate the effects of the magnetic fields we use controlled setups that vary only the spiral nature of the galaxy and its initial magnetic fields.

We find that galaxies simulated with stronger magnetic fields have increased disk stability and reduced star formation rates compared to those without magnetic fields. Magnetic fields provide additional pressure that increases the scale height of the galactic disk. Secondly, we demonstrate the presence of several dynamos, including a novel galactic dynamo which is enabled by the presence of non-axisymmetric features such as bars and spiral arms. By simulating the same galaxy with and without spiral arms, we show that the galaxies can generate large-scale azimuthal fields whose amplification depends upon radial flows of gas. The presence of spiral arms also increases the overall amount of star formation in the galaxies, which in turn generates stronger fields through the turbulent dynamo. We show that the initial configuration of the fields does not affect the overall star formation rate, but does impact the transport of angular momentum, which can inhibit or promote the formation of a central bar and associated central star formation and field amplification.

Acknowledgements

First and foremost, I thank my advisor James Wadsley, for his patience, guidance and endless technical support throughout the years. James is a true expert in his field, and his common-sense approach has helped me become an effective researcher and communicator. I hope our paths continue to cross in the future.

To those on my advisory committees: Ralph Pudritz, Laura Parker and Alison Sills. Thank you for your guidance and assistance, I could not have accomplished this work without your help.

I would also like to thank the staff in the McMaster Department of Physics and Astronomy, specifically Rosemary McNeice and Jennifer Ayres, who have consistently gone above and beyond, and are not thanked often enough. I'm also grateful to the entire astronomy group at McMaster, they have created a welcoming yet research-intensive environment. I will greatly miss giving shows in the planetarium.

To my parents, thank you for your love, and for inspiring me to pursue higher education. To the rest of my family including the Robinsons, Marlows, and Mohameds, thank you for your continuous moral support.

Finally, to my beloved fiancé Selina. Thank you for everything. Your love, your patience, and your support. You inspire me everyday and I'm so excited to see what the future holds for us.

Contents

List of Figures

List of Tables

Declaration of Academic Achievement

I, Hector Smoothstone Robinson, declare that this thesis titled, **Simulations Exploring Magnetic Fields in Spiral Galaxies**, and works presented in it are my own. I confirm that

- Chapters 2, 3, and 4 present original research written by myself. I ran the simulations studied on supercomputing clusters, performed analysis of the simulation data, and created the figures presented. Throughout all of my work, my supervisor Dr. James Wadsley provided guidance on the direction and objectives of the research, in the interpretation of the results, and in the writing and editing process of the manuscripts.
- The work presented in Chapter 3 was done in collaboration with Dr. Jerry Sellwood and Dr. Ralph Pudritz, both of whom provided guidance on the direction and objectives of the research, in the interpretation of the results, and in the writing and editing process of the manuscripts. Dr. Jerry Sellwood also ran the simulations included in the appendix, and provided the initial conditions used in our simulations.

Chapter 1

Introduction

1.1 Magnetism in Astronomy

Since time immemorial, both magnetism and astronomy have been the subject of great curiosity. This thesis aims to combine them, by studying the magnetic fields embedded within spiral galaxies. Galaxies account for a sizeable minority of the baryonic matter in the Universe, and they are among the most easily observable, representing the peaks of structure formation. That baryonic matter exists as gas and stars which are caught in a consistent cycle of creation and destruction. Gas provides the raw material used in the creation of new stars, which shine for millions of years, but ultimately eject some of their material back into the surrounding space. That newly enriched material will then go on to form the next generation of stars. At every stage of this cycle, magnetic fields permeate the gas and stars, mediating the exchange of mass and energy within the interstellar medium (ISM). The modern understanding of the galactic life cycle requires many branches of physics, uses observations from state of the art telescopes, and employs novel computational techniques.

Galaxies have been observed for hundreds of years, but it wasn't until the 20th century that it became accepted they are independent objects outside of our own galaxy. In the past century, telescopes have improved dramatically, and have now produced high-resolution observations of galaxies across the entire electromagnetic spectrum and history of the Universe. This has revolutionized our understanding and produced a rich scientific literature on the study of galaxies. However, one thing that separates the study of astrophysical objects from other sciences is the absence of experiments. Astronomers cannot conduct an experiment on a galaxy, their analysis is limited to the light incident upon their telescope. Combined with the fact that galaxies change over hundreds of millions of years, this makes it difficult to understand galactic evolution.

Any observation of galaxy appears frozen in time, revealing only a single snapshot of its life-cycle. Together, this means that to study galactic evolution astronomers must make statistical connections in galaxy populations, which involves many assumptions. Another way around this is the use of numerical simulations to model the evolution of galaxies computationally. In this way computational astrophysicists play the role of experimentalists that is missing in galactic astronomy.

The systems studied in this thesis are late spiral galaxies which contain several distinct components. A dark matter halo, a stellar bulge, and a gas/stellar disk. The largest component of a galaxy is its dark matter halo. The dark matter accounts for roughly 80-90% of a galaxy's total mass, far outweighing the baryonic component. Although its precise nature remains unknown, dark matter interacts primarily through gravity, and dominates the gravitational potential of galaxies. The extended gravitational potential has important implications: they cause galaxies to rotate faster at large radii than expected from baryonic matter alone. In the current cosmological framework, ΛCDM (Blumenthal et al.; 1984), galaxies form and evolve within these dark matter halos through the hierarchical growth of structure, accretion of gas, and mergers with other galaxies. Embedded within the halo is the observable baryonic matter which has two main components, a disk and a bulge. The disk contains the majority of the cold gas and young stellar population, organized into spiral arms where star formation actively proceeds. The bulge, a centrally concentrated spheroidal component, is dominated by older stars and often hosts a supermassive black hole at its center. Within this galactic environment, several key physical processes govern the evolution: gravity drives the dynamics of the system, hydrodynamics controls the flow of gas, star formation converts gas into stars, stellar and black hole feedback redistribute energy in interstellar medium, and magnetic fields couple to the gas to influence dynamics on a wide range of scales. Each of these processes have nuanced interactions and require careful study, but this thesis concentrates on magnetic fields, and their interplay with other drivers of galaxy evolution.

1.1.1 An Observational Perspective on Galaxies

When viewing a populations of galaxies, it is immediately apparent that there is considerable variation in their properties. Galaxies come in a wide range of luminosity, colour, morphology, mass, size, and star formation rate (SFR). Perhaps the most fundamental property of galaxies are their mass, which range from roughly 10^7-10^{12} $M_\odot$, however even at a given mass there are galaxies with a wide range of other properties. Classically, galaxies were categorized based on their morphology using a system called the Hubble

Sequence (Hubble; 1926) that split galaxies into elliptical, spiral, and irregular types. At the time, elliptical and spiral galaxies were referred to as late-type and early-type respectively, but this language is misleading because ellipticals are actually an evolved state of spiral galaxies after they exhaust their star forming gas.

A more robust method of categorizing galaxies is by viewing them on a colour-mass diagram, which clearly reveals the bimodal nature of galaxy populations. Bluer colour is a signifier of ongoing star formation, so the two populations represent star-forming and non-star-forming (quenched) galaxies. Figure 1.1 shows the stellar $u-r$ colour vs. stellar mass for ∼50,000 galaxies in the SDSS+GALEX+Galaxy Zoo datasets (Schawinski et al.; 2014). The two populations are commonly referred to as the red-sequence and the blue-cloud. The red-sequence contains galaxies that are redder and primarily elliptical, early-type galaxies. Conversely, the blue-sequence is composed of galaxies that are bluer and mostly spiral late-type.

The colour differences between galaxies arises from their stellar populations. Stars themselves have a wide range of colours, with low-mass stars being dim and red, and high-mass stars being brighter and bluer. This means that blue-sequence galaxies contain a higher fraction of high-mass stars. These stars are short-lived and will die only a few million years after their creation, compared to low-mass red stars which can survive for billions of years. It then follows that to appear blue, a galaxy must be constantly replenishing its population of massive stars by forming new stars. In this way, the blue-sequence and red-cloud are divided by their current star formation rates; blue-cloud galaxies are actively forming stars, while star formation has been largely quenched in red-sequence galaxies. There is also an overlapping region between the two populations, referred to as the green valley. Fewer galaxies are observed in the green valley, indicating that it is a transition region, where an individual galaxy spends a shorter amount of time.

While some properties of a galaxy (such as colour) depend on internal processes, the external environment a galaxy exists within can play an important role as well. A galaxy's environment is determined by where it exists within the large-scale cosmology of the Universe. Within the Λ-CDM model (Blumenthal et al.; 1984), quantum fluctuations in the early Universe are inflated into large scale density fluctuations. These grow due to gravity, ultimately collapsing into bound structures that merge with each other, and eventually develop into the large-scale structure of the Universe seen today. The result is a vast web-like structure that spans the Universe (Bond et al.; 1996). The cosmic web is primarily composed of dark matter, which accounts for ∼95% of all matter in the Universe (Planck Collaboration; 2016a). Within the web, matter is arranged into

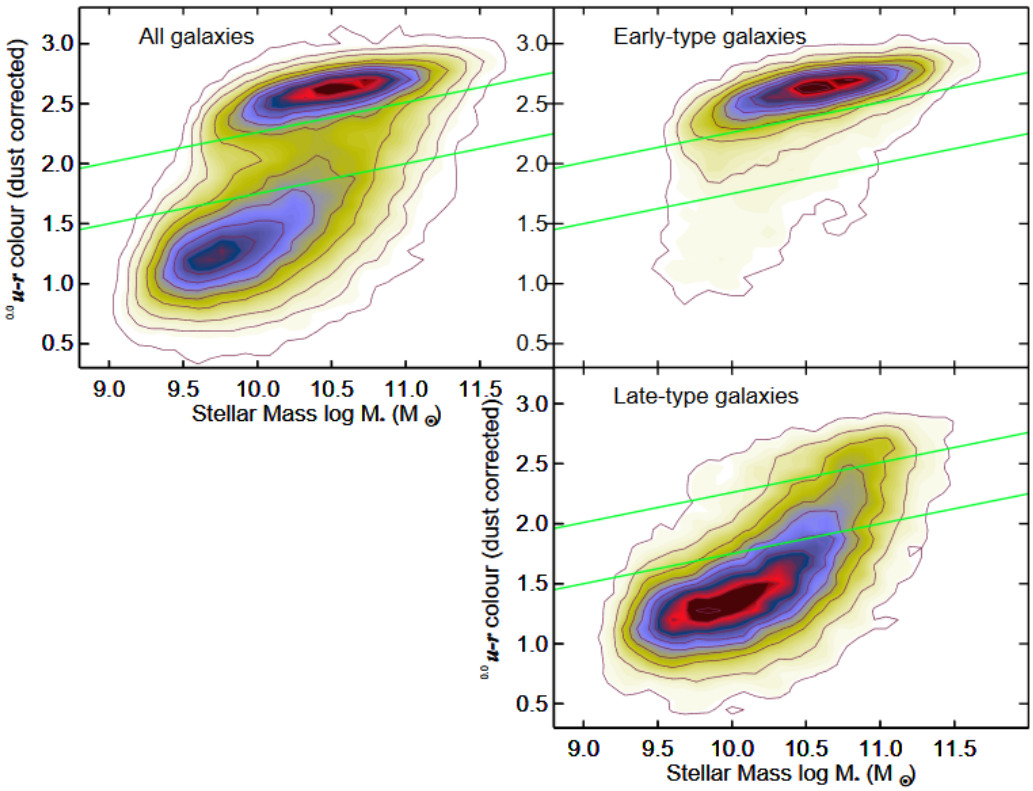

FIGURE 1.1: Colour-Mass diagram from Schawinski et al. 2014. Left panel shows all galaxies. Top and bottom right panels shows only galaxies that have and early or late type morphology respectively.

filaments that span millions of light years, separated by even larger empty voids. Galaxies are found embedded within the gravitational potential of the dark matter in the web. The highest concentrations of dark matter are found at the intersections of the filaments, and these regions can contain clusters of hundreds or even thousands of galaxies.

As the large-scale structure of the Universe was evolving, so too were the galaxies within it. The early Universe was much denser, meaning halos were rapidly merging and accreting gas, leading to high star formation rates in young galaxies. The comoving cosmic star formation rate (SFR) volume-density peaked at a redshift of z$\sim$2, about 10 billion years ago (Madau and Dickinson; 2014). Since then star formation has quenched in some galaxies, causing them to redden overtime. This is especially true in high-density regions like galaxy clusters where environmental quenching mechanisms have

lead to higher fractions of red elliptical galaxies (Dressler; 1980; Muzzin et al.; 2012; Brown et al.; 2023). In contrast, isolated galaxies have remained relatively undisturbed, and many have sustained star-forming disks for the last 10 billion years. Our own Milky-way galaxy is one such galaxy, with the last major merger having occurred around 9.5 billion years ago (Belokurov et al.; 2020).

At this point, the large-scale structure of the Universe is very well constrained, and most uncertainty in modeling galaxy evolution comes from the baryonic physics controlling star formation and gas flows. A natural place to study this physics is in isolated spiral galaxies where star formation is ongoing. A benefit of studying these systems is that they have mostly quiet evolution, without the chaotic effects of large-scale structure and mergers. Hence, they are the focus of the remainder of this thesis.

1.1.2 Star formation in Spiral Galaxies

Understanding star formation is critical to understanding the evolution of galaxies. To first order, star formation can be understood as a process that consumes interstellar gas as fuel. The more fuel available, the higher the SFR. However, star formation is inefficent; in most galaxies it would take 1-2 Gyr to consume their current gas supply at current SFRs (Bigiel et al.; 2011; Saintonge et al.; 2011). This is very slow compared to the timescale for dense gas free-falling under gravitational collapse ($\sim$ 10 Myr). This mismatch in timescales forms the basis to the modern understanding of star formation; not a one-way gravitational collapse, but a self-regulating cycle where young stars return energy into the surrounding gas. This creates a feedback cycle that limits the efficiency of star formation. The relationship between SFR and gas surface density is shown in Figure 1.2. In this plot each point represents an entire galaxy. The relationship is commonly fit with a power-law, known as the Kennicutt-Schmidt (KS) relation.

$$\Sigma_{\rm SFR} = A\Sigma_{\rm gas}^{N} \tag{1.1}$$

This equation relates SFR surface density $\Sigma_{\rm SFR}$, to the total surface density of gas $\Sigma_{\rm gas}$, with $N = 1.4$ (Schmidt; 1959; Kennicutt; 1998). This relation holds for different types of galaxies such as regular-spirals, starbursts, and low-surface-brightness galaxies.

The KS power-law works well when measuring entire galaxies, where regions with different surface densities are averaged together. However, high-resolution telescopes such as the Atacama Large Millimetre Array (ALMA) can now resolve the substructure within galaxies, and when the KS relation is measured on those smaller scales it is

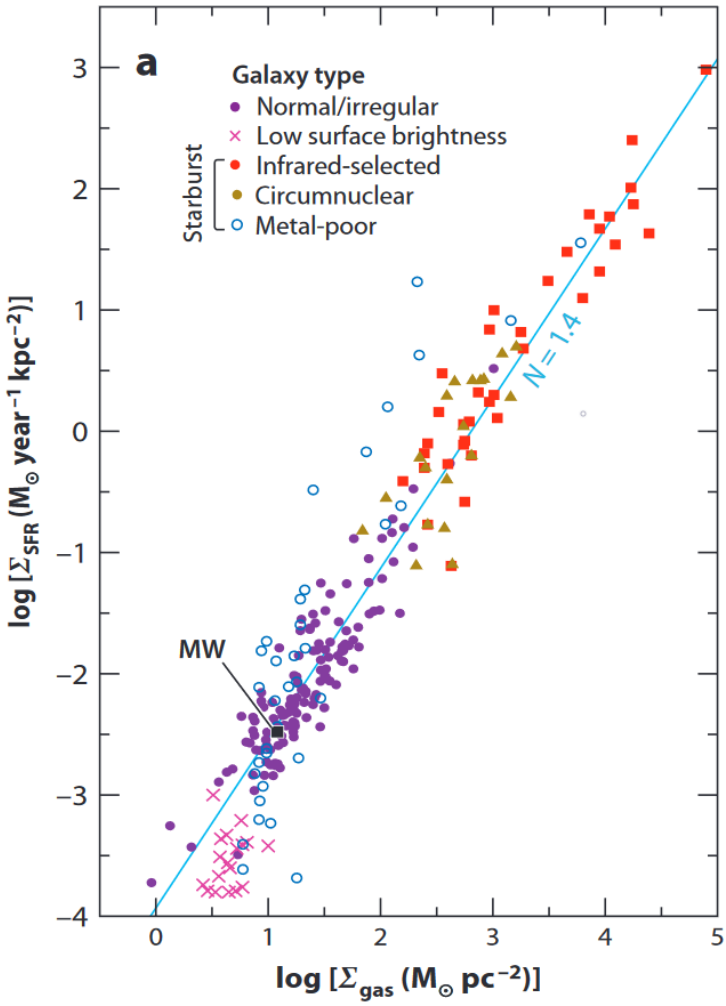

FIGURE 1.2: Global Kennicutt-Schmidt relation from Kennicutt and Evans (2012)

not as simple. At surface densities below 10 $M_{\odot}/pc^2$ the correlation disappears and instead there is a wide range of Σ_{SFR} for a given Σ_{gas} (Schruba et al.; 2011; Liu et al.; 2011). This implies that in low-surface density regions the gas can be supported against gravitational collapse without having substantial SFRs. Another factor that complicates measuring the KS relation at high resolution is that different wavelengths of light are used to observe dense gas and star formation. When young star clusters form within gas-rich regions, they consume or expel the material immediately surrounding them, creating an observable offset between the two. This has been framed as an uncertainty principle for star formation, because the correlations between gas surface density and SFR begin to break down at kpc scales (Kruijssen and Longmore; 2014; Kruijssen et al.;

Phase	T (K)	n (cm^{-3})	Scale Height (pc)	M (10^9 M$_\odot$)
Hot Ionized Medium	10^6	0.003	3000	-
Warm Ionized Medium	8000	0.1	900	1.0
Warm Neutral Medium	8000	0.5	220	2.8
Cold Neutral Medium	80	50	94	2.2
Giant Molecular Clouds (GMCs)	20	>100	75	1.3

TABLE 1.1: Data from table 1.1 in Tielens (2010). Temperature, density, scale height and total mass of different phases of gas in the ISM of the Milky Way.

2018).

Regardless of scale, early galaxy simulations showed that global star formation laws were not sufficient to predict the SFRs of galaxies. Simulations that used these laws produced too many stars and were unable to reproduce observational trends such as the luminosity function of galaxies (Navarro and Benz; 1991; Navarro et al.; 1995; Balogh et al.; 2001). This was occurring because the simulations had finite numerical resolution, which caused the feedback energy from stars to be diluted into large regions, allowing it to be rapidly lost by radiative cooling. This overcooling occurred so efficiently that star formation became a runaway process, and the simulations they predicted unrealistically high SFRs. This came to be known as the "overcooling catastrophe" (Benson et al.; 2003). The solution to this problem was more sophisticated stellar feedback models that effectively heat the gas or otherwise prevent it from collapsing. However, understanding the interplay between stellar feedback and gas cooling requires a detailed understanding of the physics and chemistry occurring within the gas of the interstellar medium.

1.1.3 The Interstellar Medium (ISM)

The ISM consists of all the gas between the stars in a galaxy. It is primarily composed of hydrogen with 30% Helium by mass and trace amounts of heavier elements which play important roles in radiative cooling. The gas ranges in number density from 10^{-4} particles per cubic centimeter (cm^{-3}) in the more diffuse regions and exceeding 10^6 cm^{-3} in the densest clouds. The wide range of densities means that gas exists in different phases, each with distinct temperatures, chemical compositions, and ionization states. Each phase emits different types of radiation and therefore has different observational signatures. The main phases of the ISM are summarized in Table 1.1.

The majority of mass in diffuse gas ($n < 1$ cm^{-3}) exists in clouds of neutral atomic

hydrogen, which has long been observed in the Milky Way through 21 cm hydrogen line emission. Neutral gas is separated into the cold neutral medium (CNM) with temperatures of T $\sim$ 80 K, and warm the neutral medium (WNM) with temperatures of T $\sim$ 8000 K. Embedded within the neutral clouds are giant molecular clouds (GMCs), which are the coldest and most dense regions of the ISM (n $>$ 100 cm^{-3}, T $\sim$ 20 K). The high densities within GMCs shields the gas from dissociating radiation, allowing molecular hydrogen to exist. Molecular hydrogen does not emit any observable light, but its presence is inferred through other tracer molecules that exist alongside it, such as CO which has an observable transition line at 2.6 mm. The ISM also has ionized gas at both warm (T $\sim$ 8000K) and hot (T $\sim$10^6 K) temperatures, which together fill over 50‘% of the total ISM volume. The warm ionized medium (WIM) is observed through the Hα line (656 nm), and the hot ionized medium (HIM) is observed with UV absorption lines of highly ionized species (eg. CIV, SVI, NV, OVI).

The phases of the ISM are dynamic, with gas constantly being exchanged by various physical processes. That means that understanding the various processes in each phase becomes critical to predicting star formation. Inside GMCs, some of the gas will collapse under its own self-gravity resulting in the formation of new stars. However, in the other phases the internal pressure of the gas is often sufficient to stabilize against gravitational contraction, which is why the majority of mass in the ISM is unavailable to form stars.

Early models of the ISM accounted for the warm and cold phases co-existing in a pressure equilibrium (Field et al.; 1969; Wolfire et al.; 2003). When in pressure equilibrium, the two phases naturally emerge from a balance between heating and cooling processes. Heating and cooling are both driven by radiation; There is a broad spectrum of radiation in the ISM which heats the gas through absorption. The dominant mechanism by which radiation heats gas in the neutral ISM is the photoelectric effect; dust grains absorb a UV photon causing them to eject an electron with high kinetic energy that heats the gas. High-energy photons can also heat the gas through photoionization of HI and other molecules, but this is mostly localized in hot regions around young stars. Conversely, the gas cools through its own spontaneous emission, which are observed as various line emissions. Below temperatures of 10^4 K, the cooling is dominated by heavier elements such as C, N, and O, and molecules such as CO. At 10^4 K, the Lyman-α H line begins to play the dominant role.

The two-phase model was challenged in the 1970s when observations of O-VI absorption lines implied the presence of the HIM (Jenkins and Meloy; 1974). In their seminal paper, McKee and Ostriker (1977) proposed that the HIM was created by supernova

explosions producing the high temperature gas. This three-phase model forms the inspiration for most modern ISM models, which include additional physics that affect the exchange of gas between the phases. By creating the HIM, supernova provide effective stellar feedback that contributes to the regulation of star formation. Models for supernova feedback that produce high temperature (T>10^6 K) gas in galaxy simulations are an effective solution to the overcooling problem (Stinson et al.; 2006; Agertz et al.; 2013), because there is no efficient cooling mechanism for gas at these temperatures. Newer supernova feedback models are now designed to properly model thermal conduction to regulate star formation using minimal free parameters (Keller et al.; 2015).

Prior to their death, high-mass ($M > 5M_{\odot}$) stars also generate feedback through ionizing UV radiation and stellar winds. The radiation creates hot and luminous HII regions surrounding young stars (Krumholz and Matzner; 2009) and the stellar winds have speeds up to 1000 km/s (Weaver et al.; 1977). Winds and radiation are considered "early" feedback because they occur while the star is still embedded within the dense gas it formed out of. Because of that most of the energy from early feedback does not escape the cloud into the surrounding ISM. This means early feedback is not as relevant on galactic scales, but it does disperse the gas in the cloud and create small channels that allow the subsequent supernovae feedback to escape and be more effective (Gendelev and Krumholz; 2012; Rogers and Pittard; 2013; Peters et al.; 2017).

Another source of energy in the ISM connected to stellar evolution is cosmic rays. Cosmic rays are high-energy particles accelerated in supernova shock waves. Cosmic rays have similar energy densities to thermal and turbulent energy (Cox; 2005; Zweibel; 2013), but how exactly they couple to the gas is not well understood. They are thought to play an important role setting the thermal state of dense molecular clouds (Papadopoulos and Thi; 2013), and may play an important role in launching galactic outflows (Breitschwerdt et al.; 1991; Everett et al.; 2008; Bustard et al.; 2017). One thing that is certain about cosmic rays is that their dynamics are closely coupled to magnetic fields (following field lines).

1.2 Magnetic Fields

Magnetic fields are another repository of energy within the ISM. They are ubiquitous throughout the Universe and are embedded within almost all astrophysical gas. However, because of the success of stellar feedback models and the difficulty in both modeling and observing magnetic fields, their effects have often been overlooked in galaxy evolution.

Recently, techniques in both observing and modeling fields have improved dramatically and there is increasing evidence that they are important to star formation and galaxy evolution (see section 1.2.5). Figure 1.3 shows the Planck all-sky polarized dust emission map, with magnetic field directions overlaid. This image alone shows that the entire Milky Way is threaded with magnetic fields. The fields are structured over galactic scales, running parallel to structures within the disk, and with large magnetic loops extending above and below the disk.

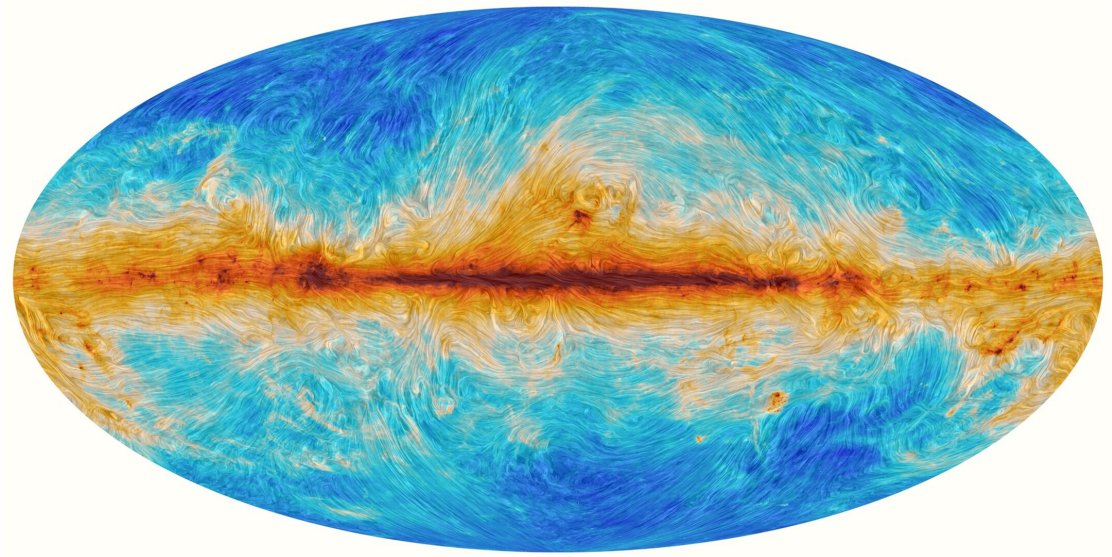

FIGURE 1.3: Planck all-sky polarized dust emission map. Colour represents polarized emission intensity, and textured lines show the direction of the magnetic fields. Image credit: ESA and the Planck Collaboration.

There are many different observational signatures of astrophysical magnetic fields, including the polarization of starlight, synchrotron emission, and emission lines split by the Zeeman effect. The first of which—starlight—is not naturally polarized when emitted, but becomes polarized due to the effects of magnetically aligned dust grains as it travels to the observer. The magnetic moment of non-spherical dust grains causes them to align perpendicular to the magnetic fields (Davis and Greenstein; 1951). The extinction caused by those dust-grains will then occur preferentially along specific polarization angles, causing the dust-grains to act as polarizers. The same dust grains can then re-emit radiation at longer wavelengths, meaning the polarization is also observed in infrared light, but rotated by 90 degrees.

Synchrotron radiation is emitted by relativistic cosmic rays as they spiral around magnetic field lines. Synchrotron emission is typically observed in the radio part of the spectrum. Synchrotron observations can be used to estimate the strength of the magnetic fields, using an assumption of energy equipartition between the cosmic rays and magnetic fields. Synchrotron observations are also able to probe magnetic fields in material along the line of sight, through the use of Faraday rotation. Faraday rotation causes the polarization angle of radiation to rotate as it travels through a magnetized medium. The degree of rotation is proportional to the square of the wavelength observed, so by measuring at different wavelengths, the magnetic field strength along the line of sight can be estimated.

Another method for observing magnetic fields uses the Zeeman effect, and is the only method that provides a direct measurement of field strengths. The Zeeman effect is a quantum mechanical phenomenon that causes individual emission lines of atoms to split into multiple lines when under the influence of magnetic fields, with the amplitude of the split being directly proportional to the field strength. Zeeman splitting was first observed in HI lines, but has also been detected in larger molecules such as H_20 and OH (Heiles and Crutcher; 2005; McBride and Heiles; 2013).

A challenge in interpreting magnetic field observations is that different techniques probe different components of the field. Here, the ordered component refers to coherent, large-scale fields that maintain a consistent orientation over extended regions, while the turbulent component describes small-scale, randomly oriented fields that vary over short distances. The Zeeman effect measures the line-of-sight ordered magnetic field. Starlight polarization traces the plane-of-sky component and similarly depends on the ordered field, since turbulence reduces the net polarization signal along the line of sight. Synchrotron emission captures the total field strength, but its polarized fraction specifically reflects the ordered field, whereas the unpolarized emission arises from turbulent fluctuations. Faraday rotation probes the line-of-sight ordered field, being largely insensitive to turbulent contributions. Because each method also samples gas from different phases of the interstellar medium, no single technique provides a complete picture, making multi-tracer approaches essential for reconstructing the full three-dimensional structure of galactic magnetic fields.

Despite the complexity of the analysis, observations have revealed several distinct features of galactic-scale magnetic fields. Firstly, the fields have typical strengths around $\sim$10 μG, increasing to 100 μG in high surface density or starburst regions (Basu and Roy; 2013; Tabatabaei et al.; 2017; Beck et al.; 2019). These field strengths correspond to the

magnetic fields being in a rough energy equipartition with cosmic rays and turbulence (Boulares and Cox; 1990; Beck and Wielebinski; 2013). Within the Milky Way, there is a strong correlation between magnetic field strength and gas density, of the form $B = B_0 \frac{n}{n_0}^{\alpha}$, with $B_0 \sim 10$ μG, $n_0 \sim 300$ cm^{-3} (Crutcher et al.; 2010). This power law was originally thought to only be valid for gas with densities $n > n_0$ and have a power-law-index of $\alpha \sim 0.65$, which is the theoretical prediction for an isotropic collapsing cloud with perfect flux-freezing (Mestel; 1966). However, a more recent analysis of the same data showed an index of 0.5 was a better fit (Tritsis et al.; 2015). Even more recently, Whitworth et al. (2025) used the Davis-Chandrasekhar-Fermi method, which uses polarized thermal dust emission and velocity dispersion to measure the field strengths, and showed the best fit is a broken power law with indexes 0.26 and 0.77 (Whitworth et al.; 2025). Departures from the classical $\alpha \sim 0.65$ relation suggest that non-ideal effects may play important roles. Another insight from Whitworth et al. (2025) is that the both simulations and observations show the power-law behaviour extends to densities much lower than n_0.

The geometry of galactic magnetic fields also provides critical insight into their origin. Disk galaxies commonly exhibit large-scale (ordered) spiral magnetic structures, both in galaxies with optical spirals (Chyży and Buta; 2008), and those without (Fletcher et al.; 2011; Lopez-Rodriguez et al.; 2023). The magnetic spirals have pitch angles between 10-40 degrees (Fletcher; 2010), consistent with the action of large-scale dynamos that amplify and order the field (see section 1.2.4). However, there is significant differences in the pitch angles measured by far-infrared and radio observations (Borlaff et al.; 2023). In general, the magnetic fields align parallel to density structures such as spiral arms and filaments, down to 100 pc scales (Planck Collaboration; 2016b). In galactic halos, Faraday rotation studies of edge-on galaxies reveal characteristic X-shaped field morphologies (Krause et al.; 2020), which are interpreted as signatures of vertical outflows transporting magnetic flux out of the disk.

1.2.1 Modeling Magnetic Fields

Models of galactic magnetic fields serve two main purposes. They attempt to explain the origin of fields that are observed in real galaxies, and also make predictions for how those fields affect galactic evolution. Similarly to the observations, there are many difficulties in modeling magnetic fields. The basic equations governing the motion of magnetized gases are called the magnetohydrodynamic (MHD) equations. They are constructed similarly to the regular hydrodynamic equations, but with the addition of extra terms

accounting for the effects of magnetic fields and the evolution of the field in response to the gas motions.

$$\frac{\partial \rho}{\partial t} + \nabla \cdot (\rho \vec{v}) = 0 \tag{1.2}$$

$$\frac{\partial \vec{v}}{\partial t} + \vec{v} \cdot (\nabla \vec{v}) = \vec{F} - \frac{1}{\rho} \nabla \left(P + \frac{1}{8\pi} B^2 \right) + \frac{(\vec{B} \cdot \nabla)\vec{B}}{4\pi\rho} + \nu \nabla^2 \vec{v} \tag{1.3}$$

$$\frac{\partial \rho e}{\partial t} = -\nabla \cdot \Big((\rho e + P)\vec{v} - (\vec{v} \cdot \vec{B})\vec{B} + \eta (\nabla \times \vec{B} \times \vec{B}) \Big) \tag{1.4}$$

$$\frac{\partial \vec{B}}{\partial t} = -\nabla \times (\vec{v} \times \vec{B}) + \eta \nabla^2 \vec{B} \tag{1.5}$$

In these equations, ρ is the density of gas, $\vec{v}$ is the gas velocity, P is the pressure, e is the gas total energy per unit mass, $\vec{B}$ is the magnetic field, F is a body force (such as gravity), ν is the viscosity, and η is the magnetic diffusivity. An additional constraint on magnetic fields is that they must be divergence free ($\nabla \cdot B = 0$). These equations preserve that property over time but numerical methods may do so only approximately. The complexity arises because these are coupled partial differential equations, meaning the magnetic field affects the dynamics of the gas (Equations 1.2-1.4), while simultaneously the gas affects the evolution of the field (equation 1.5). However, there are several assumptions that can be safely used to simplify the equations. To demonstrate them, we introduce a dimensionless number called the *magnetic Reynold's number* R_M, given by.

$$R_M = LV/\eta \tag{1.6}$$

where L and V are typical lengths and velocities of the system. R_M is constructed so the values on the numerator and denominator have the same dimensions as the two terms on the right hand side of equation 1.5. Hence, a large R_M implies the first term dominating over the second. For the warm ISM, typical values are around $L = 10^{21}$cm, $V = 10^6$ cm/s and $\eta = 10^7$ cm/s (Choudhuri; 1998). This yields a large value of $R_M = 10^{20}$, meaning that the second term in equation 1.5 can be neglected. For this reason, an infinite conductivity ($\eta = 0$) is often assumed. However, this cannot be realized in practice with finite resolution. Magnetic fields experiences a minimal level of numerical diffusion and thus can only achieve a finite magnetic Reynolds number. Through a similar analysis zero viscosity ($\nu = 0$) is also valid in the ISM. This reduces the equations to the ideal MHD equations:

$$\frac{\partial \rho}{\partial t} + \nabla \cdot (\rho \vec{v}) = 0 \tag{1.7}$$

$$\frac{\partial \vec{v}}{\partial t} + \vec{v} \cdot (\nabla \vec{v}) = \vec{F} - \frac{1}{\rho} \nabla \left(P + \frac{1}{8\pi} B^2 \right) + \frac{(\vec{B} \cdot \nabla)\vec{B}}{4\pi\rho} \tag{1.8}$$

$$\frac{\partial \rho e}{\partial t} = -\nabla \cdot \Big((\rho e + P)\vec{v} - (\vec{v} \cdot \vec{B})\vec{B} \Big) \tag{1.9}$$

$$\frac{\partial \vec{B}}{\partial t} = -\nabla \times (\vec{v} \times \vec{B}) \tag{1.10}$$

A direct consequence of the ideal MHD equations is the conservation of magnetic flux. Alfvén's theorem states that the magnetic flux through any surface moving with the plasma remains constant in time (Alfvén; 1942). This result follows from the ideal induction equation, along with the assumption that magnetic monopoles do not exist. The key implication of Alfvén's theorem is that magnetic field lines are "frozen into" the plasma, meaning fluid elements and field lines move together. As a result, magnetic reconnection, which requires field lines to break and reconnect, cannot occur in ideal MHD since it relies on magnetic diffusion. Another way to express Alfvén's theorem is that the topology of the magnetic field is preserved in ideal MHD. This topological invariance implies the conservation of magnetic helicity, a quantity that measures the degree to which magnetic field lines are twisted, linked, or knotted within a volume.

Having established that magnetic field lines are effectively frozen into the plasma flow, it's useful to examine the forces they exert. In the ideal MHD momentum equation (Equation 1.8), the magnetic terms on the right-hand side can be interpreted as two distinct components of the Lorentz force: magnetic pressure and magnetic tension. The B^2 term corresponds to magnetic pressure, which resists the compression of field lines and acts similarly to a gas pressure. This pressure can influence large-scale phenomena, such as regulating star formation in galaxies (Ostriker et al.; 2010). The term $(\vec{B} \cdot \nabla)\vec{B}$ represents magnetic tension, a restoring force that resists the bending of field lines. Magnetic tension is especially important in the evolution of magnetic field configurations and plays a central role in processes such as the magnetic dynamo.

1.2.2 Dynamos

A key process involved in the evolution of magnetic fields is the dynamo. At its heart, a dynamo is a process that converts kinetic energy into magnetic energy through electromagnetic induction. This is the same process that occurs within electrical generators,

but hydromagnetic dynamos are sustained by the flows of conducting fluids, and do not rely on external currents or magnetic fields. The theory of hydromagnetic dynamos was first postulated as a source for the magnetic fields of the Sun by Joseph Larmor in 1919, but has since been generalized for many astrophysical systems including planets, accretion disks, and galaxies.

Before discussing how dynamos operate, it is worth mentioning one of their limitations. Dynamos cannot generate magnetic fields from an initial state of zero field, because $\vec{B} = 0$ is a perfectly valid solution to the induction equation. In other words, dynamos require a non-zero "seed" magnetic field to operate. This raises an important question: how were the first magnetic fields generated in the early universe?

One widely studied mechanism for producing the cosmological seed fields is the Biermann battery effect (Biermann; 1950). The Biermann battery arises in plasmas where there are misaligned gradients of electron pressure and density, leading to the spontaneous generation of a weak magnetic field even in the absence of an initial field. This process can occur naturally in ionized gas with non-parallel temperature and density gradients, such as those found in shocks or during the formation of the first cosmic structures (Xu et al.; 2008). The magnetic fields generated by the Biermann battery would be extremely weak but provide the crucial initial conditions necessary for galactic dynamo processes that subsequently amplify and sustain the magnetic fields observed.

Dynamos naturally arise from hydrodynamical motions of conducting fluids. There are many different types of flows in which dynamo action can be achieved, but a simple illustrative model is the stretch–fold–twist dynamo described by Zeldovich et al. (1990). This process amplifies the magnetic field by stretching, twisting, and then folding the field lines back on themselves, as illustrated in Figure 1.4. Each repetition of this sequence effectively doubles the number of field lines and the magnetic flux through the loop. Importantly, these motions are three-dimensional, and it has been proven that a purely two-dimensional velocity field cannot sustain dynamo action (Zeldovich and Ruzmaikin; 1980).

The stretch–fold–twist dynamo is classified as a fast dynamo, because it exhibits a growth rate that remains finite as the magnetic Reynolds number, R_M, becomes large. In other words, the amplification rate does not depend on magnetic diffusion. Although field lines may reconnect (by diffusion) after the fold step, the amplification has already occurred by that stage. This justifies the use of the ideal induction equation (Equation 1.10), and the solution will be of the form $B \propto \exp(\gamma t)$, with the growth rate γ on the

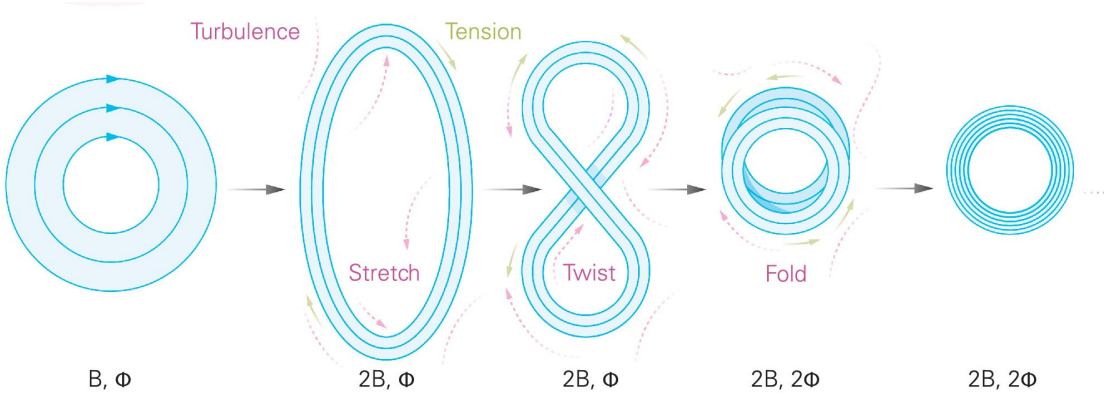

FIGURE 1.4: Schematic diagram showing how the stretch-twist-fold dynamo of Zeldovich et al. (1990). Modified from Steinwandel et al. (2024) with permission.

order of V/L (Shukurov et al.; 2019). The key takeaway is that fast dynamos operate in the kinematic regime, where velocity fields are driven by non-magnetic forces and lead to exponential magnetic field growth. Given the typically large values of R_M in astrophysical systems, fast dynamos generally dominate magnetic field amplification when the fields are weak relative to hydrodynamical forces.

There are also slow dynamos that have growth rates that diminish as R_M increases. One example is the rope dynamo discussed within Alfvén (1950), which relies on magnetic diffusion to break the magnetic loop into two rather than twisting and folding it. As $R_M \to \infty$, diffusion will become the rate-limiting step, and the growth rates become dependent on diffusion rates ($\gamma \sim \eta$). The evolution of the magnetic field during slow dynamo-action is non-linear and is less well understood than kinematic dynamos.

In the context of galaxies, two primary dynamo processes have been extensively studied, both driven by turbulent motions. The first is the small-scale dynamo, also known as the fluctuation dynamo. This is a fast dynamo that amplifies magnetic fields exponentially in the kinematic regime. The second is the large-scale dynamo, also known as the mean-field dynamo, which generates magnetic fields coherent over scales larger than the turbulent fluctuations. The mean-field dynamo has been studied in both the kinematic and diffusive regimes, though in galaxies it likely operates primarily in the diffusive regime because the small-scale dynamo amplifies field strengths very rapidly.

1.2.3 The Small-Scale dynamo

The small-scale dynamo generates magnetic fields through random, turbulent motions within a conducting fluid. In essence, the turbulent velocity field performs repeated and rapid stretch–twist–fold actions on magnetic field lines, leading to exponential amplification during the kinematic regime. Originally formulated by Kazantsev (1968), the theory of the small-scale dynamo predicts that the magnetic energy spectrum follows a characteristic slope of $E_B(k) \propto k^{3/2}$ in the kinematic regime, before nonlinear saturation. This prediction has been confirmed in numerous MHD simulations (e.g., Schekochihin et al. (2005); Rieder and Teyssier (2016); Beattie et al. (2025)), and serves as a key diagnostic for identifying small-scale dynamo action in numerical studies.

The small-scale dynamo is believed to be active across a wide range of astrophysical environments, including galaxy clusters, protogalaxies, the early universe, and particularly the interstellar medium (ISM). In the ISM, the small-scale dynamo amplifies fields with exponential growth rates of $\sim 10 - 100$ Myr when in the kinematic regime. (Federrath, Chabrier, Schober, Banerjee, Klessen and Schleicher; 2011; Schober et al.; 2013; Bhat et al.; 2016; Pakmor et al.; 2020; Martin-Alvarez et al.; 2022). This rapid amplification makes it a strong candidate for the initial buildup of magnetic energy in the early phases of galaxy evolution, and is consistent with the near-equipartition field strengths observed in young-galaxies.

Observational evidence for small-scale dynamo action is found in a range of astrophysical systems. In young and irregular galaxies, Faraday rotation measures often show strong spatial fluctuations without a dominant mean-field direction, consistent with amplification by a small-scale dynamo (Bhat and Subramanian; 2013; Sur et al.; 2018). In elliptical galaxies, where differential rotation and ordered disk structures are absent, the conditions for large-scale dynamo action are unfavorable (Section 1.2.4). Nevertheless, observations still reveal magnetic fields of several μG, implying that turbulent small-scale dynamo activity alone can account for the measured field strengths (Seta et al.; 2021). In galaxy clusters, synchrotron emission and Faraday rotation maps reveal tangled μG-level fields on kiloparsec scales, pointing again to dynamo amplification in highly turbulent hot halos (Eilek and Owen; 2002; Murgia et al.; 2004; Di Gennaro et al.; 2021). Together, these systems demonstrate that the small-scale dynamo operates efficiently across diverse environments, making it a nearly universal mechanism for amplifying weak seed fields in turbulent astrophysical plasmas.

Numerically, resolving the small-scale dynamo requires high spatial resolution because

the dynamo operates at scales near or below the coherence scale of the turbulence. As a rule of thumb, the magnetic Reynolds number must exceed a critical value (typically $R_M > 100$) for the dynamo to operate (Brandenburg and Subramanian; 2005). In practice, this means resolving several turbulent eddies across the simulation domain with sufficient fluid elements, or resolving the Jean's length by ~ 30 resolution elements (Federrath, Sur, Schleicher, Banerjee and Klessen; 2011).

While the presence of the small-scale dynamo within galaxies is now well-accepted, the magnetic fields it generates are tangled on the turbulent coherence length. However, the fields observed in disk galaxies are coherent over kpc scales. This could potentially be explained by the driving of a small-scale dynamo on CGM scales (Pudritz and Silk; 1989; Rieder and Teyssier; 2017a). However, more commonly a secondary large-scale dynamo is invoked to explain the large-scale fields (Subramanian; 1998; Widrow; 2002).

1.2.4 The Large-Scale Dynamo

A large-scale dynamo amplifies magnetic fields on spatial scales larger than the characteristic scale of the turbulent motions. In galaxies, the most well-studied large-scale dynamo is the α–Ω dynamo, first proposed by Parker (1955) and further developed in subsequent decades (Steenbeck and Krause; 1969; Vainshtein and Ruzmaikin; 1972; Brandenburg and Subramanian; 2005). This dynamo operates through an interplay between turbulent helical motions (the α-effect) and differential rotation (the Ω-effect).

The α–Ω dynamo requires two conditions to operate: differential rotation and helical turbulence. Within their disk, spiral galaxies naturally exhibit strong differential rotation, but the origin of helical turbulence is more subtle. It arises due to the action of the Coriolis force on buoyant, rising turbulent eddies above the galactic disk. As a gas parcel rises into regions of lower pressure, it expands. The Coriolis force acting on this expanding motion imparts a rotation aligned with the direction of galactic rotation. This breaks the symmetry between clockwise and counterclockwise rotating eddies, resulting in net helicity in the turbulence.

When turbulence is helical, magnetic fields embedded in the rotating eddies collectively produce a net electromotive force, which can generate a radial component of the magnetic field. Differential rotation then shears this radial field into an azimuthal component, completing the dynamo feedback loop. This process leads to the spontaneous amplification of the large-scale magnetic field, as long as the necessary conditions persist.

The α–Ω dynamo is generally considered the most plausible mechanism for generating the coherent, galaxy-scale magnetic fields observed in disk galaxies. It is expected to produce specific observational signatures, including magnetic spiral and quadrupolar field structures in galactic halos (Stix; 1975; Henriksen; 2017; Shukurov et al.; 2019). These features have been reproduced in some isolated galaxy simulations, such as those by Ntormousi et al. (2020) which also showed evidence of helical turbulence, providing some numerical support for the model.

However, several challenges remain. Chief among them is the expected growth timescale. The α–Ω dynamo is relatively slow, typically requiring several gigayears to build up coherent large-scale fields. This poses a tension with recent observational results: Geach et al. (2023) reported the presence of a coherent, galaxy-scale magnetic field in a system observed only 2.5 billion years after the Big Bang. If confirmed, such observations may suggest the need for a more rapid or efficient mechanism.

1.2.5 Magnetic Fields in Galaxy Evolution

While dynamos describe how fluid motions generate and amplify magnetic fields, the reverse interaction is equally important. Because of the rapid amplification of fields by the small-scale dynamo, magnetic fields are already amplified to their observed field strengths corresponding to equipartition with the cosmic rays and turbulent energy, for most of a galaxy's lifetime. At these levels they can exert significant influence on the dynamics of the gas and can shape the structure and evolution of the interstellar medium. Their influence extends from the scale of dense star-forming clouds to the global regulation of turbulence, angular momentum transport, and outflows.

A significant role magnetic fields play is in regulating star formation. Magnetic pressure can provide an additional form of support against gravitational collapse, particularly in molecular clouds. A useful conceptual framework is the idea of cloud criticality: a cloud is considered subcritical when magnetic support dominates over self-gravity, inhibiting collapse, and supercritical when gravitational energy exceeds magnetic support, allowing star formation to proceed. This can be framed as a critical mass-to-flux ratio given by

$$\left(\frac{M}{\Phi}\right)_{\text{crit}} = \frac{1}{2\pi\sqrt{G}} \tag{1.11}$$

where Φ is the magnetic flux (Nakano and Nakamura; 1978). Observations suggest that while dense star-forming cores tend to be supercritical, the envelopes of clouds are often near-critical or subcritical, suggesting that magnetic fields delay collapse and regulate

cloud fragmentation (Crutcher et al.; 2010; Pattle et al.; 2023). The criticality analysis can also be extended to ISM filaments, which will collapse above a critical mass per unit length. (Fiege and Pudritz; 2000; Federrath; 2016; Pillsworth et al.; 2025).

Across multiple scales, magnetic fields also regulate turbulence and transport angular momentum transport. MHD turbulence predicts a universal width for magnetized ISM filaments, which matches the observed distributions closely (Arzoumanian et al.; 2011; Federrath; 2016). Magnetic fields may also be responsible for driving turbulence, through the magnetorotational instability (MRI) (Balbus and Hawley; 1991), which was originally developed for accretion disks. There remains debate over whether the MRI is active in galactic disks (Kim et al.; 2003; Machida et al.; 2013). Magnetic fields transport angular momentum through a process known as magnetic braking. Magnetic braking can occur in a rotating system that contains magnetic fields aligned with the rotation axis. As the fields rotate, magnetic tension will transfer the angular momentum upwards out of the disk (Mestel; 1968). Magnetic braking is critically important in protostellar collapse (Li et al.; 2011; Wurster et al.; 2016), but has also been shown to be capable of altering the sizes of galactic disks (Martin-Alvarez et al.; 2020).

1.3 Numerical Simulations: a Tool for Studying Galaxies

Numerical simulations are a powerful tool that allow us to follow the evolution of astrophysical systems. Modern simulation codes can handle many different aspects of physics including gravity, magnetohydrodynamics (MHD), star formation, stellar feedback, radiative transfer, and many more. In this section we discuss the methods and approaches commonly used.

The earliest numerical simulations of galaxies accounted for only the effects of gravity. A direct approach to computing the effects of gravity is by calculating the gravitational forces on a system of particles, updating their positions, and repeating. This method is commonly referred to as the N-body problem, due to its lack of an analytical solution for N>2. The first N-body gravity simulations actually predated the use of computers. They were performed in 1941 by a Swedish physicist named Erik Holmberg, who used collections of lightbulbs and photocells to represent individual mass elements of a galaxy. Each lightbulb was used to simulate the gravitational interaction between the mass elements, which was possible because both gravity and light flux follow an inverse square law. This makes it possible to calculate the total gravitational force on each element by measuring the flux at each corresponding bulb. After measuring the forces, the

positions of the bulbs were updated according to their gravitational acceleration. This simple setup was able to show galaxies develop spiral arms and move towards each other from purely gravitational interactions (Holmberg; 1941). Decades later, the use of computerized N-body simulations was pioneered by Toomre and Toomre (1972), who were able to simulate disk galaxies composed of 120 particles. Since then, computers have advanced and so has the scale of N-body simulations. To date, the largest N-body simulation used over 60 trillion particles to calculate the large-scale structure of the Universe (Maksimova et al.; 2021). The algorithms have also improved; modern N-body codes use sophisticated techniques to calculate gravity, such as tree-based methods (Barnes and Hut; 1986) or particle-particle/particle-mesh methods (Couchman; 1991), which reduce the numerical workload considerably.

Gravity-only simulations are a powerful tool for calculations of large-scale structure, but properly modeling the baryonic content of galaxies requires the use of hydrodynamics. Hydrodynamics provides a mathematical framework for describing the motion of fluids, by treating them as a continuum governed by the conservation of mass, momentum, and energy. Numerical hydrodynamic solvers do this by breaking the continuum into discrete elements. An inherent limitation of this approach is the finite numerical resolution. This problem is particularly limiting when simulating galaxies because there is physics that occurs over many orders of magnitude in scale. This makes some processes, such as star formation and stellar-feedback impossible to resolve, even with the most powerful computers. As a result, they are typically modeled using sub-grid prescriptions, which are added as additional sources of energy in the hydrodynamics equations. Sub-grid models are not derived from first principles, so they typically introduce free parameters which are calibrated using theoretical expectations and observational constraints. Designing effective sub-grid models involves balancing two goals: ensuring they produce plausible, physically motivated outcomes, while avoiding over-tuning that undermines their predictive power.

There are multiple techniques for solving the equations of hydrodynamics, but they are mainly divided into two frameworks: Eulerian and Lagrangian (See section 1.2 for the full equations including magnetic terms). Eulerian methods discretize space into fixed grids, tracking the evolution of fluid quantities at stationary points in space. Fluid is transported by calculating fluxes across adjacent grid cells using a Riemann solver (Godunov; 1959). To achieve higher resolution in regions of interest, these codes often employ adaptive-mesh-refinement (AMR), which dynamically splits cells into smaller sub-cells. Eulerian solvers are generally high order, exhibit low numerical noise, and are

effective at resolving shocks. However, they also face limitations including numerical diffusion, difficulty in accurately modeling orbits, and strict timestep constraints due to the Courant condition. Widely used Eulerian hydrodynamics codes in astrophysics include Ramses (Teyssier; 2002), ENZO (Bryan et al.; 2014), FLASH (Fryxell et al.; 2000), and Athena (Stone et al.; 2008).

In contrast, Lagrangian methods discretize mass rather than space. The most common of these is Smoothed Particle Hydrodynamics (SPH), which represents fluids as a collection of particles that move with the flow and are not confined to a grid. Fluid properties are computed through weighted averages over neighboring particles. The particle-based nature of SPH brings both advantages and disadvantages. It naturally conserves mass, energy, momentum, and angular momentum, and it integrates well with tree-based gravity solvers. However, it also inhibits mixing of fluid properties below the resolution scale, which can suppress the growth of fluid instabilities (Agertz et al.; 2007). To address this issues, modern SPH implementations include improvements such as geometric density averaging and artificial diffusion to better model turbulence and mixing (Wadsley et al. (2017)). Prominent SPH codes used in astrophysics include Hydra (Couchman et al.; 1995), Gadget (Springel; 2005), Gasoline (Wadsley et al.; 2004, 2017), and Phantom (Price et al.; 2018).

Beyond pure particle or grid-based methods, hybrid approaches have also been developed, such as Arepo (Springel; 2010). Arepo discretizes fluid using a moving Voronoi mesh and computes fluxes across cell interfaces with a Riemann solver, and uses Dedner cleaning to ensure magnetic fields remain divergence free Dedner et al. (2002). Hybrid methods often outperform traditional approaches in certain regimes, particularly in modeling low Mach number flows and subsonic turbulence. Several major code comparison projects have evaluated different numerical techniques to determine which is best suited for galaxy formation and evolution simulations (Scannapieco et al.; 2012; Kim et al.; 2014, 2016). Most studies conclude that while small differences exist, no single method is universally superior. The choice of code often depends on the specific physical processes and scales being investigated.

Using the methods described above, there are several common approaches to simulating galaxies, each focusing on different physical scales and offering varying trade-offs between numerical resolution and environmental realism.

One widely used method is cosmological simulations, which model large volumes of

the universe and allow galaxies to form naturally as a result of gravity, gas dynamics, and other included physics (Hopkins et al.; 2014; Vogelsberger et al.; 2014; Schaye et al.; 2015; Agertz and Kravtsov; 2016; Keller et al.; 2016; Grand et al.; 2017; Tremmel et al.; 2017; Hopkins et al.; 2018; Springel et al.; 2018). These simulations begin with initial conditions informed by fluctuations in the Cosmic Microwave Background and evolve forward in time within an expanding universe. While cosmological simulations offer valuable statistical power by simulating large populations of galaxies, their spatial resolution is limited. As a result, individual galaxies are often under-resolved. To overcome this, modern simulations frequently use zoom-in techniques, focusing computation on regions containing individual galaxies or groups. This preserves the high-resolution while maintaining the broader cosmological context.

Cosmological simulations have become increasingly successful in reproducing large-scale galaxy properties, such as star formation rates (SFRs) and the observed correlation between galaxy color and stellar mass (Naab and Ostriker; 2017). However, due to their complexity and chaotic nature, the detailed evolution of a single galaxy can be difficult to interpret. Small perturbations can lead to vastly different outcomes (Keller et al.; 2019), and the continual influence of gas inflows, mergers, and changing environment makes it difficult to isolate the impact of specific physical processes. For these reasons, some researchers turn to more controlled environments.

Isolated galaxy simulations focus on a single galaxy, with the full cosmological context replaced by an idealized halo model, allowing for higher resolution within less chaotic environments. Without cosmological gas inflows or interactions with neighboring galaxies, these systems are less dynamic and more stable, making them ideal for testing physical models. However, their isolation limits long-term realism, as the lack of fresh gas supply causes galaxies to exhaust their gas reservoirs over time. Despite these limitations, isolated galaxies are valuable tools for studying the interstellar medium (ISM) in detail. They allow for the resolution of galactic shear, the formation of individual giant molecular clouds (GMCs), and the development of turbulence. These simulations have been used to explore how feedback shapes the ISM (Tasker et al.; 2015; Grisdale et al.; 2017), how the ISM self-regulates (Benincasa et al.; 2016), and how magnetic fields evolve in galactic environments (Dobbs et al.; 2016; Rieder and Teyssier; 2016; Körtgen et al.; 2019).

At even smaller scales, ISM box simulations model small, stratified sections of galactic disks with high resolution (Walch et al.; 2015; Kim and Ostriker; 2017). These simulations typically use periodic boundary conditions in the galactic plane and open

boundaries in the vertical direction, allowing them to track vertical structure and energy injection from supernovae. ISM boxes can resolve the full lifecycle of star-forming clouds and the early phases of feedback, offering a unique window into the microphysics of the ISM. These small-scale simulations have demonstrated the importance of turbulence in supporting galactic disks (Ostriker and Shetty; 2011), and have been used to study the interplay between feedback, magnetic fields, and the time variability of star formation (Walch et al.; 2015; Li et al.; 2017; Kim and Ostriker; 2017). However, they lack the global galactic context, typically omitting shear, large-scale flows, and realistic galactic outflows, which are challenging to model accurately in their simplified geometry (Martizzi et al.; 2016).

Together, these three simulation regimes: cosmological volumes, isolated galaxies, and ISM boxes offer a complementary toolkit. Each captures different aspects of galaxy evolution, from the large-scale evolving cosmological context, to detailed, small-scale physical processes. The choice of method depends on the scientific question being addressed and the computational resources available.

1.3.1 Magnetic fields in Galaxy Simulations

Galaxy simulations have now begun to commonly include MHD, which has highlighted the roles of magnetic fields in galactic evolution. Cosmological simulations with MHD have demonstrated the amplification of fields from primordial seed values ($\sim 10^{-15}$ G) to observed levels ($\sim\ 10^{-5}$ G) during the formation of large-scale structure (Marinacci et al.; 2015; Dolag et al.; 2016; Marinacci et al.; 2018). They have also shown galaxies magnetize their halo with outflows of gas that was amplified in the ISM Pakmor et al. (2020), and can produce field morphologies similar to observationsKovacs et al. (2024). Girichidis et al. (2018) used ISM box simulations to show magnetic fields thicken gas in the disk to 100 pc, delay the collapse of dense gas by up to 25 Myr, and decrease the intercloud velocity dispersion by ~ 3 km/s. Other ISM box models have shown how magnetic fields can significantly reduce the overall star formation in nuclear rings by providing additional pressure support (Ostriker and Kim; 2022; Moon et al.; 2023). Gent et al. (2024) modelled the small-scale dynamo and large-scale dynamo simultaneously in an ISM box, and showed the small-scale dynamo can decrease the growth rate of the large-scale dyanmo by a factor of $\sim$2.

Isolated spiral galaxies provide an ideal testing ground for magnetic fields. Both Wang and Abel (2009) and Dubois and Teyssier (2010) followed the formation of a disk in an idealized halo, and produced field strengths that were a match with observations.

The simulations by Körtgen et al. (2019); Arora et al. (2024) showed that galaxies simulated with MHD fragment significantly faster due to the Parker instability. In these simulations, the ISM fragments into elongated, filamentary structures, and cold gas was driven hundreds of parsecs above the midplane without the inclusion of stellar feedback. While these studies showed how magnetic fields can affect the global evolution of a disk, they did not include any stellar feedback or star formation, so they suffered from overcooling, meaning eventually the entire ISM collapsed into dense clouds. Wibking and Krumholz (2023) simulated isolated galaxies with star formation and feedback and conducted a straightforward test between MHD/hydrodynamics, they found the simulations with magnetic fields produced SFRs 1.5-2 times lower than those without.

Isolated galaxy simulations have also been used to test dynamo activity. Rieder and Teyssier (2016, 2017a,b) conducted a series of tests on small-scale dynamo growth. They found a striking dependence of the growth rate on numerical resolution and stellar feedback. They demonstrated that the small-scale dynamo undergoes three separate phases of growth in the ISM: exponential growth during the kinematic phase, constant growth during the non-linear phase, and no growth once reaching saturation. While the growth rate was closely tied to the numerical resolution, the level at which the fields saturated did not, which motivates initializing galaxies with fields that are closer to a saturated state. Large-scale dynamo activity has been examined in isolated galaxy simulations by Ntormousi et al. (2020); Steinwandel et al. (2020); Wissing and Shen (2023), but each of them attribute the growth to a different large-scale dynamo: the $\alpha\Omega$ dynamo (section 1.2.4), the $\alpha^2\Omega$ dynamo, and the gravitational-instability dynamo of Riols and Latter (2019). The different dynamo behaviour reported by different methods shows the the field has yet to converge on exactly how large-scale dynamos operate within simulations.

The simulations described above have begun to reveal many magnetic effects important to galaxy evolution, but many questions remain. How exactly do magnetic fields contribute to the regulation of star formation in a galactic disk? How and when do large-scale dynamos operate? How do magnetic fields affect the evolution of galactic structures, such as bars and spiral arms? How do small-scale and large-scale dynamos coexist and interact in a realistic galactic environment? Can simulations reproduce the observed correlations between magnetic field strength and gas density or star formation rates? How can we design MHD simulations of galaxies with robust predictive power? While non-exhaustive, the questions in this list are the motivation behind this thesis.

1.4 This Thesis and Chapter Organization

The discussion above highlights that magnetic fields are a fundamental component of the ISM and galaxy evolution, influencing star formation, turbulence, and large-scale dynamics. Understanding how these fields originate, grow, and interact with galactic gas requires a combination of observational insights, theory, and numerical modeling. Isolated galaxy simulations are particularly well-suited for this purpose: they capture essential galactic dynamics such as shear and large-scale rotation while allowing high enough resolution to resolve GMC formation, turbulence, and localized feedback processes. Compared to cosmological simulations, they provide a controlled environment free from mergers and chaotic inflows, and compared to small ISM boxes, they retain the global context necessary for studying magnetic field evolution.

This thesis is structured around three studies that explore different aspects of galactic magnetic fields and their impact on the ISM. This work builds on the methods of Robinson (2021), where we developed a model for simulating isolated disk galaxies with a self-regulating ISM, and began to incorporate magnetic fields. All of our simulations are conducted with the Ramses (Teyssier; 2002) AMR code, which ensures magnetic fields are divergence-free using the constrained transport method (Evans and Hawley; 1988). We reach maximum spatial resolutions of 9.15 pc in all of our simulations, which allows us to resolve the small-scale dynamo (Rieder and Teyssier; 2016).

Chapter 2 presents MHD simulations of isolated disk galaxies with varying initial magnetic field strengths. We investigate the co-evolution of magnetic fields with a self-regulated, star-forming ISM and show that weak seed fields can grow through feedback and turbulence to realistic levels, while initially strong fields modify ISM structure, supernova bubble sizes, and the distribution of star formation. This study demonstrates how magnetic pressure, turbulence, and thermal energy jointly regulate star formation.

Chapter 3 focuses on the role of spiral arms in the evolution of magnetic fields and star formation. Using MHD simulations both with and without self-consistent stellar spiral arms, we find that spirals concentrate gas to enhance star formation and enable a large-scale dynamo, producing coherent magnetic fields aligned with the arms and coherent over kiloparsec scales. This provides a novel mechanism for mean-field amplification in disk galaxies.

Chapter 4 explores the influence of the initial magnetic field configuration on galaxy

evolution. The results indicate that while the total star formation rate is largely insensitive to the initial field morphology, the formation of central bars and the spatial distribution of star formation are affected.

Finally, Chapter 5 summarizes the main results, discusses their broader implications, and outlines directions for future research.

Bibliography

Agertz, O. and Kravtsov, A. V. (2016). The Impact of Stellar Feedback on the Structure, Size, and Morphology of Galaxies in Milky-Way-sized Dark Matter Halos, **824**(2): 79.

Agertz, O., Kravtsov, A. V., Leitner, S. N. and Gnedin, N. Y. (2013). Toward a Complete Accounting of Energy and Momentum from Stellar Feedback in Galaxy Formation Simulations, **770**(1): 25.

Agertz, O., Moore, B., Stadel, J., Potter, D., Miniati, F., Read, J., Mayer, L., Gawryszczak, A., Kravtsov, A., Nordlund, Å., Pearce, F., Quilis, V., Rudd, D., Springel, V., Stone, J., Tasker, E., Teyssier, R., Wadsley, J. and Walder, R. (2007). Fundamental differences between SPH and grid methods, **380**(3): 963–978.

Alfvén, H. (1942). Existence of Electromagnetic-Hydrodynamic Waves, **150**(3805): 405–406.

Alfvén, H. (1950). Discussion of the Origin of the Terrestrial and Solar Magnetic Fields, *Tellus* **2**: 74–82.

Arora, R., Federrath, C., Banerjee, R. and Körtgen, B. (2024). Role of magnetic fields in disc galaxies: spiral arm instability, **687**: A276.

Arzoumanian, D., André, P., Didelon, P., Könyves, V., Schneider, N., Men'shchikov, A., Sousbie, T., Zavagno, A., Bontemps, S., di Francesco, J., Griffin, M., Hennemann, M., Hill, T., Kirk, J., Martin, P., Minier, V., Molinari, S., Motte, F., Peretto, N., Pezzuto, S., Spinoglio, L., Ward-Thompson, D., White, G. and Wilson, C. D. (2011). Characterizing interstellar filaments with Herschel in IC 5146, **529**: L6.

Balbus, S. A. and Hawley, J. F. (1991). A Powerful Local Shear Instability in Weakly Magnetized Disks. I. Linear Analysis, **376**: 214.

Balogh, M. L., Pearce, F. R., Bower, R. G. and Kay, S. T. (2001). Revisiting the cosmic cooling crisis, **326**(4): 1228–1234.

Barnes, J. and Hut, P. (1986). A hierarchical O(N log N) force-calculation algorithm, **324**(6096): 446–449.

Basu, A. and Roy, S. (2013). Magnetic fields in nearby normal galaxies: energy equipartition, **433**(2): 1675–1686.

Beattie, J. R., Federrath, C., Klessen, R. S., Cielo, S. and Bhattacharjee, A. (2025). The spectrum of magnetized turbulence in the interstellar medium, *Nature Astronomy* .

Beck, R., Chamandy, L., Elson, E. and Blackman, E. G. (2019). Synthesizing Observations and Theory to Understand Galactic Magnetic Fields: Progress and Challenges, *Galaxies* **8**(1): 4.

Beck, R. and Wielebinski, R. (2013). Magnetic Fields in Galaxies, *in* T. D. Oswalt and G. Gilmore (eds), *Planets, Stars and Stellar Systems. Volume 5: Galactic Structure and Stellar Populations*, Vol. 5, p. 641.

Belokurov, V., Sanders, J. L., Fattahi, A., Smith, M. C., Deason, A. J., Evans, N. W. and Grand, R. J. J. (2020). The biggest splash, **494**(3): 3880–3898.

Benincasa, S. M., Wadsley, J., Couchman, H. M. P. and Keller, B. W. (2016). The anatomy of a star-forming galaxy: pressure-driven regulation of star formation in simulated galaxies, **462**(3): 3053–3068.

Benson, A. J., Bower, R. G., Frenk, C. S., Lacey, C. G., Baugh, C. M. and Cole, S. (2003). What Shapes the Luminosity Function of Galaxies?, **599**(1): 38–49.

Bhat, P. and Subramanian, K. (2013). Fluctuation dynamos and their Faraday rotation signatures, **429**(3): 2469–2481.

Bhat, P., Subramanian, K. and Brandenburg, A. (2016). A unified large/small-scale dynamo in helical turbulence, **461**(1): 240–247.

Biermann, L. (1950). Über den ursprung der magnetfelder auf sternen und im interstellaren raum, *Zeitschrift für Naturforschung A* **5**(2): 65–71.

Bigiel, F., Leroy, A. K., Walter, F., Brinks, E., de Blok, W. J. G., Kramer, C., Rix, H. W., Schruba, A., Schuster, K. F., Usero, A. and Wiesemeyer, H. W. (2011). A Constant Molecular Gas Depletion Time in Nearby Disk Galaxies, **730**(2): L13.

Blumenthal, G. R., Faber, S. M., Primack, J. R. and Rees, M. J. (1984). Formation of galaxies and large-scale structure with cold dark matter., **311**: 517–525.

Bond, J. R., Kofman, L. and Pogosyan, D. (1996). How filaments of galaxies are woven into the cosmic web, **380**(6575): 603–606.

Borlaff, A. S., Lopez-Rodriguez, E., Beck, R., Clark, S. E., Ntormousi, E., Tassis, K., Martin-Alvarez, S., Tahani, M., Dale, D. A., del Moral-Castro, I., Roman-Duval, J., Marcum, P. M., Beckman, J. E., Subramanian, K., Eftekharzadeh, S. and Proudfit, L. (2023). Extragalactic Magnetism with SOFIA (SALSA Legacy Program). V. First Results on the Magnetic Field Orientation of Galaxies, **952**(1): 4.

Boulares, A. and Cox, D. P. (1990). Galactic Hydrostatic Equilibrium with Magnetic Tension and Cosmic-Ray Diffusion, **365**: 544.

Brandenburg, A. and Subramanian, K. (2005). Astrophysical magnetic fields and nonlinear dynamo theory, **417**(1-4): 1–209.

Breitschwerdt, D., McKenzie, J. F. and Voelk, H. J. (1991). Galactic winds. I. Cosmic ray and wave-driven winds from the galaxy., **245**: 79.

Brown, T., Roberts, I. D., Thorp, M., Ellison, S. L., Zabel, N., Wilson, C. D., Bahé, Y. M., Bisaria, D., Bolatto, A. D., Boselli, A., Chung, A., Cortese, L., Catinella, B., Davis, T. A., Jiménez-Donaire, M. J., Lagos, C. D. P., Lee, B., Parker, L. C., Smith, R., Spekkens, K., Stevens, A. R. H., Villanueva, V. and Watts, A. B. (2023). VERTICO. VII. Environmental Quenching Caused by the Suppression of Molecular Gas Content and Star Formation Efficiency in Virgo Cluster Galaxies, **956**(1): 37.

Bryan, G. L., Norman, M. L., O'Shea, B. W., Abel, T., Wise, J. H., Turk, M. J., Reynolds, D. R., Collins, D. C., Wang, P., Skillman, S. W., Smith, B., Harkness, R. P., Bordner, J., Kim, J.-h., Kuhlen, M., Xu, H., Goldbaum, N., Hummels, C., Kritsuk, A. G., Tasker, E., Skory, S., Simpson, C. M., Hahn, O., Oishi, J. S., So, G. C., Zhao, F., Cen, R., Li, Y. and Enzo Collaboration (2014). ENZO: An Adaptive Mesh Refinement Code for Astrophysics, **211**(2): 19.

Bustard, C., Zweibel, E. G. and Cotter, C. (2017). Cosmic Ray Acceleration by a Versatile Family of Galactic Wind Termination Shocks, **835**(1): 72.

Choudhuri, A. R. (1998). *The Physics of Fluids and Plasmas: An Introduction for Astrophysicists*.

Chyży, K. T. and Buta, R. J. (2008). Discovery of a Strong Spiral Magnetic Field Crossing the Inner Pseudoring of NGC 4736, **677**(1): L17.

Couchman, H. M. P. (1991). Mesh-refined P 3M: A Fast Adaptive N-Body Algorithm, **368**: L23.

Couchman, H. M. P., Thomas, P. A. and Pearce, F. R. (1995). Hydra: an Adaptive-Mesh Implementation of P 3M-SPH, **452**: 797.

Cox, D. P. (2005). The Three-Phase Interstellar Medium Revisited, **43**(1): 337–385.

Crutcher, R. M., Wandelt, B., Heiles, C., Falgarone, E. and Troland, T. H. (2010). Magnetic Fields in Interstellar Clouds from Zeeman Observations: Inference of Total Field Strengths by Bayesian Analysis, **725**(1): 466–479.

Davis, Jr., L. and Greenstein, J. L. (1951). The Polarization of Starlight by Aligned Dust Grains., **114**: 206.

Dedner, A., Kemm, F., Kröner, D., Munz, C. D., Schnitzer, T. and Wesenberg, M. (2002). Hyperbolic Divergence Cleaning for the MHD Equations, *Journal of Computational Physics* **175**(2): 645–673.

Di Gennaro, G., van Weeren, R. J., Brunetti, G., Cassano, R., Brüggen, M., Hoeft, M., Shimwell, T. W., Röttgering, H. J. A., Bonafede, A., Botteon, A., Cuciti, V., Dallacasa, D., de Gasperin, F., Domínguez-Fernández, P., Enßlin, T. A., Gastaldello, F., Mandal, S., Rossetti, M. and Simionescu, A. (2021). Fast magnetic field amplification in distant galaxy clusters, *Nature Astronomy* **5**: 268–275.

Dobbs, C. L., Price, D. J., Pettitt, A. R., Bate, M. R. and Tricco, T. S. (2016). Magnetic field evolution and reversals in spiral galaxies, **461**(4): 4482–4495.

Dolag, K., Komatsu, E. and Sunyaev, R. (2016). SZ effects in the Magneticum Pathfinder simulation: comparison with the Planck, SPT, and ACT results, **463**(2): 1797–1811.

Dressler, A. (1980). Galaxy morphology in rich clusters: implications for the formation and evolution of galaxies., **236**: 351–365.

Dubois, Y. and Teyssier, R. (2010). Magnetised winds in dwarf galaxies, **523**: A72.

Eilek, J. A. and Owen, F. N. (2002). Magnetic Fields in Cluster Cores: Faraday Rotation in A400 and A2634, **567**(1): 202–220.

Evans, C. R. and Hawley, J. F. (1988). Simulation of Magnetohydrodynamic Flows: A Constrained Transport Model, **332**: 659.

Everett, J. E., Zweibel, E. G., Benjamin, R. A., McCammon, D., Rocks, L. and Gallagher, III, J. S. (2008). The Milky Way's Kiloparsec-Scale Wind: A Hybrid Cosmic-Ray and Thermally Driven Outflow, **674**(1): 258–270.

Federrath, C. (2016). On the universality of interstellar filaments: theory meets simulations and observations, **457**(1): 375–388.

Federrath, C., Chabrier, G., Schober, J., Banerjee, R., Klessen, R. S. and Schleicher, D. R. G. (2011). Mach Number Dependence of Turbulent Magnetic Field Amplification: Solenoidal versus Compressive Flows, **107**(11): 114504.

Federrath, C., Sur, S., Schleicher, D. R. G., Banerjee, R. and Klessen, R. S. (2011). A New Jeans Resolution Criterion for (M)HD Simulations of Self-gravitating Gas: Application to Magnetic Field Amplification by Gravity-driven Turbulence, **731**(1): 62.

Fiege, J. D. and Pudritz, R. E. (2000). Helical fields and filamentary molecular clouds - I, **311**(1): 85–104.

Field, G. B., Goldsmith, D. W. and Habing, H. J. (1969). Cosmic-Ray Heating of the Interstellar Gas, **155**: L149.

Fletcher, A. (2010). Magnetic Fields in Nearby Galaxies, *in* R. Kothes, T. L. Landecker and A. G. Willis (eds), *The Dynamic Interstellar Medium: A Celebration of the Canadian Galactic Plane Survey*, Vol. 438 of *Astronomical Society of the Pacific Conference Series*, p. 197.

Fletcher, A., Beck, R., Shukurov, A., Berkhuijsen, E. M. and Horellou, C. (2011). Magnetic fields and spiral arms in the galaxy M51, **412**(4): 2396–2416.

Fryxell, B., Olson, K., Ricker, P., Timmes, F. X., Zingale, M., Lamb, D. Q., MacNeice, P., Rosner, R., Truran, J. W. and Tufo, H. (2000). FLASH: An Adaptive Mesh Hydrodynamics Code for Modeling Astrophysical Thermonuclear Flashes, **131**(1): 273–334.

Geach, J. E., Lopez-Rodriguez, E., Doherty, M. J., Chen, J., Ivison, R. J., Bendo, G. J., Dye, S. and Coppin, K. E. K. (2023). Polarized thermal emission from dust in a galaxy at redshift 2.6, *arXiv e-prints* p. arXiv:2309.02034.

Gendelev, L. and Krumholz, M. R. (2012). Evolution of Blister-type H II Regions in a Magnetized Medium, **745**(2): 158.

Gent, F. A., Mac Low, M.-M. and Korpi-Lagg, M. J. (2024). Transition from Small-scale to Large-scale Dynamo in a Supernova-driven, Multiphase Medium, **961**(1): 7.

Girichidis, P., Seifried, D., Naab, T., Peters, T., Walch, S., Wünsch, R., Glover, S. C. O. and Klessen, R. S. (2018). The SILCC project - V. The impact of magnetic fields on the chemistry and the formation of molecular clouds, **480**(3): 3511–3540.

Godunov, S. K. (1959). A difference method for numerical calculation of discontinuous solutions of the equations of hydrodynamics, *Mat. Sb. (N.S.)* **47**(89): 271–306.

Grand, R. J. J., Gómez, F. A., Marinacci, F., Pakmor, R., Springel, V., Campbell, D. J. R., Frenk, C. S., Jenkins, A. and White, S. D. M. (2017). The Auriga Project: the properties and formation mechanisms of disc galaxies across cosmic time, **467**(1): 179–207.

Grisdale, K., Agertz, O., Romeo, A. B., Renaud, F. and Read, J. I. (2017). The impact of stellar feedback on the density and velocity structure of the interstellar medium, **466**(1): 1093–1110.

Heiles, C. and Crutcher, R. (2005). Magnetic Fields in Diffuse HI and Molecular Clouds, *in* R. Wielebinski and R. Beck (eds), *Cosmic Magnetic Fields*, Vol. 664, p. 137.

Henriksen, R. N. (2017). Magnetic spiral arms in galaxy haloes, **469**(4): 4806–4830.

Holmberg, E. (1941). On the Clustering Tendencies among the Nebulae. II. a Study of Encounters Between Laboratory Models of Stellar Systems by a New Integration Procedure., **94**: 385.

Hopkins, P. F., Kereš, D., Oñorbe, J., Faucher-Giguère, C.-A., Quataert, E., Murray, N. and Bullock, J. S. (2014). Galaxies on FIRE (Feedback In Realistic Environments): stellar feedback explains cosmologically inefficient star formation, **445**(1): 581–603.

Hopkins, P. F., Wetzel, A., Kereš, D., Faucher-Giguère, C.-A., Quataert, E., Boylan-Kolchin, M., Murray, N., Hayward, C. C., Garrison-Kimmel, S., Hummels, C., Feldmann, R., Torrey, P., Ma, X., Anglés-Alcázar, D., Su, K.-Y., Orr, M., Schmitz, D., Escala, I., Sanderson, R., Grudić, M. Y., Hafen, Z., Kim, J.-H., Fitts, A., Bullock, J. S., Wheeler, C., Chan, T. K., Elbert, O. D. and Narayanan, D. (2018). FIRE-2 simulations: physics versus numerics in galaxy formation, **480**(1): 800–863.

Hubble, E. (1926). No. 324. Extra-galactic nebulae., *Contributions from the Mount Wilson Observatory / Carnegie Institution of Washington* **324**: 1–49.

Jenkins, E. B. and Meloy, D. A. (1974). A Survey with Copernicus of Interstellar O VI Absorption, **193**: L121.

Kazantsev, A. P. (1968). Enhancement of a Magnetic Field by a Conducting Fluid, *Soviet Journal of Experimental and Theoretical Physics* **26**: 1031.

Keller, B. W., Wadsley, J. and Couchman, H. M. P. (2015). Cosmological galaxy evolution with superbubble feedback - I. Realistic galaxies with moderate feedback, **453**(4): 3499–3509.

Keller, B. W., Wadsley, J. and Couchman, H. M. P. (2016). Cosmological galaxy evolution with superbubble feedback - II. The limits of supernovae, **463**(2): 1431–1445.

Keller, B. W., Wadsley, J. W., Wang, L. and Kruijssen, J. M. D. (2019). Chaos and variance in galaxy formation, **482**(2): 2244–2261.

Kennicutt, Jr., R. C. (1998). The Global Schmidt Law in Star-forming Galaxies, **498**(2): 541–552.

Kennicutt, R. C. and Evans, N. J. (2012). Star Formation in the Milky Way and Nearby Galaxies, **50**: 531–608.

Kim, C.-G. and Ostriker, E. C. (2017). Three-phase Interstellar Medium in Galaxies Resolving Evolution with Star Formation and Supernova Feedback (TIGRESS): Algorithms, Fiducial Model, and Convergence, **846**(2): 133.

Kim, J.-h., Abel, T., Agertz, O., Bryan, G. L., Ceverino, D., Christensen, C., Conroy, C., Dekel, A., Gnedin, N. Y., Goldbaum, N. J., Guedes, J., Hahn, O., Hobbs, A., Hopkins, P. F., Hummels, C. B., Iannuzzi, F., Keres, D., Klypin, A., Kravtsov, A. V., Krumholz, M. R., Kuhlen, M., Leitner, S. N., Madau, P., Mayer, L., Moody, C. E., Nagamine, K., Norman, M. L., Onorbe, J., O'Shea, B. W., Pillepich, A., Primack, J. R., Quinn, T., Read, J. I., Robertson, B. E., Rocha, M., Rudd, D. H., Shen, S., Smith, B. D., Szalay, A. S., Teyssier, R., Thompson, R., Todoroki, K., Turk, M. J., Wadsley, J. W., Wise, J. H., Zolotov, A. and AGORA Collaboration29, t. (2014). The AGORA High-resolution Galaxy Simulations Comparison Project, **210**(1): 14.

Kim, J.-h., Agertz, O., Teyssier, R., Butler, M. J., Ceverino, D., Choi, J.-H., Feldmann, R., Keller, B. W., Lupi, A., Quinn, T., Revaz, Y., Wallace, S., Gnedin, N. Y., Leitner, S. N., Shen, S., Smith, B. D., Thompson, R., Turk, M. J., Abel, T., Arraki, K. S., Benincasa, S. M., Chakrabarti, S., DeGraf, C., Dekel, A., Goldbaum, N. J., Hopkins, P. F., Hummels, C. B., Klypin, A., Li, H., Madau, P., Mandelker, N., Mayer, L., Nagamine, K., Nickerson, S., O'Shea, B. W., Primack, J. R., Roca-Fàbrega, S., Semenov, V., Shimizu, I., Simpson, C. M., Todoroki, K., Wadsley, J. W., Wise, J. H.

and AGORA Collaboration (2016). The AGORA High-resolution Galaxy Simulations Comparison Project. II. Isolated Disk Test, **833**(2): 202.

Kim, W.-T., Ostriker, E. C. and Stone, J. M. (2003). Magnetorotationally Driven Galactic Turbulence and the Formation of Giant Molecular Clouds, **599**(2): 1157–1172.

Körtgen, B., Banerjee, R., Pudritz, R. E. and Schmidt, W. (2019). Global dynamics of the interstellar medium in magnetized disc galaxies, **489**(4): 5004–5021.

Kovacs, T. O., Mao, S. A., Basu, A., Ma, Y. K., Pakmor, R., Spitler, L. G. and Walker, C. R. H. (2024). Dispersion and rotation measures from fast radio burst (FRB) host galaxies based on the TNG50 simulation, **690**: A47.

Krause, M., Irwin, J., Schmidt, P., Stein, Y., Miskolczi, A., Carolina Mora-Partiarroyo, S., Wiegert, T., Beck, R., Stil, J. M., Heald, G., Li, J.-T., Damas-Segovia, A., Vargas, C. J., Rand, R. J., West, J., Walterbos, R. A. M., Dettmar, R.-J., English, J. and Woodfinden, A. (2020). CHANG-ES. XXII. Coherent magnetic fields in the halos of spiral galaxies, **639**: A112.

Kruijssen, J. M. D. and Longmore, S. N. (2014). An uncertainty principle for star formation - I. Why galactic star formation relations break down below a certain spatial scale, **439**(4): 3239–3252.

Kruijssen, J. M. D., Schruba, A., Hygate, A. P. S., Hu, C.-Y., Haydon, D. T. and Longmore, S. N. (2018). An uncertainty principle for star formation - II. A new method for characterizing the cloud-scale physics of star formation and feedback across cosmic history, **479**(2): 1866–1952.

Krumholz, M. R. and Matzner, C. D. (2009). The Dynamics of Radiation-pressure-dominated H II Regions, **703**(2): 1352–1362.

Li, M., Bryan, G. L. and Ostriker, J. P. (2017). Quantifying Supernovae-driven Multi-phase Galactic Outflows, **841**(2): 101.

Li, Z.-Y., Krasnopolsky, R. and Shang, H. (2011). Non-ideal MHD Effects and Magnetic Braking Catastrophe in Protostellar Disk Formation, **738**(2): 180.

Liu, G., Koda, J., Calzetti, D., Fukuhara, M. and Momose, R. (2011). The Super-linear Slope of the Spatially Resolved Star Formation Law in NGC 3521 and NGC 5194 (M51a), **735**(1): 63.

Lopez-Rodriguez, E., Borlaff, A. S., Beck, R., Reach, W. T., Mao, S. A., Ntormousi, E., Tassis, K., Martin-Alvarez, S., Clark, S. E., Dale, D. A. and del Moral-Castro, I. (2023). Extragalactic Magnetism with SOFIA (SALSA Legacy Program): The Magnetic Fields in the Multiphase Interstellar Medium of the Antennae Galaxies, **942**(1): L13.

Machida, M., Nakamura, K. E., Kudoh, T., Akahori, T., Sofue, Y. and Matsumoto, R. (2013). Dynamo Activities Driven by Magnetorotational Instability and the Parker Instability in Galactic Gaseous Disks, **764**(1): 81.

Madau, P. and Dickinson, M. (2014). Cosmic Star-Formation History, **52**: 415–486.

Maksimova, N. A., Garrison, L. H., Eisenstein, D. J., Hadzhiyska, B., Bose, S. and Satterthwaite, T. P. (2021). ABACUSSUMMIT: a massive set of high-accuracy, high-resolution N-body simulations, **508**(3): 4017–4037.

Marinacci, F., Vogelsberger, M., Mocz, P. and Pakmor, R. (2015). The large-scale properties of simulated cosmological magnetic fields, **453**(4): 3999–4019.

Marinacci, F., Vogelsberger, M., Pakmor, R., Torrey, P., Springel, V., Hernquist, L., Nelson, D., Weinberger, R., Pillepich, A., Naiman, J. and Genel, S. (2018). First results from the IllustrisTNG simulations: radio haloes and magnetic fields, **480**(4): 5113–5139.

Martin-Alvarez, S., Devriendt, J., Slyz, A., Sijacki, D., Richardson, M. L. A. and Katz, H. (2022). Towards convergence of turbulent dynamo amplification in cosmological simulations of galaxies, **513**(3): 3326–3344.

Martin-Alvarez, S., Slyz, A., Devriendt, J. and Gómez-Guijarro, C. (2020). How primordial magnetic fields shrink galaxies, **495**(4): 4475–4495.

Martizzi, D., Fielding, D., Faucher-Giguère, C.-A. and Quataert, E. (2016). Supernova feedback in a local vertically stratified medium: interstellar turbulence and galactic winds, **459**(3): 2311–2326.

McBride, J. and Heiles, C. (2013). An Arecibo Survey for Zeeman Splitting in OH Megamaser Galaxies, **763**(1): 8.

McKee, C. F. and Ostriker, J. P. (1977). A theory of the interstellar medium: three components regulated by supernova explosions in an inhomogeneous substrate., **218**: 148–169.

Mestel, L. (1966). The magnetic field of a contracting gas cloud. I,Strict flux-freezing, **133**: 265.

Mestel, L. (1968). Magnetic braking by a stellar wind-I, **138**: 359.

Moon, S., Kim, W.-T., Kim, C.-G. and Ostriker, E. C. (2023). Effects of Magnetic Fields on Gas Dynamics and Star Formation in Nuclear Rings, **946**(2): 114.

Murgia, M., Govoni, F., Feretti, L., Giovannini, G., Dallacasa, D., Fanti, R., Taylor, G. B. and Dolag, K. (2004). Magnetic fields and Faraday rotation in clusters of galaxies, **424**: 429–446.

Muzzin, A., Wilson, G., Yee, H. K. C., Gilbank, D., Hoekstra, H., Demarco, R., Balogh, M., van Dokkum, P., Franx, M., Ellingson, E., Hicks, A., Nantais, J., Noble, A., Lacy, M., Lidman, C., Rettura, A., Surace, J. and Webb, T. (2012). The Gemini Cluster Astrophysics Spectroscopic Survey (GCLASS): The Role of Environment and Self-regulation in Galaxy Evolution at z $\sim$1, **746**(2): 188.

Naab, T. and Ostriker, J. P. (2017). Theoretical Challenges in Galaxy Formation, **55**(1): 59–109.

Nakano, T. and Nakamura, T. (1978). Gravitational Instability of Magnetized Gaseous Disks 6, **30**: 671–680.

Navarro, J. F. and Benz, W. (1991). Dynamics of Cooling Gas in Galactic Dark Halos, **380**: 320.

Navarro, J. F., Frenk, C. S. and White, S. D. M. (1995). The assembly of galaxies in a hierarchically clustering universe, **275**(1): 56–66.

Ntormousi, E., Tassis, K., Del Sordo, F., Fragkoudi, F. and Pakmor, R. (2020). A dynamo amplifying the magnetic field of a Milky-Way-like galaxy, **641**: A165.

Ostriker, E. C. and Kim, C.-G. (2022). Pressure-regulated, Feedback-modulated Star Formation in Disk Galaxies, **936**(2): 137.

Ostriker, E. C., McKee, C. F. and Leroy, A. K. (2010). Regulation of Star Formation Rates in Multiphase Galactic Disks: A Thermal/Dynamical Equilibrium Model, **721**(2): 975–994.

Ostriker, E. C. and Shetty, R. (2011). Maximally Star-forming Galactic Disks. I. Starburst Regulation Via Feedback-driven Turbulence, **731**(1): 41.

Pakmor, R., van de Voort, F., Bieri, R., Gómez, F. A., Grand, R. J. J., Guillet, T., Marinacci, F., Pfrommer, C., Simpson, C. M. and Springel, V. (2020). Magnetizing the circumgalactic medium of disc galaxies, **498**(3): 3125–3137.

Papadopoulos, P. P. and Thi, W.-F. (2013). The Initial Conditions of Star Formation: Cosmic Rays as the Fundamental Regulators, *in* D. F. Torres and O. Reimer (eds), *Cosmic Rays in Star-Forming Environments*, Vol. 34 of *Astrophysics and Space Science Proceedings*, p. 41.

Parker, E. N. (1955). Hydromagnetic Dynamo Models., **122**: 293.

Pattle, K., Fissel, L., Tahani, M., Liu, T. and Ntormousi, E. (2023). Magnetic Fields in Star Formation: from Clouds to Cores, *in* S. Inutsuka, Y. Aikawa, T. Muto, K. Tomida and M. Tamura (eds), *Protostars and Planets VII*, Vol. 534 of *Astronomical Society of the Pacific Conference Series*, p. 193.

Peters, T., Naab, T., Walch, S., Glover, S. C. O., Girichidis, P., Pellegrini, E., Klessen, R. S., Wünsch, R., Gatto, A. and Baczynski, C. (2017). The SILCC project - IV. Impact of dissociating and ionizing radiation on the interstellar medium and Hα emission as a tracer of the star formation rate, **466**(3): 3293–3308.

Pillsworth, R., Roscoe, E., Pudritz, R. E. and Koch, E. W. (2025). Filamentary Hierarchies and Superbubbles. I. Characterizing Filament Properties across a Simulated Spiral Galaxy, **987**(1): 20.

Planck Collaboration (2016a). Planck 2015 results. XIII. Cosmological parameters, **594**: A13.

Planck Collaboration (2016b). Planck intermediate results. XXXV. Probing the role of the magnetic field in the formation of structure in molecular clouds, **586**: A138.

Price, D. J., Wurster, J., Tricco, T. S., Nixon, C., Toupin, S., Pettitt, A., Chan, C., Mentiplay, D., Laibe, G., Glover, S., Dobbs, C., Nealon, R., Liptai, D., Worpel, H., Bonnerot, C., Dipierro, G., Ballabio, G., Ragusa, E., Federrath, C., Iaconi, R., Reichardt, T., Forgan, D., Hutchison, M., Constantino, T., Ayliffe, B., Hirsh, K. and Lodato, G. (2018). Phantom: A Smoothed Particle Hydrodynamics and Magnetohydrodynamics Code for Astrophysics, **35**: e031.

Pudritz, R. E. and Silk, J. (1989). The Origin of Magnetic Fields and Primordial Stars in Protogalaxies, **342**: 650.

Rieder, M. and Teyssier, R. (2016). A small-scale dynamo in feedback-dominated galaxies as the origin of cosmic magnetic fields - I. The kinematic phase, **457**(2): 1722–1738.

Rieder, M. and Teyssier, R. (2017a). A small-scale dynamo in feedback-dominated galaxies - II. The saturation phase and the final magnetic configuration, **471**(3): 2674–2686.

Rieder, M. and Teyssier, R. (2017b). A small-scale dynamo in feedback-dominated galaxies - III. Cosmological simulations, **472**(4): 4368–4373.

Riols, A. and Latter, H. (2019). Gravitoturbulent dynamos in astrophysical discs, **482**(3): 3989–4008.

Robinson, H. (2021). Realistic Galaxy Simulations: Feedback, Magnetic Fields and the ISM, *M.Sc Thesis, McMaster University, http://hdl.handle.net/11375/26150* .

Rogers, H. and Pittard, J. M. (2013). Feedback from winds and supernovae in massive stellar clusters - I. Hydrodynamics, **431**(2): 1337–1351.

Saintonge, A., Kauffmann, G., Wang, J., Kramer, C., Tacconi, L. J., Buchbender, C., Catinella, B., Graciá-Carpio, J., Cortese, L., Fabello, S., Fu, J., Genzel, R., Giovanelli, R., Guo, Q., Haynes, M. P., Heckman, T. M., Krumholz, M. R., Lemonias, J., Li, C., Moran, S., Rodriguez-Fernandez, N., Schiminovich, D., Schuster, K. and Sievers, A. (2011). COLD GASS, an IRAM legacy survey of molecular gas in massive galaxies - II. The non-universality of the molecular gas depletion time-scale, **415**(1): 61–76.

Scannapieco, C., Wadepuhl, M., Parry, O. H., Navarro, J. F., Jenkins, A., Springel, V., Teyssier, R., Carlson, E., Couchman, H. M. P., Crain, R. A., Dalla Vecchia, C., Frenk, C. S., Kobayashi, C., Monaco, P., Murante, G., Okamoto, T., Quinn, T., Schaye, J., Stinson, G. S., Theuns, T., Wadsley, J., White, S. D. M. and Woods, R. (2012). The Aquila comparison project: the effects of feedback and numerical methods on simulations of galaxy formation, **423**(2): 1726–1749.

Schawinski, K., Urry, C. M., Simmons, B. D., Fortson, L., Kaviraj, S., Keel, W. C., Lintott, C. J., Masters, K. L., Nichol, R. C., Sarzi, M., Skibba, R., Treister, E., Willett, K. W., Wong, O. I. and Yi, S. K. (2014). The green valley is a red herring: Galaxy Zoo reveals two evolutionary pathways towards quenching of star formation in early- and late-type galaxies, **440**(1): 889–907.

Schaye, J., Crain, R. A., Bower, R. G., Furlong, M., Schaller, M., Theuns, T., Dalla Vecchia, C., Frenk, C. S., McCarthy, I. G., Helly, J. C., Jenkins, A., Rosas-Guevara,

Y. M., White, S. D. M., Baes, M., Booth, C. M., Camps, P., Navarro, J. F., Qu, Y., Rahmati, A., Sawala, T., Thomas, P. A. and Trayford, J. (2015). The EAGLE project: simulating the evolution and assembly of galaxies and their environments, **446**(1): 521–554.

Schekochihin, A. A., Haugen, N. E. L., Brandenburg, A., Cowley, S. C., Maron, J. L. and McWilliams, J. C. (2005). The Onset of a Small-Scale Turbulent Dynamo at Low Magnetic Prandtl Numbers, **625**(2): L115–L118.

Schmidt, M. (1959). The Rate of Star Formation., **129**: 243.

Schober, J., Schleicher, D. R. G. and Klessen, R. S. (2013). Magnetic field amplification in young galaxies, **560**: A87.

Schruba, A., Leroy, A. K., Walter, F., Bigiel, F., Brinks, E., de Blok, W. J. G., Dumas, G., Kramer, C., Rosolowsky, E., Sandstrom, K., Schuster, K., Usero, A., Weiss, A. and Wiesemeyer, H. (2011). A Molecular Star Formation Law in the Atomic-gas-dominated Regime in Nearby Galaxies, **142**(2): 37.

Seta, A., Rodrigues, L. F. S., Federrath, C. and Hales, C. A. (2021). Magnetic Fields in Elliptical Galaxies: An Observational Probe of the Fluctuation Dynamo Action, **907**(1): 2.

Shukurov, A., Rodrigues, L. F. S., Bushby, P. J., Hollins, J. and Rachen, J. P. (2019). A physical approach to modelling large-scale galactic magnetic fields, **623**: A113.

Springel, V. (2005). The cosmological simulation code GADGET-2, **364**(4): 1105–1134.

Springel, V. (2010). E pur si muove: Galilean-invariant cosmological hydrodynamical simulations on a moving mesh, **401**(2): 791–851.

Springel, V., Pakmor, R., Pillepich, A., Weinberger, R., Nelson, D., Hernquist, L., Vogelsberger, M., Genel, S., Torrey, P., Marinacci, F. and Naiman, J. (2018). First results from the IllustrisTNG simulations: matter and galaxy clustering, **475**(1): 676–698.

Steenbeck, M. and Krause, F. (1969). On the Dynamo Theory of Stellar and Planetary Magnetic Fields. I. AC Dynamos of Solar Type, *Astronomische Nachrichten* **291**: 49–84.

Steinwandel, U. P., Dolag, K., Böss, L. M. and Marin-Gilabert, T. (2024). Toward Cosmological Simulations of the Magnetized Intracluster Medium with Resolved Coulomb Collision Scale, **967**(2): 125.

Steinwandel, U. P., Dolag, K., Lesch, H., Moster, B. P., Burkert, A. and Prieto, A. (2020). On the origin of magnetic driven winds and the structure of the galactic dynamo in isolated galaxies, **494**(3): 4393–4412.

Stinson, G., Seth, A., Katz, N., Wadsley, J., Governato, F. and Quinn, T. (2006). Star formation and feedback in smoothed particle hydrodynamic simulations - I. Isolated galaxies, **373**(3): 1074–1090.

Stix, M. (1975). The galactic dynamo., **42**(1): 85–89.

Stone, J. M., Gardiner, T. A., Teuben, P., Hawley, J. F. and Simon, J. B. (2008). Athena: A New Code for Astrophysical MHD, **178**(1): 137–177.

Subramanian, K. (1998). Can the turbulent galactic dynamo generate large-scale magnetic fields?, **294**: 718–728.

Sur, S., Bhat, P. and Subramanian, K. (2018). Faraday rotation signatures of fluctuation dynamos in young galaxies, **475**(1): L72–L76.

Tabatabaei, F. S., Schinnerer, E., Krause, M., Dumas, G., Meidt, S., Damas-Segovia, A., Beck, R., Murphy, E. J., Mulcahy, D. D., Groves, B., Bolatto, A., Dale, D., Galametz, M., Sandstrom, K., Boquien, M., Calzetti, D., Kennicutt, R. C., Hunt, L. K., De Looze, I. and Pellegrini, E. W. (2017). The Radio Spectral Energy Distribution and Star-formation Rate Calibration in Galaxies, **836**(2): 185.

Tasker, E. J., Wadsley, J. and Pudritz, R. (2015). Star Formation in Disk Galaxies. III. Does Stellar Feedback Result in Cloud Death?, **801**(1): 33.

Teyssier, R. (2002). Cosmological hydrodynamics with adaptive mesh refinement. A new high resolution code called RAMSES, **385**: 337–364.

Tielens, A. G. G. M. (2010). *The Physics and Chemistry of the Interstellar Medium*.

Toomre, A. and Toomre, J. (1972). Galactic Bridges and Tails, **178**: 623–666.

Tremmel, M., Karcher, M., Governato, F., Volonteri, M., Quinn, T. R., Pontzen, A., Anderson, L. and Bellovary, J. (2017). The Romulus cosmological simulations: a physical approach to the formation, dynamics and accretion models of SMBHs, **470**(1): 1121–1139.

Tritsis, A., Panopoulou, G. V., Mouschovias, T. C., Tassis, K. and Pavlidou, V. (2015). Magnetic field-gas density relation and observational implications revisited, **451**(4): 4384–4396.

Vainshtein, S. I. and Ruzmaikin, A. A. (1972). Generation of the Large-Scale Galactic Magnetic Field., **15**: 714.

Vogelsberger, M., Genel, S., Springel, V., Torrey, P., Sijacki, D., Xu, D., Snyder, G., Nelson, D. and Hernquist, L. (2014). Introducing the Illustris Project: simulating the coevolution of dark and visible matter in the Universe, **444**(2): 1518–1547.

Wadsley, J. W., Keller, B. W. and Quinn, T. R. (2017). Gasoline2: a modern smoothed particle hydrodynamics code, **471**(2): 2357–2369.

Wadsley, J. W., Stadel, J. and Quinn, T. (2004). Gasoline: a flexible, parallel implementation of TreeSPH, **9**(2): 137–158.

Walch, S., Girichidis, P., Naab, T., Gatto, A., Glover, S. C. O., Wünsch, R., Klessen, R. S., Clark, P. C., Peters, T., Derigs, D. and Baczynski, C. (2015). The SILCC (SImulating the LifeCycle of molecular Clouds) project - I. Chemical evolution of the supernova-driven ISM, **454**(1): 238–268.

Wang, P. and Abel, T. (2009). Magnetohydrodynamic Simulations of Disk Galaxy Formation: The Magnetization of the Cold and Warm Medium, **696**(1): 96–109.

Weaver, R., McCray, R., Castor, J., Shapiro, P. and Moore, R. (1977). Interstellar bubbles. II. Structure and evolution., **218**: 377–395.

Whitworth, D. J., Srinivasan, S., Pudritz, R. E., Mac Low, M. M., Eadie, G., Palau, A., Soler, J. D., Smith, R. J., Pattle, K., Robinson, H., Pillsworth, R., Wadsley, J., Brucy, N., Lebreuilly, U., Hennebelle, P., Girichidis, P., Gent, F. A., Marin, J., Sánchez Valido, L., Camacho, V., Klessen, R. S. and Vázquez-Semadeni, E. (2025). On the relation between magnetic field strength and gas density in the interstellar medium: a multiscale analysis, **540**(3): 2762–2786.

Wibking, B. D. and Krumholz, M. R. (2023). The global structure of magnetic fields and gas in simulated Milky Way-analogue galaxies, **521**(4): 5972–5990.

Widrow, L. M. (2002). Origin of galactic and extragalactic magnetic fields, *Reviews of Modern Physics* **74**(3): 775–823.

Wissing, R. and Shen, S. (2023). Numerical dependencies of the galactic dynamo in isolated galaxies with SPH, **673**: A47.

Wolfire, M. G., McKee, C. F., Hollenbach, D. and Tielens, A. G. G. M. (2003). Neutral Atomic Phases of the Interstellar Medium in the Galaxy, **587**(1): 278–311.

Wurster, J., Price, D. J. and Bate, M. R. (2016). Can non-ideal magnetohydrodynamics solve the magnetic braking catastrophe?, **457**(1): 1037–1061.

Xu, H., O'Shea, B. W., Collins, D. C., Norman, M. L., Li, H. and Li, S. (2008). The Biermann Battery in Cosmological MHD Simulations of Population III Star Formation, **688**(2): L57.

Zeldovich, I. B. and Ruzmaikin, A. A. (1980). Magnetic field of a conducting fluid in two-dimensional motion, *Zhurnal Eksperimentalnoi i Teoreticheskoi Fiziki* **78**: 980–986.

Zeldovich, Y. B., Ruzmaikin, A. A. and Sokoloff, D. D. (1990). *The almighty chance*.

Zweibel, E. G. (2013). The microphysics and macrophysics of cosmic rays, *Physics of Plasmas* **20**(5): 055501.

Chapter 2

Regulating Star Formation in a Magnetized Disk Galaxy

The content of this chapter is a second revision of the manuscript text for publication under the following citation:

Robinson, H. (2024). Regulating star formation in a magnetized disc galaxy. Monthly Notices of the Royal Astronomical Society, 534(2), 1420-1432.

Regulating Star Formation in a Magnetized Disk Galaxy

Hector Robinson
Department of Physics and Astronomy
McMaster University, Hamilton, ON, Canada
Email: robinh4@mcmaster.ca

James Wadsley
Department of Physics and Astronomy
McMaster University
Email: wadsley@mcmaster.ca

Abstract

We use high-resolution MHD simulations of isolated disk galaxies to investigate the co-evolution of magnetic fields with a self-regulated, star-forming interstellar medium (ISM). The simulations are conducted using the Ramses AMR code on the standard Agora initial condition, with gas cooling, star formation and feedback. We run galaxies with a variety of initial magnetic field strengths. The fields evolve and achieve approximate saturation within 500 Myr, but at different levels. The galaxies reach a quasi-steady state, with slowly declining star formation due to both gas consumption and increases in the field strength at intermediate ISM densities. We connect this behaviour to differences in the gas properties and overall structure of the galaxies. Stronger magnetic fields limit supernova bubble sizes. Different cases support the ISM using varying combinations of magnetic pressure, turbulence and thermal energy. Initially > 1 μG magnetic fields evolve modestly and dominate support at all radii. Conversely, initially weaker fields grow through feedback and turbulence but never dominate the support. This is reflected in the stability of the gas disk. This interplay determines the overall distribution of star formation in each case. We conclude that an initially weak field can grow to produce a realistic model of a local disk galaxy, but starting with typically assumed field strengths (> 1 μG) will not.

Keywords: *Methods: numerical – MHD – ISM: magnetic fields – Galaxies: star formation*

2.1 Introduction

Magnetic fields have been detected at all scales in astrophysics (Han; 2017) and are predicted to play important roles in galaxy evolution. A key question is what role magnetic fields play in regulating galactic star formation. The most straightforward consideration is that magnetic fields provide an additional pressure which can support gas against gravitational collapse on the scale of a galactic disk, but they can also affect galaxy-scale dynamics, the properties of turbulence, the effectiveness of stellar feedback, and the formation of molecular clouds. Importantly, turbulence acts to amplify and reshape the magnetic field, so in practice we must study the joint evolution of the magnetic field and the ISM together.

Detecting magnetic fields in galaxies is challenging. A diverse set of methods allows us to infer differing aspects of the field. These include synchrotron emission, the Zeeman effect, Faraday rotation, polarised thermal emission of magnetically aligned dust grains (Pattle et al.; 2023), and polarised emission of starlight due to extinction by aligned dust grains.

Of primary interest is the field strength. Synchrotron observations can be used to estimate total magnetic field strengths by assuming energy equipartition between magnetic fields and cosmic ray particles. Fields strengths measured in spiral galaxies with this method tend to be around $\sim$10 μG and decrease slowly with galactocentric radius (Fletcher et al.; 2011; Basu and Roy; 2013; Beck and Wielebinski; 2013). The dependence on the poorly constrained cosmic ray distribution means both the field strength and gradient are highly uncertain. Due to the diffusive nature and resulting large scale height of cosmic rays, it is expected to probe a thick volume around the galactic disk (Zweibel; 2017).

In the Milky-Way and a few nearby galaxies, line-of-sight magnetic field strengths have also been measured via the Zeeman effect (Crutcher et al.; 2010), which causes emission lines to split when molecules are in the presence of line of-sight magnetic fields. Zeeman observations in the Milky-Way have found fields strengths of ~ 10 μG at number densities of 10-100 cm^{-3}, In gas at number densities > 1000 cm^{-3} the upper envelope to the field strength scales with number density as $B \propto n^{0.5-0.7}$ (Crutcher et al.; 2010).

There is considerable spread in these measurements for 10-1000 cm^{-3}. It is commonly assumed that typical field strengths remain flat at lower densities.

The remaining techniques mostly indicate the field morphology. Many observations find large-scale spiral patterns in galactic magnetic fields, even in galaxies that do not have optical spiral structures (Chyży and Buta; 2008; Beck et al.; 2019; Lopez-Rodriguez et al.; 2023). Down to $\sim$ 100 pc scales, the fields tend to be aligned parallel with the structure, such as low density filaments (Goldsmith et al.; 2008; Sugitani et al.; 2011). These results have been confirmed more recently by synchrotron maps of molecular clouds in the Milky way (Planck Collaboration; 2016).

There are many theoretical predictions for how magnetic fields should evolve and affect their host galaxies. Tiny cosmic seed fields are amplified exponentially to detectable levels within a few Gyr (Geach et al.; 2023). On small galactic scales, the turbulent dynamo is expected be ubiquitous. It can exponentially amplify field strengths over timescales of $<$ 10 Myr, saturating at level that is a fraction of the turbulent energy (Federrath et al.; 2011; Rieder and Teyssier; 2016). The $\alpha - \Omega$ dynamo is expected to order the small scale turbulent fields into disk scale regular fields over Gyr timescales (Brandenburg and Subramanian; 2005). At intermediate scales there is also the gravitational-instability dynamo associated with spiral structures (Riols and Latter; 2019). Amplification rates in simulations are still highly dependent on numerical resolution and feedback methods (Rieder and Teyssier; 2016), which can make comparisons between different simulations difficult, however the level they saturate at appears to be independent of those effects. Thus saturated fields present an appealing target for study that is less dependent on numerical method differences.

After saturation, the energy density of magnetic fields relative to other sources can vary depending on the phase of gas. The diffuse medium can have significant magnetic support, meaning that the magnetic pressure is comparable to thermal pressure (plasma $\beta \sim 1$). At higher densities, where gas is colder, the primary support is turbulent and the clouds are typically magnetically supercritical ($E_{mag} < E_{grav} \sim E_{turb}$) (see review by Beck and Wielebinski 2013).

Magnetic fields are expected to play a key role in how gas transitions between phases within the ISM (Krumholz and Federrath; 2019). This manifests as a difference in the distribution of gas densities in the ISM, which are created by turbulent compression and expansion. Supersonic turbulence is expected to develop a lognormal probability density function (PDF) that is also seen in observations (Kainulainen et al.; 2009). At high

densities when the gas becomes gravitationally unstable, it diverges from the lognormal (Burkhart; 2018). Magnetic pressure narrows the width of the PDF by resisting turbulence's ability to compress gas. Simulations on cloud and kpc scales have shown that this effect can reduce star formation rates by a factor of 2-3 (Federrath and Klessen; 2012; Padoan et al.; 2012; Girichidis et al.; 2018; Krumholz and Federrath; 2019; Hix et al.; 2023; Kim et al.; 2023). Turbulence also plays a role in the magnetic field strength vs. gas density scaling relations. The 0.5-0.7 power law was originally thought to come from gravitational contraction, but cloud-scale simulations by Cao and Li (2023) retrieve the same scaling without self gravity and the authors argue it comes from turbulent compression instead. A key takeaway from this discussion is that the role of magnetic fields on smaller scales is complex and under intense study. Working on slightly larger, galactic scales, allows for a simpler treatment of star formation.

MHD simulations are a powerful tool for studying magnetic fields on many scales. On cosmological scales, magnetic fields are generally not dynamically dominant but some simulations have begun to include them (Grand et al.; 2017; Hopkins et al.; 2018; Steinwandel et al.; 2022; Martin-Alvarez et al.; 2018). Cosmological seed fields are the origin of all galactic fields; thus cosmological simulations can be used to test models of magnetic field amplification and produce toroidally dominated fields similar to those seen in observations (Rieder and Teyssier; 2017b). One difficulty with cosmological simulations is that magnetic fields amplify strongly during the poorly resolved and highly chaotic infall and merging phases. These processes apply ongoing, significant perturbations to the state of the galaxy. There is also the computational expense of simulating a large cosmological environment for the full history of the universe.

An alternative approach is high resolution simulations of individual galaxies, including the effects of magnetic fields. Körtgen et al. (2019) simulated an isolated disk galaxy and showed that magnetic fields can speed up disk fragmentation and drive outflows hundreds of parsecs above the disk even without stellar feedback. Galaxies that have both star formation and feedback tend to have lower star formation rates when MHD is also included and can magnetize their CGM with magnetic outflows (Steinwandel et al.; 2019, 2020; Pakmor et al.; 2020; Wissing and Shen; 2023), suggesting that MHD can help regulate star formation on disk scales. Recent simulations also suggest that the magnetic field strength continuously declines with density, effectively as a power law, extending to densities below the point where observationally inspired models suggest it should become constant (e.g. (Ponnada et al.; 2022)).

Prior work has tended to focus on amplification rates and the final magnetic configuration (e.g. Rieder and Teyssier; 2017a; Su et al.; 2018). However, it is also important consider how magnetic fields affect the state of the gas in the multiphase interstellar medium and whether the star formation is regulated in the same way as we introduce progressively stronger fields.

In this paper we present a controlled study, simulating an isolated galaxy with a well-known initial condition, with and without magnetic fields, with several different initial field strengths. Thus we can focus on the development and co-evolution of magnetic fields due to self-regulated star formation and feedback in a galactic disk. By running such cases for several dynamical times, we expect to produce a steady-state, self regulated star-forming ISM to study. In addition, by using a standard setup and simple, well-tested star formation and feedback models, we aim to make the interpretation more straightforward.

The remainder of the paper is organized as follows: In section 3.2, we describe the simulation method and magnetized galaxy setup. In section 2.3.1, we analyse the evolution of the magnetic field in each galaxy, including the approach to a saturated state and comparing the strengths to observations. We examine the resulting visual appearance of each galaxy in section 2.3.2. In section 2.3.3, we examine the overall star formation and its radial distribution in each case. We then explore how this is reflected in their ISM. Section 2.3.4 examines the gas properties, seeking to determine the underlying drivers of the differences in star formation rates and their connection to the magnetic fields and other forms of support for the gas. In section 2.3.5, we study the combined effect of the different support mechanisms on the gravitational stability of the galactic disks. In section 2.4 we discuss our results and future work. Finally we summarize our conclusions in section 2.5.

2.2 Simulation Method

We conduct magnetohydrodynamic (MHD) simulations of isolated galaxies using the adaptive mesh refinement (AMR) code Ramses (Teyssier; 2002) to solve the ideal MHD equations using an HLLD approximate Riemann solver (Miyoshi and Kusano; 2005). The solenoidal constraint ($\nabla \cdot B = 0$) is enforced with the constrained transport method (Evans and Hawley; 1988). The dynamics of stars and dark matter are solved using the particle-mesh technique (Hockney and Eastwood; 1981). Gas cooling and heating is included via the Grackle chemistry and cooling library (Smith et al.; 2017). Grackle

uses metal cooling rates tabulated from output from the photo-ionization code CLOUDY (Ferland et al.; 2017). We also include a photoelectric heating rate of $\zeta = 4 \times 10^{-26}$ erg cm^{-3} s^{-1}, which allows for a two-phase ISM similar to that proposed by Wolfire et al. (2003).

2.2.1 Initial Conditions and Refinement

The galaxies we simulate are all based on the medium-resolution isolated disk galaxy from the AGORA Project (Kim et al.; 2016), but with an initial magnetic field added. It has an active dark matter halo ($M_{200} = 1.074 \times 10^{12}M_\odot$) that follows an NFW profile, a stellar bulge ($M_B = 4.297 \times 10^9$M$_\odot$) that follows a Hernquist profile, and a disk ($M_D = 4.297 \times 10^{10}M_\odot$) that is 80% stars and 20% gas by mass with a density profile given by

$$\rho_{\rm gas}(r, z) = \rho_0 e^{(-r/r_d)} e^{(-|z|/z_d)} \tag{2.1}$$

With $\rho_0 = M_{\rm gas}/(4\pi r_d^2 z_d)$, where $r_d = 3.432$ kpc and $z_d = 0.1 r_d$. The stellar and dark matter components are modeled with collisionless particles, and the gas is initiated on a RAMSES AMR Grid. Kim et al. (2016) contains fulls details about the disk setup.

This initial condition has been described as similar to 'Milky-Way like' spiral galaxy with a redshift of z∼1. However, the dark matter halo and rotation curve are quite similar to a $z \sim 0$ large disk galaxy, such as NGC 5055 (the Sunflower galaxy). The initial surface densities of gas and stars are also quite similar to NGC 5055 (as noted by Benincasa et al. 2020). In this sense it is actually a reasonable proxy for a nearby spiral galaxy.

The gas disk is initialized inside of a domain 600 kpc on a side that has a base grid of 64^3 cells, that is allowed to refine an additional 10 levels which gives a spatial resolution of 9.15 pc at the highest level. A cell will refine if it contains more than 10,000 M$_\odot$ of gas or if it contains more than 8 collisionless particles. The disk starts off with $M_{\rm gas} = 8.59 \times 10^9$ M$_\odot$, which will decrease throughout the simulation as gas is converted into stars. The gas is initialized to a temperature of 10,000 K and solar metallicity.

Inside the gas disk, we initialize a magnetic field with a morphology that is purely toroidal, containing no vertical or radial components. The field strength scales with gas density as

$$B = B_0 \left(\frac{\rho}{\rho_0} \right)^{2/3} \tag{2.2}$$

Name	B_{ISM}	β_{ISM}	B_0
Hydro	0	∞	0
MHD Weak	0.1 μG	800	0.85 μG
MHD Medium	1 μG	8	8.5 μG
MHD Strong	10 μG	0.08	85 μG

TABLE 2.1: Summary of initial magnetic properties of each simulation. B_{ISM} and β_{ISM} are magnetic field and plasma β values, respectively, in the typical ISM (gas density $n \sim 0.25$ cm^{-3}). B_0 is the corresponding magnetic field strength in equation 3.2 (at the geometric center of the galaxy). Otherwise initial magnetic field strengths scale as $B \propto \rho^{2/3}$. As a result of this scaling, the plasma β ($P_{thermal}/P_{mag}$) increases with radius.

B_0 is the value of the magnetic field strength on the midplane at the center of the galaxy. The magnetic field strength decreases further out in the disk, decreasing by a factor of 10 by 12 kpc. Due to the grid initialization process, some initial B values are changed by $\pm$ 10%. Figure 2.1 includes radial profiles of the initial magnetic field strength (straight red lines).

We simulate four galaxies which are identical except for the initial magnetic field, with values for each case summarized in Table 2.1. The first case has zero initial magnetic field, equivalent to being simulated with regular hydrodynamics. The remaining three galaxies are referred to as MHD Weak, MHD Medium, and MHD Strong. In each of them, the field strength initially scales with gas density according to equation 3.2, but the constant B_0 is modified so that the MHD Medium has fields 10 times stronger than the MHD Weak, and MHD Strong has fields 10 times stronger than MHD Medium. An increase of 10 times in magnetic field strength corresponds to an increase of 100 times in magnetic energy.

2.2.2 Star Formation and Feedback

Stars particles are formed stochastically via a Schmidt-law of the form

$$\frac{d\rho_*}{dt} = \frac{\epsilon_{\rm ff}\rho}{t_{\rm ff}} \quad \text{if} \quad \rho > \rho_{\rm crit} \tag{2.3}$$

where ρ_* is the stellar density, $\epsilon_{\rm ff}$ is the star formation efficiency per free-fall time which we set to $\epsilon_{ff} = 0.1$, and $\rho_{\rm crit}$ is a threshold density which corresponds to a number

density of 100 cm^{-3}.

Stellar feedback is entirely supernovae (SN), injected as thermal energy 5 Myr after stars first form with 10^{51} erg per 91 $M_\odot$ of young stars. This energy is treated via the delayed cooling model of Agertz et al. (2011), which allows unresolved superbubbles to grow correctly by initially treating hot supernova ejecta as unresolved, non-cooling bubbles whose energy is converted to regular thermal energy with a e-folding time of 5 Myr. At the chosen resolution, other forms of feedback are largely unresolved, as are the dense structures in which they would chiefly operate.

We note that these choices differ from the original AGORA simulations (Kim et al.; 2016). In particular, AGORA used a low efficiency ($\epsilon_{ff} = 0.01$) in dense gas. This pushes the characteristic time for star formation to ~ 1 Gyr, effectively forcing a typical overall galactic star formation rate (SFR), that was the same with or without feedback. With $\epsilon_{ff} = 0.1$, stellar feedback is necessary to regulate star formation to the level expected for typical disk galaxies (Agertz and Kravtsov; 2015; Semenov et al.; 2018; Robinson; 2021). Feedback is expected to couple in such a way to reproduce large scale ISM properties including the scale height (Ostriker et al.; 2010; Benincasa et al.; 2016). We choose this simple, robust approach to star formation and feedback because it reliably produces self-regulated galaxies with sensible star formation rates in the hydrodynamic case, where it widely-used. This allows us to focus on the effects of MHD.

Each galaxy was evolved for 1 Gyr, corresponding to a handful dynamical times at the outer radius. The inner regions were expected to evolve rapidly and then settle into a quasi-steady state of ongoing star formation. Thus the goal was to produce an interval of several 100 Myr to study this relatively quiet, self-regulated state in each case.

2.3 Simulation results

At the start of the simulation, all four galaxies begin their evolution by settling from the slightly unstable initial state by compressing vertically. While this happens cold-phase gas condenses and fragments along spiral arms into individual clouds. In the Hydro and MHD Weak cases, this collapse is violent and results in a starburst, mostly localized to the galactic center ($r < 2$ kpc). In the cases with stronger fields, the fields resist the compression, preventing a starburst from occurring, and the onset of star formation is delayed. As a result, the Hydro and MHD Weak galaxies have a smaller fraction of gas remaining in the galactic center for the remainder of the simulation, for this reason we

exclude the center 2 kpc from some of our analysis to ensure a fair comparison between the galaxies.

2.3.1 Magnetic Field Evolution

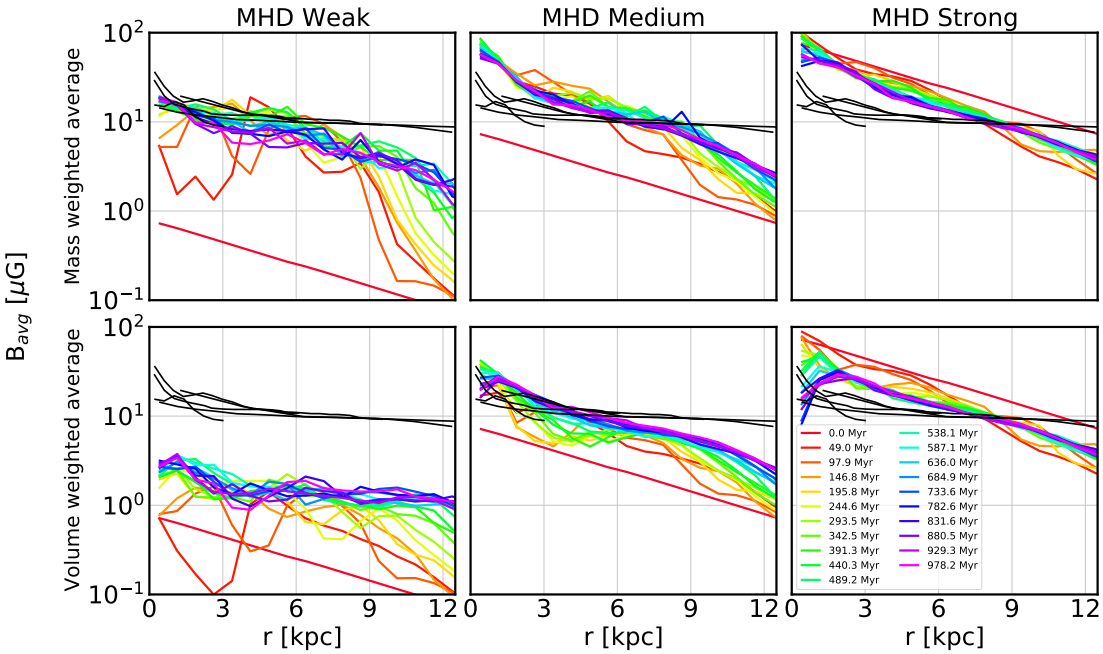

FIGURE 2.1: Magnetic field strength vs. galactocentric radius in each MHD galaxy. Top row shows a mass-weighted average, and bottom row shows a volume-weighted average. Color shows the the time of the snapshot from 0 (red), to 1 Gyr (pink). Black lines are data from nearby galaxies from Basu and Roy (2013). Field strengths are calculated in a disk with a height of 1 kpc.

The primary focus of this work is how magnetic fields influence the structure of the ISM and the regulation of star formation at later stages. Before examining that we give a brief overview of the magnetic field evolution leading to the final state.

Figure 2.1 shows the average magnetic field strength vs. radius in a disk of height 1 kpc for each galaxy over time, and compares them to field strengths from synchrotron observations by Basu and Roy (2013). Firstly, we note that this observational sample includes NGC 5055, for which the simulation set-up is a reasonable proxy. Secondly, the variation among the observational sample is also quite small, with estimated field strengths of $\sim$ 10-20 μG in the radii of interest, 2-10 kpc.

The figure includes two methods of calculating the average field strength. The first is a mass-weighted average (top panels) and the second is a volume weighted average (lower panels). The mass weighted average gives an estimate of the field strengths in high-density regions, while the volume weighted average probes more typical ISM densities. The method of averaging does not particularly affect the field estimate in the MHD Strong galaxy because the gas scale height is quite large, and there is very little high density gas created. (see 2.3.4 for a quantitative comparison). For weaker fields, the galaxies are thinner and the differences more pronounced.

The volume weighted average provides a better comparison to the observed estimates because synchrotron emission arises from cosmic rays which are typically assumed to have a large scale height (Zweibel; 2017). Many assumptions are required to calculate field strengths from synchrotron emission. A common choice is energy equipartition between the magnetic and cosmic ray energies (Basu and Roy; 2013). There are also uncertainties in the effective volume of the synchrotron emitting disk. These assumptions most strongly affect the amplitude of the estimated field strength. The diffusive nature of cosmic rays tends to limit their radial variation. The estimated radial slope depends most sensitively on the observed synchrotron intensity profiles which drive the relatively flat slopes seen in the observation estimates (black curves) in figure 2.1. The MHD Weak galaxy is promising in this regard because the volume weighted average achieves a flat radial profile like the observations. However, the fields saturate around 1 μG for most of the disk, whereas the observations have been used to infer 10 μG using the previously discussed assumptions. It may be worth revisiting these assumptions, particularly equipartition. These results also suggest that initial fields must be well below equipartition in order to naturally evolve to a realistic saturated state that reproduces the radial profile.

Similar amounts of magnetic field amplification are visible in both the MHD Weak and MHD Medium galaxies regardless of the choice of weighting. The MHD Strong galaxy experiences a net loss of field strength over time, confirming that it was oversaturated from the beginning. Both the MHD Weak and Medium galaxies appear close saturation after about 500 Myr, but they do not saturate at the same value. Field strengths may decrease over time due to magnetic flux leaving the disk. In the inner regions of the MHD Weak galaxy, field strengths peak at around t=500 Myr and then decrease slightly due to flux leaving in vertical outflows. In the MHD Strong galaxy, net flux loss is expected due to magnetic braking.

In all cases, the amplification rate is lower in the outer disk, where there is less star

formation (see section 2.3.3). This behaviour is most consistent with a turbulent style dynamo, both in terms of the rate of growth and the strong association with feedback from star formation.

Our field strengths can also be compared to those inferred from Zeeman measurements, by placing them on a field strength vs. density (B vs. n) plot, shown in figure 2.2. There are a few caveats when comparing to Zeeman measurements. First, those observations typically probe dense, mostly neutral and molecular gas that is not present in these simulations (see section 2.3.4). Secondly, non-ideal processes such as turbulent ambipolar diffusion are expected to remove field in dense neutral gas (Heitsch et al.; 2004). Additionally, the high density gas is within an order of magnitude of our resolution limit, so numerical diffusion may also begin to play a role. Thus the numerical results are best interpreted as upper bounds for densities, $n > 100$ cm^{-3}. We plot the median field strength in each density bin, but variations of an order of magnitude are common at a given density. In this figure, field amplification due to dynamo action is seen as a vertical translation. When field strengths increase due to gas compression (or expansion), the points should also move to the right as the density increases (or decreases, respectively). This largely explains the rapid expansion of the plot upward in density and field strength after the initial state. In the highest density gas field strengths remain similar across all three simulations. This is likely due to the fact that the field strength in the dense gas immediately saturates. This dense gas is selectively where star formation occurs, driving turbulence which would feed a rapid, small scale dynamo (See figure 2.10). Amplification is clearly visible in the diffuse medium with number densities of 0.1-10 cm^{-3}. There are differing levels of amplification seen in the diffuse medium in each case. The 2/3 power-law slope is maintained in the diffuse medium as the field evolves. There is a shallower power-law slope for intermediate density gas (1-100 cm^{-3}), which is flatter in the stronger field cases. The stronger field forces gas flows along field lines, limiting field increases due to density changes.

At low densities, the simulated field strengths continue to decrease with density, showing no hint of the constant 10 μG field extrapolation below number densities of ~ 10 cm^{-3} assumed by, e.g. Crutcher et al. (2010).

2.3.2 Overall structure

We now proceed with an examination of the state of the galaxies after 1 Gyr of evolution. Figure 2.3 shows face-on visualisations of each galaxy. The top row shows the surface densities of gas in each galaxy. The excess of gas in the medium and strong galaxies is

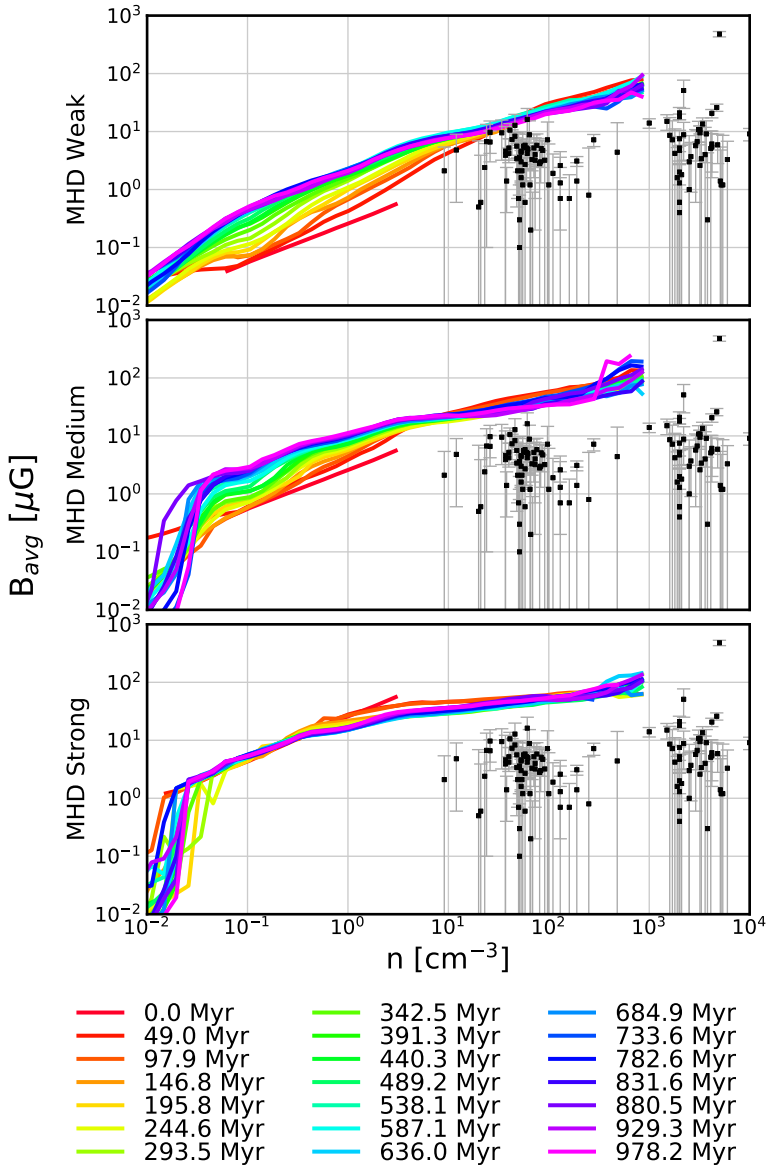

FIGURE 2.2: Median magnetic field strength vs. gas number density over time. Black points are measured values from clouds inside the Milky Way (Crutcher et al.; 2010). Amplification is visible in diffuse gas in galaxies with weaker initial fields.

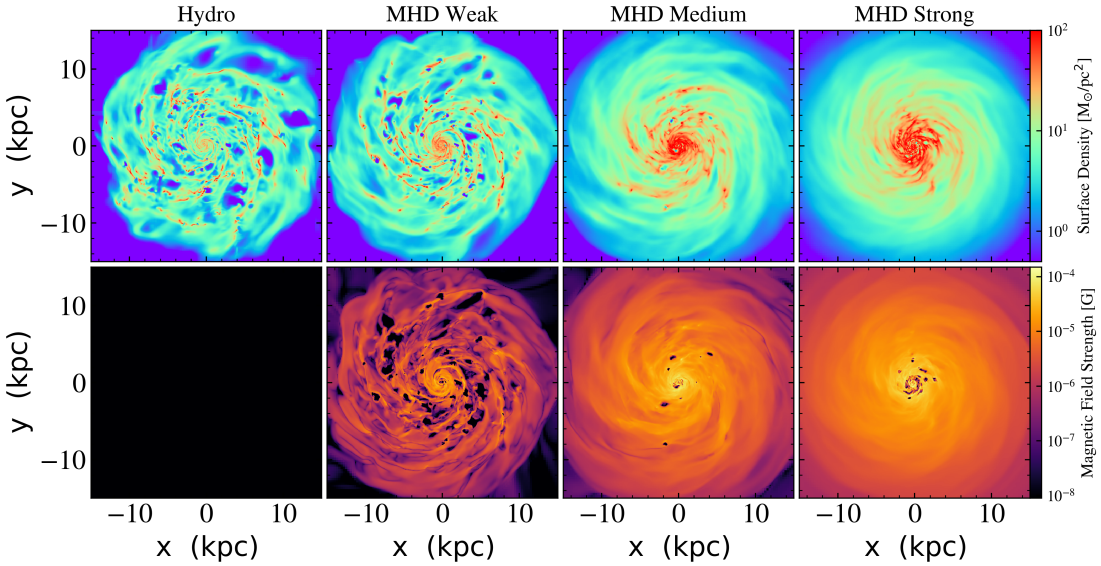

FIGURE 2.3: Visualizations of each galaxy 1 Gyr. The top row shows surface density projections, and the bottom row shows slices of magnetic field strength in the midplane. The Hydro case is black because there is zero magnetic fields everywhere.

clearly visible. Those galaxies also appear less fragmented, with more flocculent spiral arms and fewer superbubble holes. The bottom row shows slices of the magnetic field strength in the midplane of the galactic disk. Although there is some amplification of the fields during the galaxies evolution, the fields do not saturate at the same level and the case with the stronger initial fields still has the strongest magnetic fields at the end of the run. The stronger magnetic fields have less structure in them, mostly due to them having lower star formation rates (see section 2.3.3), but also due to the weaker fields being less dynamically important and having less resistance to being pushed around by motions of the gas. Large scale spiral structure is reflected in the magnetic fields, and the stronger field cases result in spiral morphology that is less disrupted by superbubbles. To understand this better, we need to examine the distribution of star formation.

2.3.3 Star Formation

Figure 2.4 summarizes the star formation history of each galaxy. To ensure a fair comparison between the galaxies we restrict this analysis to gas outside of the central 2 kpc, which minimizes the differences arising from the large difference in gas depletion in the center of the galaxies in different cases. The Hydro and MHD Weak galaxy undergo starbursts that have SFRs reaching up to 20 $M_\odot$ yr^{-1}. After the initial burst, the hydro

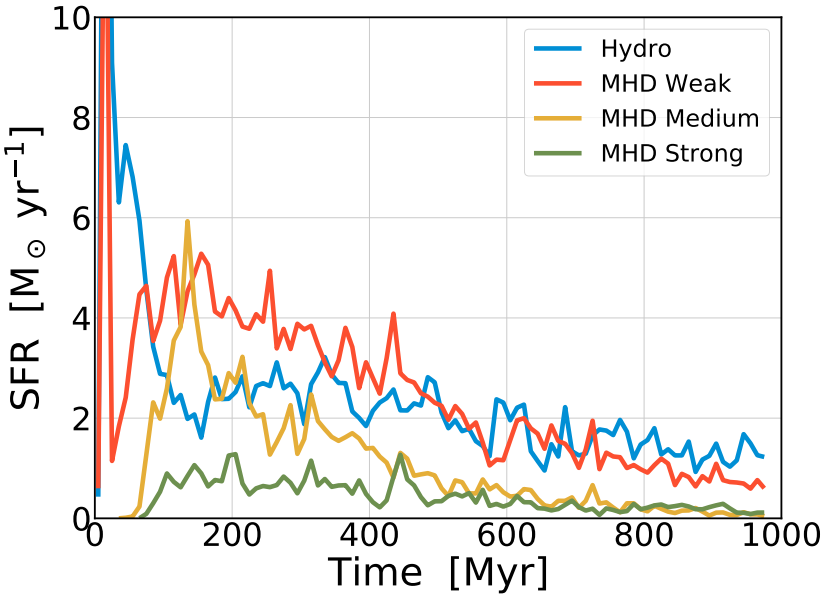

FIGURE 2.4: Star formation rate vs. time for each galaxy, excluding the central 2 kpc. Star formation rate is calculated by summing the mass of all stars formed within each time bin and dividing by the size of the bin. For the MHD Weak and Medium galaxies, field strengths decline over time due to increasing field strengths.

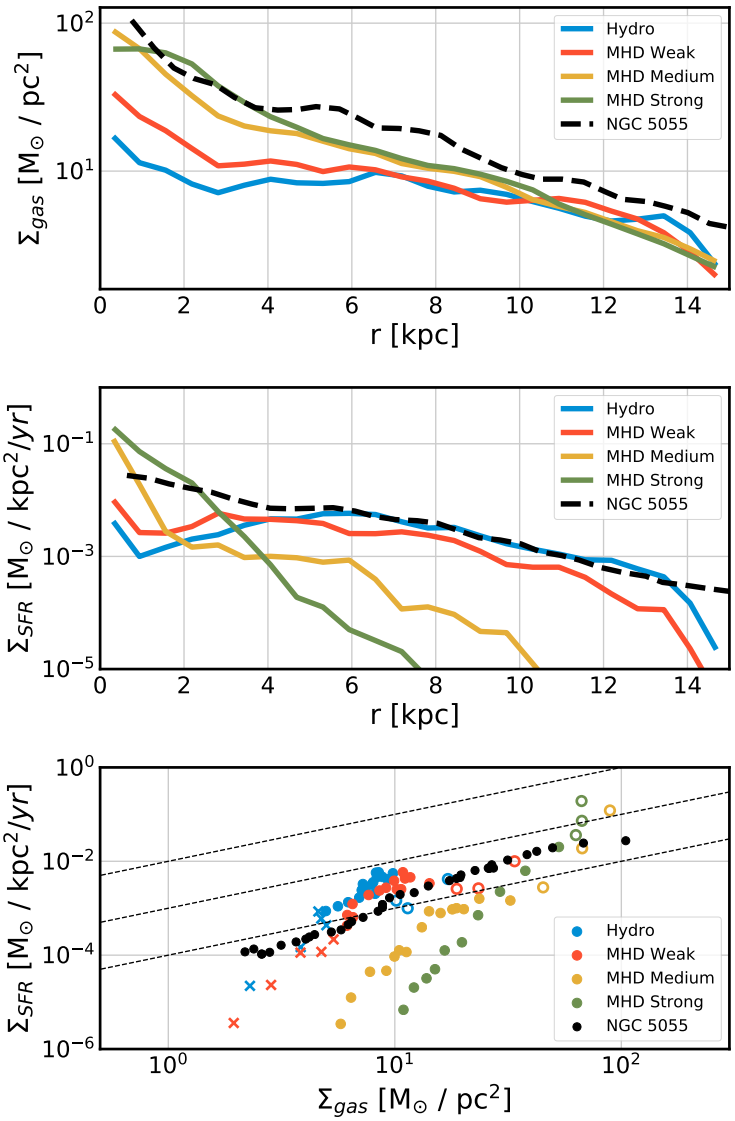

FIGURE 2.5: Top row: gas surface density as a function of galactocentric radius at 1 Gyr. Middle row: star formation rate surface density as a function of radius. Bottom row: star formation rate surface density vs. gas surface density, otherwise known as the Kennicutt-Schmidt relation. Open circles indicate points within 2 kpc of the center, and x's indicate points beyond 12 kpc. Diagonal lines indicate constant gas depletion times of 10^8, 10^9, and 10^{10} years, as done in (Bigiel et al.; 2008). Data for NGC 5055 is from Leroy et al. (2008).

galaxy settles into a constant SFR of $\sim 2 M_{\odot} yr^{-1}$ that reduces slightly by the end due to a decreasing gas content. The MHD Weak galaxy has an an initially elevated SFR of 5 $M_{\odot}$ yr^{-1}, which continually decreases and reaches 1 $M_{\odot}$ yr^{-1} by the end of the run, lower than the hydro galaxy. The MHD Medium does initially undergo a slight starburst, but it is delayed until ∼75 Myr and much smaller. Once it does begin to form stars it quickly reaches a SFR of 4 $M_{\odot}$ yr^{-1} before decreasing even more quickly than the MHD Weak galaxy, and ends up with a SFR of less than 1 $M_{\odot}$ yr^{-1}. The decreasing SFR in both the MHD Weak and Medium galaxies is due to the amplification of the magnetic fields, As they become stronger they become more dynamically important, they limit star formation more effectively. The MHD Strong galaxy has very limited star formation, remaining around 1 $M_{\odot}$ yr^{-1} or less for its entire evolution.

After 1 Gyr of evolution, the differences in the remaining gas content can be seen in the top row of figure 2.5, which plots the surface density versus galactocentric radius for each galaxy, alongside data from NGC 5055 (Leroy et al.; 2008). We note that all the simulated galaxies began with identical gas profiles, so the differences arise from the amount of gas consumed by star formation. The stronger the fields in the galaxy, the more gas remains due to the different star formation history. The differences are most prominent in the galactic center but exist out to around 10 kpc, beyond which all 4 galaxies have similar gas surface densities. The second row of figure 2.5 shows star formation surface density as a function of radius, averaged over the last 100 Myr of the simulation. The stronger field galaxies have enhanced star formation in the center 2 kpc due to having more gas remaining at this point in time, The MHD Strong galaxy is the most centrally concentrated due to the strong magnetic support in the outer disk (See figure 2.10). In the outer regions, star formation only occurs out to a limited distance. It is truncated at 14 kpc in the Hydro and MHD Weak cases, 10 kpc in the MHD Medium case, and at 8 kpc in the MHD Strong case.

The final row in figure 2.5 combines the above data to make the well-known Kennicutt-Schmidt plot. The surface densities were measured at 1 kpc resolution, and then binned by radius. Star formation rate surface density is calculated using stars that formed within the last 100 Myr in each pixel to make a fair comparison to observational tracers of star formation rate. The dashed lines on the plot show lines of constant consumption times of 10^8, 10^9, and 10^{10} years from top to bottom. Bigiel et al. (2008) label these using efficiencies per 10^8 yr of 100%, 10% and 1%, respectively. Open circles indicate the central 2 kpc which is depleted in the Hydro and MHD Weak galaxies, and x's indicate regions beyond 12 kpc where the disk has not had enough time to evolve significantly.

We note the regions beyond 12 kpc have no star formation at all in the MHD Medium and Strong galaxies, hence they do not appear on the plot.

In the bottom row of figure 2.5, the Hydro and MHD Weak galaxies have most of their gas at surface densities of 1-10 $M_\odot/pc^2$. They approach a consumption time of 2×10^9 years at 10 $M_\odot/pc^2$ with a reduced star formation at lower surface densities. The MHD Medium and Strong galaxies push the turn down further right, meaning that star formation is drastically reduced at low surface densities, but have higher surface densities towards the center of the galaxies. The SFR surface densities in the Medium and Strong galaxies fall far below the observations, which suggests the initial fields are too strong and result in unrealistically low star formation due to the extra magnetic support. This result is reinforced when we explicitly examine gas support in the next section. One caveat is that the surface density profiles are different, making an exact comparison between the simulated and observed galaxies difficult, but the overall differences in star formation are highlighted on the Kennicutt-Schmidt plot.

2.3.4 Gas Properties and Distribution

The Hydro and MHD Weak galaxies end up with higher star formation rates than the other two galaxies despite having less gas content remaining at the end. Our star formation model depends on the amount of dense gas. Thus we expect to see less dense gas when there is reduced star formation. Figure 2.6 shows a histogram of the total gas mass vs. number density excluding the central 2 kpc at the final snapshot. We see progressively less star forming gas (above the number density of 100) in the stronger field cases as expected. The left side of the distribution is also more extended with the weaker fields. This is because of the stronger feedback and larger bubbles. The regular features separated by factors of 8 in the plot are a result of the refinement strategy of Ramses, with each dip corresponding to a different refinement level.

As individual superbubbles form due to supernova feedback, the magnetic fields lines are dragged by the gas in the explosions, draping themselves around the bubbles. Figure 2.7 shows a typical example of such an event. This particular bubble has stopped expanding and does not end up escaping out of the disk. These explosions are a major source of turbulence in the gas and play a major role in the evolution of both the galaxy and its magnetic fields. Magnetic tension causes magnetic fields to resist being bent, counteracting the expansion of the bubbles. Thus the field strength also affects the visual morphology by limiting the number and size of holes in the gas distribution as seen in figure 2.3 and figure 2.11. The sizes of the bubbles are also affected by the local surface

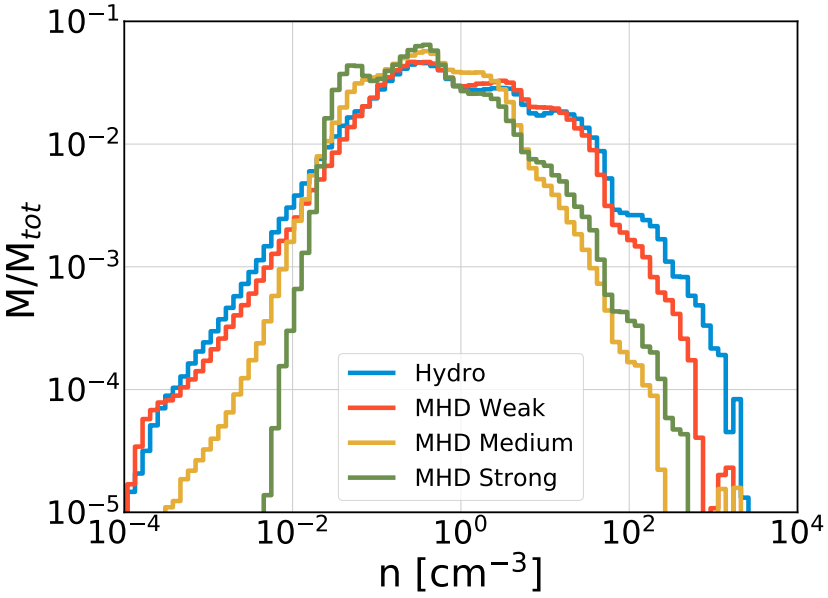

FIGURE 2.6: Histogram of gas number densities excluding central 2 kpc. Each bin represents the total mass at that density inside of a disk with radius 15 kpc, and 1 kpc high, normalized by the total gas mass of that disk. Magnetic fields limit the amount of star forming gas that is created by narrowing the distribution.

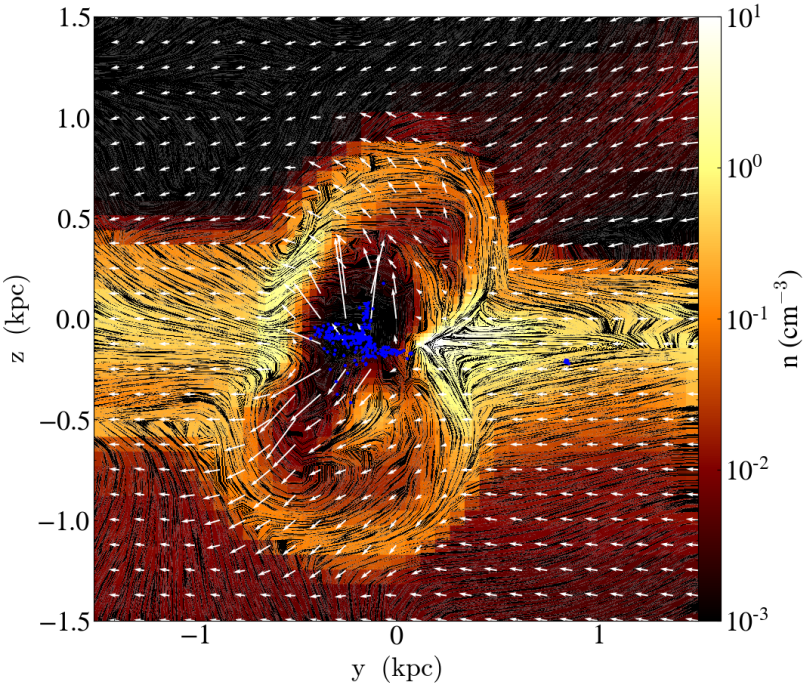

FIGURE 2.7: Example of a typical supernova bubble forming in the simulation. Color shows the number density of gas, with the magnetic field lines visualized by a line-integral convolution. Overplotted are the velocity of the gas (white), and newly formed star particles (blue). This particular bubble occurs at a radius of 7 kpc, at t=500 Myr in the MHD Medium galaxy. As the bubble expands, magnetic fields lines are dragged with the gas, and the magnetic tension resists expansion.

density. In the MHD Medium and Strong galaxies, star formation is limited to the central region where the high density surrounding medium will also limit the size of the bubbles. However the MHD Weak and Hydro galaxy show show different size bubbles despite having SFRs that are similarly distributed, demonstrating how magnetic fields limit bubble sizes.

The volume fractions of each temperature phase vary for each case, as shown in figure 2.8. We define the three phases as cold gas (T $<$ 5000 K), warm gas (5000 K $<$ T $<$ 50000 K), and hot gas (T $>$ 50000 K) and exclude the central 2 kpc, just as for the SFR plots. To first order, the volume fractions are explained by higher star formation rates leading to more supernovae and more hot gas in superbubbles. As the star formation rates decrease in the MHD Weak and Medium galaxies, the volume fraction of hot gas decreases correspondingly. In addition, cases with stronger magnetic fields have a lower hot volume fraction for a given star formation rate. Between 500 -700 Myr, the MHD Weak galaxy has roughly the same star formation rate as the Hydro galaxy, but a systematically lower hot volume fraction. Similarly, when the MHD Medium galaxy peaks in star formation around t=150 Myr, which is higher than the hydro galaxy, the hot volume fraction peaks at just over 20 percent. The MHD Strong galaxy has few, small bubbles. Its volume is almost entirely dominated by warm gas. The MHD Medium galaxy ends up in a similar state by the end of the simulation.

This strongly suggests that the magnetic fields are limiting the growth of superbubbles, as seen in figure 2.7. Another possible cause of the difference in bubble volume is the clustering of stars, if the star formation is more clustered, the supernovae combine more efficiently and will grow even larger (Nath and Shchekinov; 2013; Keller et al.; 2014). We have confirmed that the masses of the star clusters do not change between the four galaxies, all having similar distributions. It is commonly estimated that hot gas occupies $\sim$ 50 % of the ISM by volume (Tielens; 2010). Only the MHD Weak and Hydro cases reflect this. The MHD Medium and Strong filling factors in figure 2.8 extremely low at late times.

Figure 2.9 shows the mass weighted average of the height of the gas vs. radius. All of the galaxies have a value less than 100 pc in the center, increasing as the disk flares outwards. The thinnest disks occur in the MHD Weak and Hydro galaxies which both reach a height of 250 pc by a radius of 15 kpc. Of the two, the MHD Weak's disk is slightly thinner, because the small increase in the thickness from the magnetic support was countered by the reduced turbulence as a result of the lower SFR. The MHD Medium and Strong galaxies are both systematically thicker despite their drastically reduced star

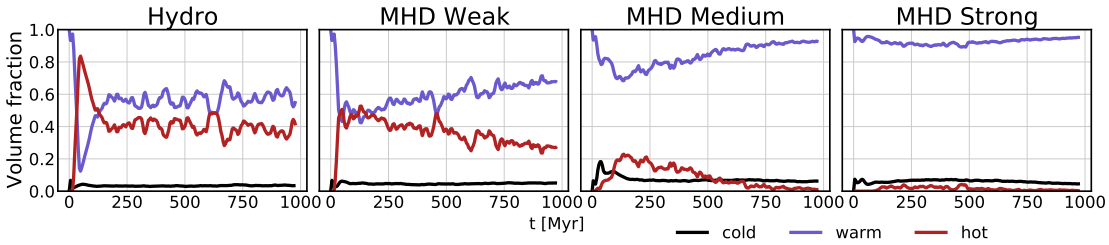

FIGURE 2.8: Volume fraction of each phase of gas in the ISM over time. Volume is calculated in a disk within a radius of 2-15 kpc, and height of 1 kpc
. Majority of the volume is split between the warm and hot phase gas. With increasing field strength the volume fraction of the warm phase gas increases, and hot phase gas decreases.

formation rates. The MHD Strong galaxy is the thickest, reaching a height of 400 pc. Because of the mass weighting this measure of thickness is mostly set by the high density gas, but in the galaxies with stronger fields there is less cold gas so the increased height is largely due to warm diffuse gas which is magnetically supported. To quantify these results, we next examine the different contributions to the supporting pressure.

The differences in gas properties and star formation rate ultimately arise due to the different forces (or pressures) acting on the gas, including thermal pressure, magnetic forces, turbulent motions and gravity (Benincasa et al.; 2016). Galaxies that have stronger magnetic fields have reduced turbulence due to the reduced stellar feedback.

Figure 2.10 shows mass-weighted pressures providing vertical support within 500 pc of the disk midplane versus radius, averaged over the final 100 Myr. The curves shows thermal pressure, $P_{\rm thermal} = n\,k\,T$, magnetic pressure $P_{\rm B} = B^2/8\pi$, and a turbulent pressure, estimated using $P_{\rm turb} = \rho v_z^2$, where v_z is the z-component of the velocity. The top row is cold gas, the middle row is warm gas, and the bottom row is hot gas, using the same definitions as above (i.e. in figure 2.8). In the cold gas, the MHD Weak, Medium, and Hydro galaxies have roughly the same total pressure, however with increasing magnetic field strength there is a smaller contribution from turbulence. The central regions of the MHD Medium and Strong galaxies have higher support to hold up the extra gas remaining there, and the radial extent of the cold phase is reduced. We draw attention to the difference between the Hydro and MHD Weak cases. The turbulent support is roughly half for MHD Weak case (with the difference being made up for by magnetic support), mirroring the halving of the star formation rate at this time relative to Hydro.

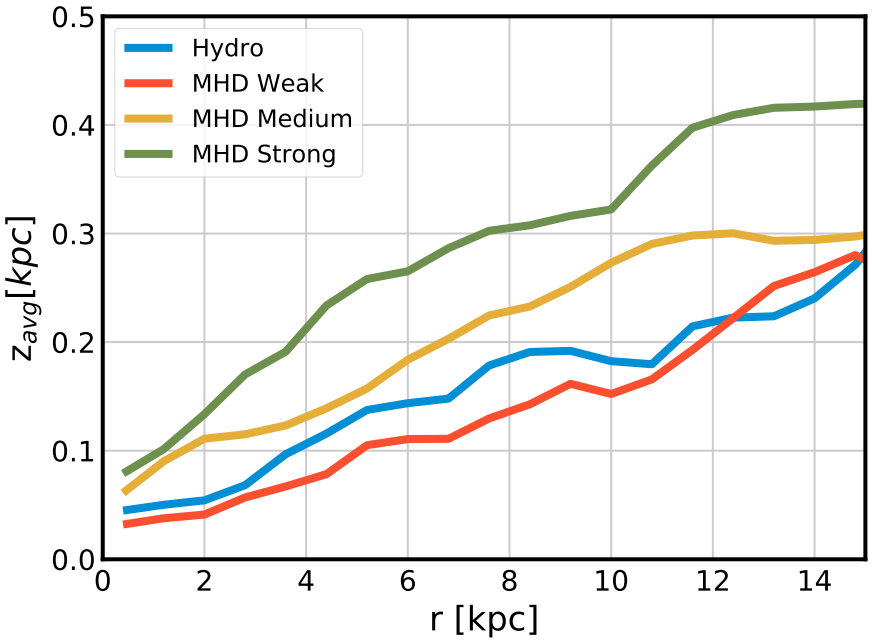

FIGURE 2.9: Mass weighted average |z| (which represents the thickness of the disk), as a function of galactocentric radius. In each radial bin, gas within 4 kpc vertically of the midplane was included. The MHD Weak galaxy has a thinner disk than the hydro case, but the more strongly magnetized galaxies are thicker.

In the warm gas, the difference in magnetic pressure is much larger between the MHD Weak and Medium. The increase in magnetic pressure in warm gas is largely responsible for the increased scale height in the Medium and Strong Galaxies. All pressures are in a rough equipartition in the MHD Weak galaxy, but the warm phase becomes dominated by magnetic pressure in the Medium and Strong galaxies.

The hot gas is localized in high pressure superbubbles which are dominated by thermal pressure in all galaxies. The magnetic fields expand with the hot gas, resulting in the lower magnetic pressure in the hot gas. There is also a high turbulent pressure, which is likely due to high-velocity flows as opposed to small scale turbulence.

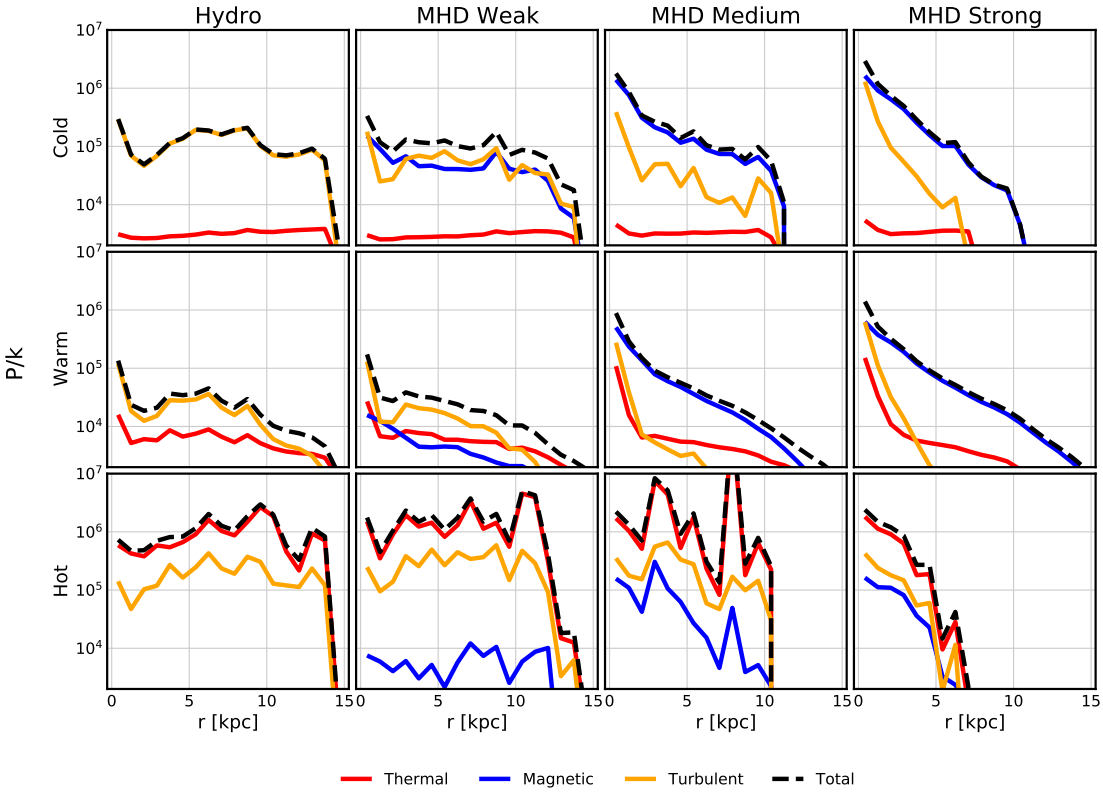

FIGURE 2.10: Comparison of different pressures in each galaxy. Included pressures are thermal (red), magnetic $B^2/8\pi$ (blue), and turbulent ρv_z^2 (yellow). Each pressure is calculated by taking a mass weighted average of gas within 1 kpc vertically in each radial bin. The pressures are calculated for three separate phases, using only the gas that falls within each temperature range: cold ($T < 5000$ K), warm (5000 K $< T <$ 50000 K), and hot ($T >$ 50000 K).

2.3.5 Disk stability

We have shown that the formation of a cold phase and subsequent star formation is much more limited in the stronger field cases. Gravitational instability drives the formation of the cold phase. We can quantify this using the Toomre Q parameter for the gas,

$$Q = \frac{\kappa\sqrt{c_s^2 + v_a^2 + \sigma_v^2}}{\pi G \Sigma}, \tag{2.4}$$

which accounts for the thermal, magnetic and turbulent support discussed in the previous section. Here c_s is sound speed, v_a is the Alfvén velocity, σ_v is the velocity dispersion of the gas, and Σ is the surface density of the gas. The literature contains several extended versions of the Toomre Q parameter (Romeo and Falstad; 2013; Körtgen et al.; 2019; Nipoti; 2023), which include adjustments for the 3D structure of the disk and multiple components like the stellar disk. We note that the AGORA stellar disk has quite a high velocity dispersion and thus the stellar component is quite stable and does not contribute much to the effective Q locally. The regions of low gas Q closely match up with the locations where stars form, confirming that this choice of Q is a reasonable approximation. Figure 2.11 shows the Toomre Q parameter for each galaxy at 1 Gyr, along with each of the individual support terms. The Alfvén velocity and sound speed were calculated by taking a mass weighted average of gas within 250 pc of the midplane, and the velocity dispersion in the midplane is estimated by summing over the differences between neighbouring cells.

The hydro galaxy again has highest turbulent support which is localized around star forming regions. Conversely, velocity dispersion provides the least support in the magnetic galaxies. Those same regions also contain high temperature gas which yields high sound speeds. The prevalence of hot bubbles drops rapidly as the field strength increase from left to right in the third row of the figure. The thermal support is lowest in dense gas seen along spiral arms, where the magnetic support is highest.

The fourth row of figure 2.11 shows the Toomre Q parameter, with red regions indicating Q$<$ 1. Much of the material with lower Q values has already collapsed so these values below 1 are not informative. Each galaxy is unstable only in regions of high surface density along spiral arms. The galaxies with stronger magnetic fields have dramatically fewer regions that are unstable and at large radii become totally stable against collapse, explaining the locations of star formation in the fifth row. Our MHD Weak galaxy has similarly placed but smoother unstable regions when compared to the hydro galaxy. This is directly related to the addition of magnetic support shown in the top

panel. The spiral features are thus smoother and more continuous, which is a general feature in the magnetized cases.

As discussed in Körtgen et al. (2019), magnetized galaxies may also be able to fragment via the Parker instability rather than gravitational instability, potentially allowing collapse in regions where $Q > 1$. This would be difficult to observe in our galaxies because stellar feedback is constantly stirring the gas and may disrupt the wavelike structure required. However, we see relatively little star formation outside of Toomre unstable regions. In addition, the timescale for these large-scale Parker instabilities tends to be long compared to turbulent crossing times.

In the outer regions of the disks, much of the gas is marginally stable ($1 \leq Q \leq 2$). In this regime, the development of spirals is still possible due to swing amplification (Binney and Tremaine; 2008). These spirals form but do not necessarily fragment into clouds. In the MHD strong case no dense structure forms in the outer regions (see figure 2.3) due to the enhanced magnetic support, and the star formation is heavily centrally concentrated, as shown in the bottom row.

2.4 Discussion

We simulated four galaxies with varying magnetic field strengths in order to understand the impact on their ISM and star formation regulation. We saw clear differences between the galaxies in their star formation rates. This result arises due to the consumption of gas fuel and the growth of the magnetic fields strength over time. Star formation rates can be understood via the gas support in each case. This is clearly reflected in the stability of the gas. Stronger fields are able to support the gas without feedback, particularly at large radii. Weak or absent fields must rely on turbulent support associated with star formation. Every case is internally self-consistent. However, the combination of the star formation rates, field strengths and gas morphology heavily favour the steady state generated by the MHD Weak case as the best match to observed disk galaxies.

A lack of star formation also means a lack of cold, dense gas precursors for star formation, which is reflected in the ISM gas phase results. This is tied to the Schmidt-law star formation model, that always forms stars at a fixed efficiency per free-fall time once gas is above a density threshold. While this is a standard model choice, it is important to recognize that the actual efficiency of star formation in dense gas is the subject of vigorous theoretical and observational study. In particular, the presence of

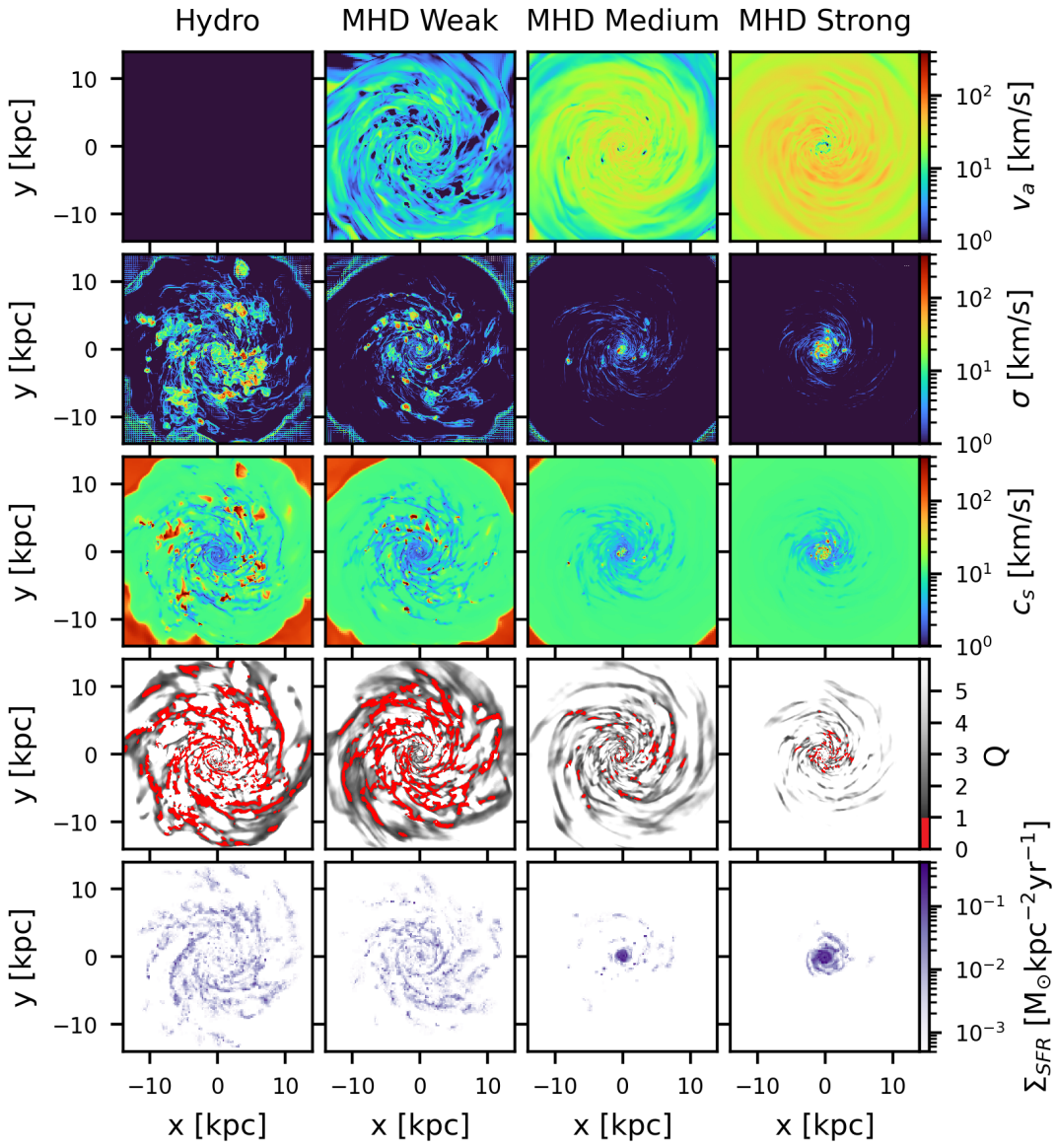

FIGURE 2.11: Toomre Q parameter and the three support terms included in it as shown in Equation 2.4. Top row: Alfvén velocity. Second row, velocity dispersion. Third row: sound speed. Fourth row: Toomre Q parameter. Red regions show Q<1, which are unstable to collapse. Q values of 1-2 are unstable to forming spirals. Fifth row: Surface density of star formation using stars formed within the last 100 Myr.

unresolved magnetic fields and turbulence could affect this efficiency in real galaxies, whereas the efficiency is fixed here (Federrath; 2015).

It is difficult to compare simulated field strengths to observed values. We argue that volume weighted fields are similar to observed synchrotron estimates. In particular, the MHD Weak case creates a flat radial profile. While this is compelling relative to the other cases, mock observations would provide more detailed insights (Ponnada et al.; 2022, 2023; Martin-Alvarez et al.; 2024).

The MHD Weak galaxy produced a steep power law increase in field strength at high densities. This is reminiscent of the upper envelope of the Zeeman observations (Crutcher et al.; 2010). However, our ideal-MHD simulated field strengths should be upper limits, as turbulent ambipolar diffusion will reduce the field at high densities (Heitsch et al.; 2004). Our simulations also show no evidence for the commonly inferred constant field strength in lower density gas. The lack of constant field has been observed by several independent simulation groups (Körtgen et al.; 2019; Rieder and Teyssier; 2017b; Ponnada et al.; 2022). Thus there is a tension between observations and theory on this point.

It is tempting to ask which of the four galaxies are the most realistic. Magnetic fields certainly exist in galaxies, ruling out the hydro galaxy. Similarly, the MHD Strong galaxy had initial fields above what we infer from observational constraints. Both it and the MHD medium case failed to match most observed properties for the field itself, gas morphologies and star formation.

The MHD Weak case did well on all these measures. We expect that any case starting with a sufficiently high plasma beta (> 100) would evolve to a saturated state similar to the MHD Weak case. The main difference would be the time it takes to do so. The key requirement is that the fields are allowed to amplify naturally to the point of saturation.

We note that the MHD Weak galaxy achieves similar star formation rates and gas distributions to the Hydro galaxy at intermediate times. Eventually, the gas support includes a magnetic component similar to the turbulence and the star formation rate dips below the hydro case. In future work, we will explore the morphology of the field and how it is linked to its ability to support the gas in place of stellar feedback. This may be related to the split between turbulent and mean fields. It would also be worth testing different morphologies in the initial condition. We started with a purely toroidal field which could possibly bias the final field configuration.

This work adds to the growing list of MHD galaxy simulations. (Wang and Abel; 2009; Pakmor and Springel; 2013; Martin-Alvarez et al.; 2020; Wibking and Krumholz; 2023). Similar to other simulations of isolated disks, there is initially fast magnetic field amplification due to an central starburst, followed by a self-regulated amplification phase as the fields approach saturation. The self-regulated phase is consistent with the feedback-driven amplification seen in late times in cosmological simulations, and produces similar field strengths (Martin-Alvarez et al.; 2018; Pakmor et al.; 2020). Several isolated galaxy studies have also demonstrated that supernovae play a major role in field amplification, which our results are consistent with (Butsky et al.; 2017; Rieder and Teyssier; 2016). It has also been found that magnetic fields reach equipartition with thermal energy once saturated (Pakmor et al.; 2014). Our results show that happens specifically in warm-phase gas, while in cold gas the fields are above equipartition, and in hot gas they are below equipartition. Our findings that most of the amplification occurring in the warm phase has also been seen in simulations by Martin-Alvarez et al. (2022).

This work does not account for cosmic rays, which could contribute significantly to gas support in principle (e.g. Semenov et al.; 2021). We note that there is a lot of uncertainty regarding cosmic rays coupling to the gas and how best to model them numerically. While the current work uses simple approaches to isolate key effects, cosmic rays would be an interesting future direction.

We also do not account for non-ideal MHD effects. While ideal MHD is a good approximation for most of the ISM, effects such as ambipolar diffusion may become important in high density star forming regions. We anticipate that these effects are comparable to the impact of the magnetic field on small star formation generally, which is not addressed in our simple star formation prescription. We also avoided more elaborate feedback models. Complex feedback models would also be affected by unresolved turbulence and magnetic fields. Though we chose simple feedback by design to keep interpretation simple, it is worth keeping in mind that factors like star formation efficiency could be different in different cases (e.g. with stronger magnetic fields).

Studying the properties of star forming regions and molecular cloud analogues is a natural extension of this work to smaller scales. Magnetic fields may affect the shapes and sizes of star forming clouds, which could also affect small-scale star formation. To do this, we need higher resolution simulations. We have performed zoom-in simulations, beginning with the galactic setup in this work, seeking to characterize the affect of galactic-scale dynamics on star forming regions (Zhao et al 2023, in prep).

Another population of interest within galaxies is that of superbubbles. JWST observations have made it possible to perform a detailed census of superbubbles in nearby galaxies (Watkins et al.; 2023). Our results show that magnetic fields dramatically affect the evolution of superbubbles. It would be interesting to characterize their populations in these and higher resolution simulations as a further constraint on how well the simulated magnetic fields match those in real galaxies.

2.5 Conclusions

We have performed simulations of magnetized Milky-Way like galaxies with different magnetic field strengths. As the galaxies evolved differences in gas distributions and star formation occur due to the differing levels of magnetic support which in turn result in different levels of turbulent support from the stellar feedback. We summarize our conclusions as follows:

- We have demonstrated that evolving a simulated galaxy towards a realistic self-regulating ISM with magnetic fields is achievable with an initially weak toroidal field and simple models for star formation and feedback. Conversely, starting with field strengths typical for the ISM limits star formation though magnetic support.
- Stronger magnetic fields generally reduce a galaxy's star formation. As magnetic fields amplify over time and their strengths increase, star formation rates will decrease. Field strengths evolve due to the star formation and feedback and provide an additional form of self-regulation in galaxies.
- In our isolated galaxies, dynamo amplification mainly occurs in the warm diffuse medium of the ISM, from number densities of 0.1 to 10 cm^{-3}. The galactic magnetic fields first saturate at high densities but continue to grow at intermediate densities over longer timescales.
- Starting with high initial fields may lock the galaxy into field configurations set by the initial conditions that result in unrealistically low star formation. Stronger magnetic fields generally result in reduced turbulence. This is due to both the reduced supernovae feedback, but also from magnetic fields limiting superbubble growth. Smaller feedback bubbles can be seen in the projected gas density and by the reduced volume fraction of hot gas for a given star formation rate.
- Magnetic fields change the distribution of unstable regions in the disk, which are well characterized with a modified gas Toomre Q. Strongly magnetized galaxies

become completely stable in the outer disk and star formation becomes more centrally concentrated.

- Initially weak magnetic fields evolve to play an important role in the vertical pressure support in galaxies, approaching equipartition levels with turbulence in the cold phase and with both thermal pressure and turbulence in the warm phase. This adds an extra component the established pressure regulation picture (Ostriker et al.; 2010; Benincasa et al.; 2016).

- Initially weak fields saturate at $\sim 1\ \mu G$ (volume weighted) in the warm medium at a range of radii, while still producing a steady-state, self-regulated galaxy. While the flat B profile is consistent with synchrotron observations, the $\sim 1\ \mu G$ amplitude is low. The amplitudes inferred from observations rely on several assumptions. Thus it may also be worth exploring if the observed amplitudes are overestimates.

- The evolved, self-regulated state of the MHD Weak simulation best matches the expected star formation radial profile, taken from either the Kennicutt-Schmidt relation or the nearby galaxy NGC 5055, which the AGORA initial condition is similar to. This provides further support for the idea that lower ($\sim 1\ \mu G$) magnetic fields at typical ISM densities (0.1-1 cm^{-3}) are consistent with realistic galaxies.

Acknowledgements

The authors would like to thank Ralph Pudritz for many useful dicussions. HR is supported by an NSERC postgraduate scholarship, and JW is supported by Discovery Grants from NSERC of Canada. Computational resources for this project were enabled by a grant to JW from Compute Canada/Digital Alliance Canada and carried out on the Niagara Supercomputer.

Data Availability

The data used this article will be shared upon reasonable request to the corresponding author.

Bibliography

Agertz, O. and Kravtsov, A. V. (2015). On the Interplay between Star Formation and Feedback in Galaxy Formation Simulations, **804**(1): 18.

Agertz, O., Teyssier, R. and Moore, B. (2011). The formation of disc galaxies in a ΛCDM universe, **410**(2): 1391–1408.

Basu, A. and Roy, S. (2013). Magnetic fields in nearby normal galaxies: energy equipartition, **433**(2): 1675–1686.

Beck, R., Chamandy, L., Elson, E. and Blackman, E. G. (2019). Synthesizing Observations and Theory to Understand Galactic Magnetic Fields: Progress and Challenges, *Galaxies* **8**(1): 4.

Beck, R. and Wielebinski, R. (2013). Magnetic Fields in Galaxies, *in* T. D. Oswalt and G. Gilmore (eds), *Planets, Stars and Stellar Systems. Volume 5: Galactic Structure and Stellar Populations*, Vol. 5, p. 641.

Benincasa, S. M., Wadsley, J., Couchman, H. M. P. and Keller, B. W. (2016). The anatomy of a star-forming galaxy: pressure-driven regulation of star formation in simulated galaxies, **462**(3): 3053–3068.

Benincasa, S. M., Wadsley, J. W., Couchman, H. M. P., Pettitt, A. R., Keller, B. W., Woods, R. M. and Grond, J. J. (2020). The anatomy of a star-forming galaxy II: FUV heating via dust, **499**(2): 2028–2041.

Bigiel, F., Leroy, A., Walter, F., Brinks, E., de Blok, W. J. G., Madore, B. and Thornley, M. D. (2008). The Star Formation Law in Nearby Galaxies on Sub-Kpc Scales, **136**(6): 2846–2871.

Binney, J. and Tremaine, S. (2008). *Galactic Dynamics: Second Edition*.

Brandenburg, A. and Subramanian, K. (2005). Astrophysical magnetic fields and nonlinear dynamo theory, **417**(1-4): 1–209.

Burkhart, B. (2018). The Star Formation Rate in the Gravoturbulent Interstellar Medium, **863**(2): 118.

Butsky, I., Zrake, J., Kim, J.-h., Yang, H.-I. and Abel, T. (2017). Ab Initio Simulations of a Supernova-driven Galactic Dynamo in an Isolated Disk Galaxy, **843**(2): 113.

Cao, Z. and Li, H.-b. (2023). Turbulence in Zeeman Measurements from Molecular Clouds, **946**(2): L46.

Chyży, K. T. and Buta, R. J. (2008). Discovery of a Strong Spiral Magnetic Field Crossing the Inner Pseudoring of NGC 4736, **677**(1): L17.

Crutcher, R. M., Wandelt, B., Heiles, C., Falgarone, E. and Troland, T. H. (2010). Magnetic Fields in Interstellar Clouds from Zeeman Observations: Inference of Total Field Strengths by Bayesian Analysis, **725**(1): 466–479.

Evans, C. R. and Hawley, J. F. (1988). Simulation of Magnetohydrodynamic Flows: A Constrained Transport Model, **332**: 659.

Federrath, C. (2015). Inefficient star formation through turbulence, magnetic fields and feedback, **450**(4): 4035–4042.

Federrath, C., Chabrier, G., Schober, J., Banerjee, R., Klessen, R. S. and Schleicher, D. R. G. (2011). Mach Number Dependence of Turbulent Magnetic Field Amplification: Solenoidal versus Compressive Flows, **107**(11): 114504.

Federrath, C. and Klessen, R. S. (2012). The Star Formation Rate of Turbulent Magnetized Clouds: Comparing Theory, Simulations, and Observations, **761**(2): 156.

Ferland, G. J., Chatzikos, M., Guzmán, F., Lykins, M. L., van Hoof, P. A. M., Williams, R. J. R., Abel, N. P., Badnell, N. R., Keenan, F. P., Porter, R. L. and Stancil, P. C. (2017). The 2017 Release Cloudy, **53**: 385–438.

Fletcher, A., Beck, R., Shukurov, A., Berkhuijsen, E. M. and Horellou, C. (2011). Magnetic fields and spiral arms in the galaxy M51, **412**(4): 2396–2416.

Geach, J. E., Lopez-Rodriguez, E., Doherty, M. J., Chen, J., Ivison, R. J., Bendo, G. J., Dye, S. and Coppin, K. E. K. (2023). Polarized thermal emission from dust in a galaxy at redshift 2.6, *arXiv e-prints* p. arXiv:2309.02034.

Girichidis, P., Seifried, D., Naab, T., Peters, T., Walch, S., Wünsch, R., Glover, S. C. O. and Klessen, R. S. (2018). The SILCC project - V. The impact of magnetic fields on the chemistry and the formation of molecular clouds, **480**(3): 3511–3540.

Goldsmith, P. F., Heyer, M., Narayanan, G., Snell, R., Li, D. and Brunt, C. (2008). Large-Scale Structure of the Molecular Gas in Taurus Revealed by High Linear Dynamic Range Spectral Line Mapping, **680**(1): 428–445.

Grand, R. J. J., Gómez, F. A., Marinacci, F., Pakmor, R., Springel, V., Campbell, D. J. R., Frenk, C. S., Jenkins, A. and White, S. D. M. (2017). The Auriga Project: the properties and formation mechanisms of disc galaxies across cosmic time, **467**(1): 179–207.

Han, J. L. (2017). Observing Interstellar and Intergalactic Magnetic Fields, **55**(1): 111–157.

Heitsch, F., Zweibel, E. G., Slyz, A. D. and Devriendt, J. E. G. (2004). Turbulent Ambipolar Diffusion: Numerical Studies in Two Dimensions, **603**(1): 165–179.

Hix, R., He, C.-C. and Ricotti, M. (2023). Bimodal star formation in simulations of strongly magnetized giant molecular clouds, **522**(4): 6203–6216.

Hockney, R. W. and Eastwood, J. W. (1981). *Computer Simulation Using Particles*.

Hopkins, P. F., Wetzel, A., Kereš, D., Faucher-Giguère, C.-A., Quataert, E., Boylan-Kolchin, M., Murray, N., Hayward, C. C., Garrison-Kimmel, S., Hummels, C., Feldmann, R., Torrey, P., Ma, X., Anglés-Alcázar, D., Su, K.-Y., Orr, M., Schmitz, D., Escala, I., Sanderson, R., Grudić, M. Y., Hafen, Z., Kim, J.-H., Fitts, A., Bullock, J. S., Wheeler, C., Chan, T. K., Elbert, O. D. and Narayanan, D. (2018). FIRE-2 simulations: physics versus numerics in galaxy formation, **480**(1): 800–863.

Kainulainen, J., Beuther, H., Henning, T. and Plume, R. (2009). Probing the evolution of molecular cloud structure. From quiescence to birth, **508**(3): L35–L38.

Keller, B. W., Wadsley, J., Benincasa, S. M. and Couchman, H. M. P. (2014). A superbubble feedback model for galaxy simulations, **442**(4): 3013–3025.

Kim, C.-G., Kim, J.-G., Gong, M. and Ostriker, E. C. (2023). Introducing TIGRESS-NCR. I. Coregulation of the Multiphase Interstellar Medium and Star Formation Rates, **946**(1): 3.

Kim, J.-h., Agertz, O., Teyssier, R., Butler, M. J., Ceverino, D., Choi, J.-H., Feldmann, R., Keller, B. W., Lupi, A., Quinn, T., Revaz, Y., Wallace, S., Gnedin, N. Y., Leitner, S. N., Shen, S., Smith, B. D., Thompson, R., Turk, M. J., Abel, T., Arraki, K. S., Benincasa, S. M., Chakrabarti, S., DeGraf, C., Dekel, A., Goldbaum, N. J., Hopkins, P. F., Hummels, C. B., Klypin, A., Li, H., Madau, P., Mandelker, N., Mayer, L., Nagamine, K., Nickerson, S., O'Shea, B. W., Primack, J. R., Roca-Fàbrega, S., Semenov, V., Shimizu, I., Simpson, C. M., Todoroki, K., Wadsley, J. W., Wise, J. H. and AGORA Collaboration (2016). The AGORA High-resolution Galaxy Simulations Comparison Project. II. Isolated Disk Test, **833**(2): 202.

Körtgen, B., Banerjee, R., Pudritz, R. E. and Schmidt, W. (2019). Global dynamics of the interstellar medium in magnetized disc galaxies, **489**(4): 5004–5021.

Krumholz, M. R. and Federrath, C. (2019). The Role of Magnetic Fields in Setting the Star Formation Rate and the Initial Mass Function, *Frontiers in Astronomy and Space Sciences* **6**: 7.

Leroy, A. K., Walter, F., Brinks, E., Bigiel, F., de Blok, W. J. G., Madore, B. and Thornley, M. D. (2008). The Star Formation Efficiency in Nearby Galaxies: Measuring Where Gas Forms Stars Effectively, **136**(6): 2782–2845.

Lopez-Rodriguez, E., Borlaff, A. S., Beck, R., Reach, W. T., Mao, S. A., Ntormousi, E., Tassis, K., Martin-Alvarez, S., Clark, S. E., Dale, D. A. and del Moral-Castro, I. (2023). Extragalactic Magnetism with SOFIA (SALSA Legacy Program): The Magnetic Fields in the Multiphase Interstellar Medium of the Antennae Galaxies, **942**(1): L13.

Martin-Alvarez, S., Devriendt, J., Slyz, A., Sijacki, D., Richardson, M. L. A. and Katz, H. (2022). Towards convergence of turbulent dynamo amplification in cosmological simulations of galaxies, **513**(3): 3326–3344.

Martin-Alvarez, S., Devriendt, J., Slyz, A. and Teyssier, R. (2018). A three-phase amplification of the cosmic magnetic field in galaxies, **479**(3): 3343–3365.

Martin-Alvarez, S., Lopez-Rodriguez, E., Dacunha, T., Clark, S. E., Borlaff, A. S., Beck, R., Rodríguez Montero, F., Jung, S. L., Devriendt, J., Slyz, A., Roman-Duval, J. C., Ntormousi, E., Tahani, M., Subramanian, K., Dale, D. A., Marcum, P. M., Tassis, K., del Moral-Castro, I., Tram, L. N. and Jarvis, M. J. (2024). Extragalactic Magnetism with SOFIA (SALSA Legacy Program). VII. A Tomographic View of Far-infrared and Radio Polarimetric Observations through MHD Simulations of Galaxies, **966**(1): 43.

Martin-Alvarez, S., Slyz, A., Devriendt, J. and Gómez-Guijarro, C. (2020). How primordial magnetic fields shrink galaxies, **495**(4): 4475–4495.

Miyoshi, T. and Kusano, K. (2005). An MHD Simulation of the Magnetosphere Based on the HLLD Approximate Riemann Solver, *AGU Fall Meeting Abstracts*, Vol. 2005, pp. SM51B–1295.

Nath, B. B. and Shchekinov, Y. (2013). Conditions for Supernovae-driven Galactic Winds, **777**(1): L12.

Nipoti, C. (2023). Local gravitational instability of stratified rotating fluids: three-dimensional criteria for gaseous discs, **518**(4): 5154–5162.

Ostriker, E. C., McKee, C. F. and Leroy, A. K. (2010). Regulation of Star Formation Rates in Multiphase Galactic Disks: A Thermal/Dynamical Equilibrium Model, **721**(2): 975–994.

Padoan, P., Haugbølle, T. and Nordlund, Å. (2012). A Simple Law of Star Formation, **759**(2): L27.

Pakmor, R., Marinacci, F. and Springel, V. (2014). Magnetic Fields in Cosmological Simulations of Disk Galaxies, **783**(1): L20.

Pakmor, R. and Springel, V. (2013). Simulations of magnetic fields in isolated disc galaxies, **432**(1): 176–193.

Pakmor, R., van de Voort, F., Bieri, R., Gómez, F. A., Grand, R. J. J., Guillet, T., Marinacci, F., Pfrommer, C., Simpson, C. M. and Springel, V. (2020). Magnetizing the circumgalactic medium of disc galaxies, **498**(3): 3125–3137.

Pattle, K., Fissel, L., Tahani, M., Liu, T. and Ntormousi, E. (2023). Magnetic Fields in Star Formation: from Clouds to Cores, *in* S. Inutsuka, Y. Aikawa, T. Muto, K. Tomida and M. Tamura (eds), *Protostars and Planets VII*, Vol. 534 of *Astronomical Society of the Pacific Conference Series*, p. 193.

Planck Collaboration (2016). Planck intermediate results. XXXV. Probing the role of the magnetic field in the formation of structure in molecular clouds, **586**: A138.

Ponnada, S. B., Panopoulou, G. V., Butsky, I. S., Hopkins, P. F., Loebman, S. R., Hummels, C., Ji, S., Wetzel, A., Faucher-Giguère, C.-A. and Hayward, C. C. (2022). Magnetic fields on FIRE: Comparing B-fields in the multiphase ISM and CGM of simulated L_* galaxies to observations, **516**(3): 4417–4431.

Ponnada, S. B., Panopoulou, G. V., Butsky, I. S., Hopkins, P. F., Skalidis, R., Hummels, C., Quataert, E., Kereš, D., Faucher-Giguère, C.-A. and Su, K.-Y. (2023). Synchrotron Emission on FIRE: Equipartition Estimators of Magnetic Fields in Simulated Galaxies with Spectrally-Resolved Cosmic Rays, *arXiv e-prints* p. arXiv:2309.04526.

Rieder, M. and Teyssier, R. (2016). A small-scale dynamo in feedback-dominated galaxies as the origin of cosmic magnetic fields - I. The kinematic phase, **457**(2): 1722–1738.

Rieder, M. and Teyssier, R. (2017a). A small-scale dynamo in feedback-dominated galaxies - II. The saturation phase and the final magnetic configuration, **471**(3): 2674–2686.

Rieder, M. and Teyssier, R. (2017b). A small-scale dynamo in feedback-dominated galaxies - III. Cosmological simulations, **472**(4): 4368–4373.

Riols, A. and Latter, H. (2019). Gravitoturbulent dynamos in astrophysical discs, **482**(3): 3989–4008.

Robinson, H. (2021). Realistic Galaxy Simulations: Feedback, Magnetic Fields and the ISM, *M.Sc Thesis, McMaster University, http://hdl.handle.net/11375/26150* .

Romeo, A. B. and Falstad, N. (2013). A simple and accurate approximation for the Q stability parameter in multicomponent and realistically thick discs, **433**(2): 1389–1397.

Semenov, V. A., Kravtsov, A. V. and Caprioli, D. (2021). Cosmic-Ray Diffusion Suppression in Star-forming Regions Inhibits Clump Formation in Gas-rich Galaxies, **910**(2): 126.

Semenov, V. A., Kravtsov, A. V. and Gnedin, N. Y. (2018). How Galaxies Form Stars: The Connection between Local and Global Star Formation in Galaxy Simulations, **861**(1): 4.

Smith, B. D., Bryan, G. L., Glover, S. C. O., Goldbaum, N. J., Turk, M. J., Regan, J., Wise, J. H., Schive, H.-Y., Abel, T., Emerick, A., O'Shea, B. W., Anninos, P., Hummels, C. B. and Khochfar, S. (2017). GRACKLE: a chemistry and cooling library for astrophysics, **466**(2): 2217–2234.

Steinwandel, U. P., Beck, M. C., Arth, A., Dolag, K., Moster, B. P. and Nielaba, P. (2019). Magnetic buoyancy in simulated galactic discs with a realistic circumgalactic medium, **483**(1): 1008–1028.

Steinwandel, U. P., Böss, L. M., Dolag, K. and Lesch, H. (2022). On the Small-scale Turbulent Dynamo in the Intracluster Medium: A Comparison to Dynamo Theory, **933**(2): 131.

Steinwandel, U. P., Dolag, K., Lesch, H., Moster, B. P., Burkert, A. and Prieto, A. (2020). On the origin of magnetic driven winds and the structure of the galactic dynamo in isolated galaxies, **494**(3): 4393–4412.

Su, K.-Y., Hayward, C. C., Hopkins, P. F., Quataert, E., Faucher-Giguère, C.-A. and Kereš, D. (2018). Stellar feedback strongly alters the amplification and morphology of galactic magnetic fields, **473**(1): L111–L115.

Sugitani, K., Nakamura, F., Watanabe, M., Tamura, M., Nishiyama, S., Nagayama, T., Kandori, R., Nagata, T., Sato, S., Gutermuth, R. A., Wilson, G. W. and Kawabe, R. (2011). Near-infrared-imaging Polarimetry Toward Serpens South: Revealing the Importance of the Magnetic Field, **734**(1): 63.

Teyssier, R. (2002). Cosmological hydrodynamics with adaptive mesh refinement. A new high resolution code called RAMSES, **385**: 337–364.

Tielens, A. G. G. M. (2010). *The Physics and Chemistry of the Interstellar Medium*.

Wang, P. and Abel, T. (2009). Magnetohydrodynamic Simulations of Disk Galaxy Formation: The Magnetization of the Cold and Warm Medium, **696**(1): 96–109.

Watkins, E. J., Barnes, A. T., Henny, K., Kim, H., Kreckel, K., Meidt, S. E., Klessen, R. S., Glover, S. C. O., Williams, T. G., Keller, B. W., Leroy, A. K., Rosolowsky, E., Lee, J. C., Anand, G. S., Belfiore, F., Bigiel, F., Blanc, G. A., Boquien, M., Cao, Y., Chandar, R., Chen, N. M., Chevance, M., Congiu, E., Dale, D. A., Deger, S., Egorov, O. V., Emsellem, E., Faesi, C. M., Grasha, K., Groves, B., Hassani, H., Henshaw, J. D., Herrera, C., Hughes, A., Jeffreson, S., Jiménez-Donaire, M. J., Koch, E. W., Kruijssen, J. M. D., Larson, K. L., Liu, D., Lopez, L. A., Pessa, I., Pety, J., Querejeta, M., Saito, T., Sandstrom, K., Scheuermann, F., Schinnerer, E., Sormani, M. C., Stuber, S. K., Thilker, D. A., Usero, A. and Whitmore, B. C. (2023). PHANGS-JWST First Results: A Statistical View on Bubble Evolution in NGC 628, **944**(2): L24.

Wibking, B. D. and Krumholz, M. R. (2023). The global structure of magnetic fields and gas in simulated Milky Way-analogue galaxies, **521**(4): 5972–5990.

Wissing, R. and Shen, S. (2023). Numerical dependencies of the galactic dynamo in isolated galaxies with SPH, **673**: A47.

Wolfire, M. G., McKee, C. F., Hollenbach, D. and Tielens, A. G. G. M. (2003). Neutral Atomic Phases of the Interstellar Medium in the Galaxy, **587**(1): 278–311.

Zweibel, E. G. (2017). The basis for cosmic ray feedback: Written on the wind, *Physics of Plasmas* **24**(5): 055402.

Chapter 3

Star Formation and Magnetic Field Amplification due to Galactic Spirals

The content of this chapter is a second revision of the manuscript text for publication under the following citation:

Robinson, H. (2025). Star Formation and Magnetic Field Amplification due to Galactic Spirals. The Astrophysical Journal, 989(2), 205.

Star Formation and Magnetic Field Amplification due to Galactic Spirals

Hector Robinson
Department of Physics and Astronomy
McMaster University, Hamilton, ON, Canada
Email: robinh4@mcmaster.ca

James Wadsley
Department of Physics and Astronomy
McMaster University
Email: wadsley@mcmaster.ca

Ralph Pudritz
Department of Physics and Astronomy
McMaster University
Email: pudritz@mcmaster.ca

Jerry Sellwood
Steward Observatory
University of Arizona
Email: sellwood@arizona.edu

Abstract

We use global MHD galaxy simulations to investigate the effects of spiral arms on the evolution of magnetic fields and star formation within a self-regulated interstellar medium (ISM). The same galaxy is simulated twice: once with self-consistent stellar spiral arms and once more with the stellar spirals suppressed via a novel numerical approach, using the Ramses AMR code. Spiral arms continually promote star formation, with 2.6 times higher rates in the spiral galaxy. The higher rate is due to high gas columns gathered along the spiral arms, rather than increasing the star formation efficiency at a given gas

column. In both cases, the magnetic field is initially amplified via a small-scale dynamo driven by turbulence due to supernova feedback. Only the spiral galaxy exhibits late-time, consistent field growth due to a large-scale dynamo (e-folding time $\sim$ 600 Myr). This results in volume-averaged field strengths of ~ 1 μG after 1 Gyr of evolution. The mean-fields tend to align themselves with the spiral arms and are coherent up to 10 kpc scales. We demonstrate a novel large-scale dynamo mechanism, whereby spiral-driven radial flows enable the mean-field amplification.

Keywords: *Methods: numerical – MHD – ISM: magnetic fields – Galaxies: star formation*

3.1 Introduction

Spirals drive many aspects of evolution within disk galaxies. They cause radial migration of stars and gas (Sellwood and Binney; 2002; Daniel and Wyse; 2018), flatten rotation curves (Lovelace and Hohlfeld; 1978; Berrier and Sellwood; 2015), promote star formation (Elmegreen and Elmegreen; 1986; Kim et al.; 2020), and drive turbulence throughout the ISM (Kim et al.; 2006). Amplification of a galaxy's magnetic field is also closely related to its star formation, turbulence, and rotation. Thus, it seems likely that spiral arms assist the growth of magnetic fields through these effects.

Observations of magnetic fields in spiral galaxies have begun to constrain the field strengths and orientations. Synchrotron emission suggests fields $\sim$10 μG, that may be stronger in high density regions (Fletcher et al.; 2011; Basu and Roy; 2013; Beck and Wielebinski; 2013). Polarization measurements have shown that the fields tend to be organized into large-scale spirals, regardless of the presence of optical spirals (Chyży and Buta; 2008; Beck et al.; 2019; Lopez-Rodriguez et al.; 2023). Other authors find that magnetic fields are generally aligned with, or slightly inclined to, gas structures down to 100 pc scales (Goldsmith et al.; 2008; Frick et al.; 2016; Planck Collaboration; 2016; Su et al.; 2018; Beck et al.; 2020; Zhao, Zhou, Baan, Hu, Lazarian, Tang, Esimbek, He, Li, Ji, Chang and Tursun; 2024).

In order to have reached detectable levels, magnetic fields in galaxies need to have been amplified through some dynamo process (Geach et al.; 2023; Ledos et al.; 2024). Dynamos are typically classified into two main categories: small-scale and large-scale. Small-scale, or turbulent, dynamos amplify field strengths exponentially through the random stretching, twisting and folding of field lines in a turbulent medium and tend to allow fast growth on smaller scales only. This process operates on short ($<$ 10 Myr)

timescales but leaves the field disordered as viewed on larger scales. Many simulations have demonstrated that a turbulent dynamo can generate field strengths approaching those observed in nature (Federrath et al.; 2011; Bhat et al.; 2016; Rieder and Teyssier; 2016; Pakmor et al.; 2020; Martin-Alvarez et al.; 2022).

Large-scale or mean-field dynamos are required to create fields that are coherent over galactic scales. In principle, this could be due to driving a turbulent dynamo on the circumgalactic medium (galactic halo) scale (Rieder and Teyssier; 2017; Pudritz and Silk; 1989). The classical large scale dynamo is assumed to work through an interplay between galactic rotation and the buoyancy of the fields (Parker; 1955), a process that is predicted to operate on Gyr timescales. Mean-field dynamos for galaxies are commonly of the $\alpha-\Omega$ type (Brandenburg and Subramanian; 2005). The $\alpha-\Omega$ dynamo is predicted to produce quadrupolar fields in the galactic halo, magnetic spirals, and helical turbulence (Stix; 1975; Henriksen; 2017; Shukurov et al.; 2019), some of which were observed in simulations by Ntormousi et al. (2020).

Small-scale dynamos generate small-scale (also called *turbulent*) fields, while large-scale dynamos amplify the mean field. Since galaxies contain both turbulent and mean fields we infer that the fields are amplified by some combination of small and large-scale dynamos.

Regardless of the scale, all proposed dynamos rely on the presence of turbulence within the system. Supernova feedback in star-forming disks is a robust source of turbulence that stirs the ISM and has been shown to be directly coupled to the amplification rate of the fields (Rieder and Teyssier; 2016; Butsky et al.; 2017). Supernova-driven turbulence tends to be isotropic and distributed throughout the ISM, making it an effective driver of the small-scale dynamo. In addition to stellar feedback, several instabilities may generate turbulence important to dynamo action, such as the magnetorotational instability (MRI) (Balbus and Hawley; 1991; Sellwood and Balbus; 1999; Korpi et al.; 2010; Gressel et al.; 2013), gravitational instability including spiral arms themselves(Toomre; 1964; Krumholz et al.; 2018; Pfrommer et al.; 2022), and cosmic ray instabilities (Bell; 2004; Riquelme and Spitkovsky; 2009).

Sellwood and Binney (2002) showed how transient spiral patterns in a galaxy disk can cause efficient radial mixing of the stars within the disk. As a spiral instability grows, the non-axisymmetric potential well first traps stars near corotation onto orbits that cross corotation. Trapped stars may cross the resonance more than once as they alternately gain and lose angular momentum. Later, as the disturbance decays, trapped stars may

be released at new radii with substantially changed angular momenta. A succession of transient spiral patterns having differing corotation radii can cause stars to random walk in several steps over large radial distances from their birth radii, a process that was also studied by Roškar et al. (2008) and by Daniel and Wyse (2018) and has been shown by Frankel et al. (2020), for example, to have been an important driver of evolution in the Milky Way disk over the past 6 Gyr.

While radial migration due to spirals was first understood as a stellar dynamical phenomenon, Sellwood and Binney (2002) argued that clouds of gas should exhibit similar behavior, i.e. they become trapped by the gravitational potential of a growing spiral, cross corotation, and then are released in a similar manner to the stars. Magnetized gas will drag its entrained magnetic field, which will stretch the field in the radial direction at first, after which it will be sheared by differential rotation, while parcels of magnetized gas from different radii become mixed, thereby stirring the medium on much grander scales than is possible by supernova-driven turbulence, for example. A more general version of this picture would allow for field to be dragged by spiral-linked gas flows without necessarily requiring compact clouds.

The extent of radial flows caused by spirals naturally depends on their peak amplitude, and also the multiplicity of the spiral pattern. Several studies of magnetized spiral galaxies have employed submaximum disks (e.g. Wibking and Krumholz; 2023; Robinson and Wadsley; 2024), causing them to prefer multi-arm spirals (Sellwood and Masters; 2022) that drive radial flows over shorter distances. Simulations by Khoperskov and Khrapov (2018) and by Kim et al. (2006) directly investigated the relationship between spiral arms and magnetic field amplification and found that galaxies produce stronger mean-fields within spiral arms. Ntormousi et al. (2020) found evidence for a mean-field dynamo operating in simulations of a forming spiral galaxy, but did not investigate the role of the spiral arms directly. Altogether this motivates simulations that can clearly demonstrate the role spiral arms play in galactic magnetic field evolution.

Another effect commonly associated with spiral patterns is the promotion of star formation. A key question is whether they *trigger* star formation at increased efficiency or *gather* gas that forms stars at typical rates (Elmegreen and Elmegreen; 1986; Sellwood and Masters; 2022). Recent observational results have begun to favor the 'gather picture, where spiral arms bring together gas that is already going to undergo star formation, but affect the overall efficiency by negligible amounts (Sun et al.; 2024; Querejeta et al.; 2024). The stratified sheared patch simulations of Kim et al. (2020) also favor the gather picture.

In this work, we compare simulations of an isolated galaxy with and without spiral arms, but with setups and physics that are otherwise identical. The spiral arms form as natural instabilities in the first simulation (i.e. they are not imposed as a fixed potential), which properly captures their transient nature. Comparison of the two simulations then allows us to study the role of spirals in both magnetic field amplification, and in the triggering/gathering of star formation.

The remainder of this paper is organized as follows: In Section 3.2 we describe our numerical methods and simulation setup, in Section 3.3 we present the results of the simulations, in Section 3.4 we discuss the implications, and in Section 3.5 we make some broad conclusions.

3.2 Methods

We conduct MHD simulations of two initially identical, isolated galaxies, but allow spiral arms to develop in one and inhibit their formation in the other. Our methods mostly follow Robinson and Wadsley (2024). We use the RAMSES adaptive mesh refinement (AMR) code Teyssier (2002) that solves the ideal MHD equations using a Harten-Lax-van Leer discontinuities (HLLD) approximate Riemann solver. We use the constrained transport method (Evans and Hawley; 1988) to maintain the solenoidal constraint ($\nabla \cdot \mathbf{B} = 0$), and a particle-mesh technique (Hockney and Eastwood; 1981) to determine the gravitational attraction of stars, dark matter and gas. Cooling and heating processes in the gas are accounted for through the GRACKLE chemistry and cooling library (Smith et al.; 2017), which utilizes metal cooling rates from the photo-ionization code CLOUDY (Ferland et al.; 2017). We include a photoelectric heating rate of $\zeta = 4 \times 10^{-26}$ erg cm^{-3} s^{-1}.

Star particles are formed stochastically with a Schmidt-Law of the form:

$$\frac{d\rho_*}{dt} = \frac{\epsilon_{\rm ff}\rho}{t_{\rm ff}} \quad \text{if} \quad \rho > \rho_{\rm crit} \tag{3.1}$$

where ρ_* is the stellar density, $\rho_{\rm crit}$ is a threshold density which corresponds to a number density of 100 cm^{-3}, and $\epsilon_{\rm ff}$ is the star formation efficiency per free-fall time. To reduce the magnitude of an initial starburst, we initially set $\epsilon_{\rm ff}$ to 0.01, and gradually increase it to 0.1 over the first 200 Myr of evolution to suppress any initial starburst.

In order to mimic supernova feedback, we assume each newly formed star particle releases 10^{51} erg per 91 M$_\odot$, after a 5 Myr delay. We prevent the released energy from

cooling at first using the delayed cooling model of Agertz et al. (2011), which allows unresolved superbubbles to grow properly, but it is then converted into regular thermal energy with an e-folding timescale of 5 Myr. The gas disk is initialized inside of a domain 600 kpc on a side that has a base grid of 64^3 cells, that is allowed to refine an additional 10 levels which gives a spatial resolution of 9.15 pc at the highest level.

3.2.1 Galaxy models with and without spirals

We created a self-consistent, equilibrium dark matter halo and the initial stellar disk as described in the Appendix and use it for both simulations.

We allow spirals to develop in one model, by evolving the stellar disk and DM halo for 400 Myr without gas. Once spiral arms have developed, we subtract 10% from the masses of the disk star particles and convert that mass to gas in an exponential disk with a scale-height and scale-radius of 0.34 kpc and 3.4 kpc respectively. In this way, we begin the full MHD simulation with a stellar disk that has already developed spiral arms. The initial magnetic field embedded within the gas disk is purely toroidal with a field strength

$$B = 0.85 \left(\frac{\rho}{\rho_0} \right)^{2/3} \ \mu\text{G}, \tag{3.2}$$

where $\rho_0 = 1.15 \times 10^{-23}$ g cm^{-3} is the initial density at the galaxy center. These choices result in a magnetic field strength of 0.1 μG in a typical ISM number density of 0.25 cm^{-3}.

To inhibit stellar spirals from forming in the second model we measured the initial axisymmetric values of the gravitational accelerations of the disk star particles as a function of radius, and modified Ramses to continuously use those values rather than those calculated by the gravity solver. This forces the stellar disk to remain axisymmetric and prevents any stellar spiral arms from forming. The gas and DM halo continue to respond to their own self-gravity and that of the stellar disk particles.

From this point on we shall refer to the two models as the spiral galaxy, and the no-spiral galaxy.

3.3 Simulation Results

Both galaxies begin their evolution with an initial starburst that lasts $\sim$ 200 Myr. These initial bursts are typical in isolated galaxy simulations. However, the amplitude is reduced here via a gradual ramping up of the star formation efficiency per free-fall

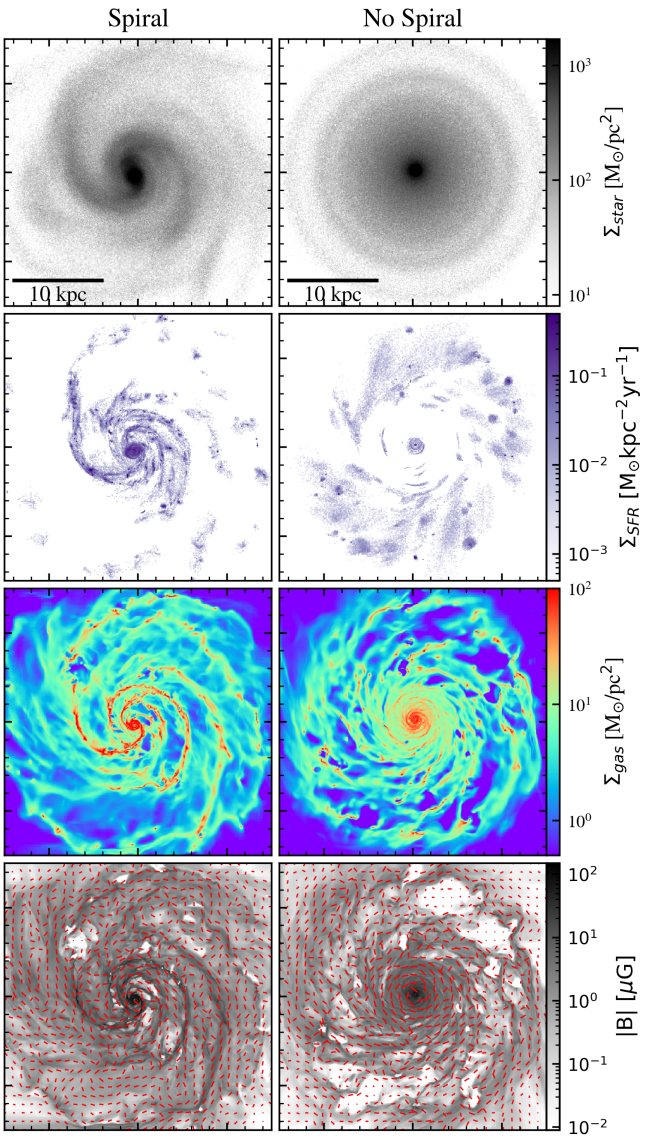

FIGURE 3.1: Visualizations of stellar surface density (top row), star formation rate surface density (second row), gas surface density (third row), and mass-weighted magnetic field strength (bottom row) for each galaxy at t=600 Myr. Gas surface density and magnetic field strength are calculated using gas within 1 kpc of the midplane. SFR is calculated using all star particles that formed during the previous 100 Myr. The bottom row shows mass-weighted magnetic field strength smoothed over 1 kpc scales in grayscale with directions indicated by line segments.

time parameter. During the 1 Gyr of evolution, the spiral galaxy develops global spiral arms that are reflected in both the stellar and gas disks. The spiral arms are transient in nature, and shift between a 2, 3, and 4 armed spiral. The no-spiral galaxy remains axisymmetric in the stellar disk, but the gas disk develops some localized, spiral-like structure. These are associated with superbubbles that are sheared out into trailing shapes. After roughly 800 Myr, the spiral galaxy begins to develop a central bar in both the stars and gas. Interestingly, the bar does not form in the stars-only simulation (see Figure 3.12).

Figure 3.1 shows images of the stellar surface density, star formation rate surface density, gas surface density, and magnetic field strength after 600 Myr of evolution. The stellar surface density in the upper left panel reveals a large-scale, mostly bi-symmetric, spiral pattern in the spiral galaxy. The stellar disk in upper right panel shows the no-spiral model has remained axi-symmetric.

The spiral structure is also reflected in the star formation rate surface density (second row); almost all of the star formation occurs within the spiral arms of the spiral model, but is spread out diffusely in the no-spiral model.

The third row shows the surface density of gas in each model, created by a projecting of all gas within 1 kpc of the midplane. In the spiral model, gas is concentrated in the spiral arms, resulting in more high surface density gas in that case overall. In the no-spiral model, superbubbles carve large holes into the low-density ISM and create structures resembling higher multiplicity spirals as those regions are sheared out.

The bottom row shows a projection of mass-weighted magnetic field strength $|B|$, with lines indicating the direction of the magnetic fields within the plane of the disk. Mass-weighting favours the field in the denser gas tracing the spiral arms. In both models, magnetic field strengths follow the density structure of the galaxy, with the interiors of superbubbles containing weak fields. The magnetic fields in the spiral galaxy are stronger, even in the inter-arm regions where the gas surface density is low. In the spiral model, the mean field tends to follow the spiral arms in a manner similar to observed spiral galaxies (Fletcher et al.; 2011)

3.3.1 Star Formation

Figure 4.5 outlines the star formation histories of the galaxies. The top panel shows the time evolution of the total star formation rate. Both models begin with an initial burst of star formation that is followed by a gradual decrease. After the initial burst,

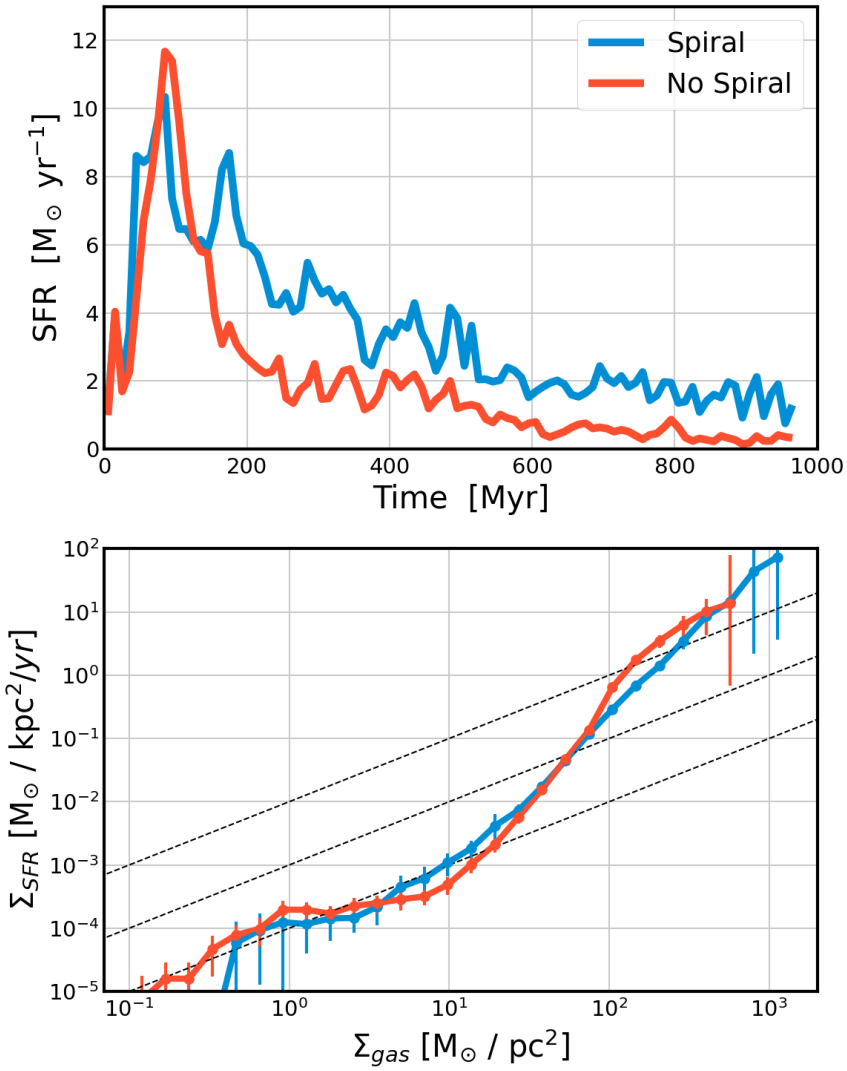

FIGURE 3.2: Total SFR (top panel) and Kennicutt-Schmidt relation (bottom panel) for each galaxy. SFR is calculated by summing the mass of stars formed in each time bin and dividing by the bin size. Vertical lines show the 95% confidence interval of the mean. Diagonal lines in the bottom panel indicate constant gas depletion times of 10^8, 10^9, and 10^{10} years, as done in (Bigiel et al.; 2008).

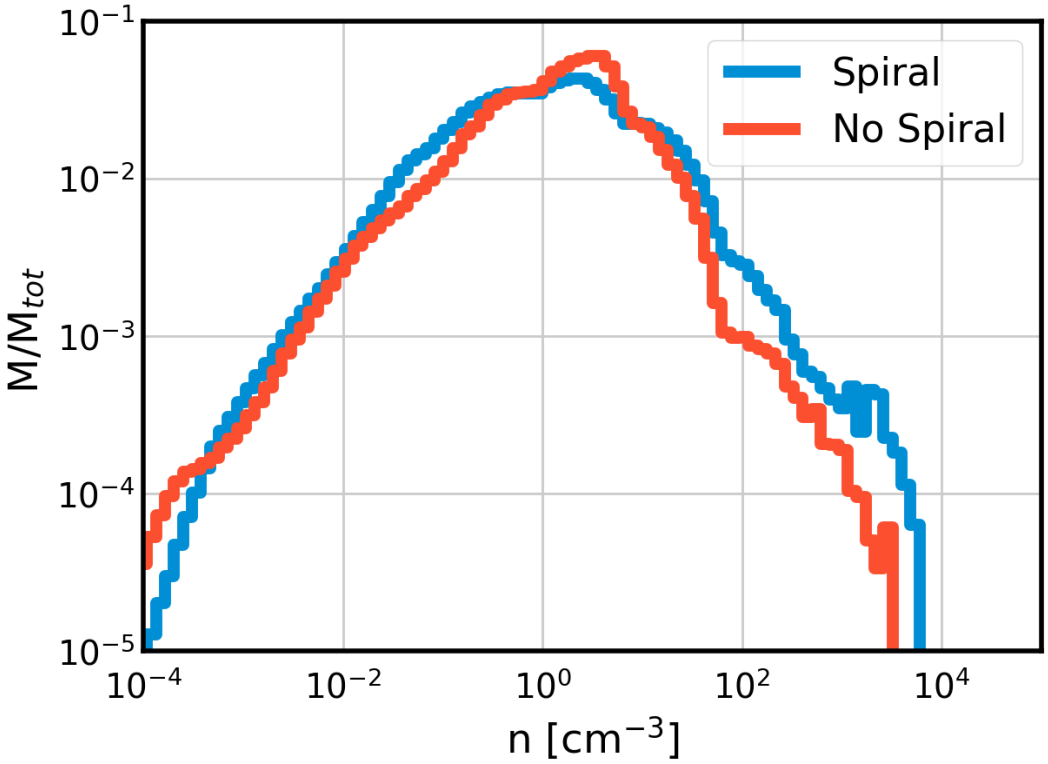

FIGURE 3.3: Histogram of gas number densities. Each bin represents the total mass within that density range inside a disk with radius 15 kpc and 1 kpc height, normalized by the total mass within that disk. The spiral galaxy has more high density gas, which results in higher star formation rates.

the spiral galaxy has a higher star formation rate (SFR) than the no-spiral galaxy for all of the subsequent evolution. The star formation rate in the no-spiral galaxy drops to 0.3 $M_\odot$ yr^{-1} after 1 Gyr of evolution, and the rate in the spiral galaxy is 1.2 $M_\odot$ yr^{-1}. This difference persists even though the no-spiral galaxy always has a larger reservoir of remaining gas; at 800 Myr there is 6.25 $\times 10^9$ $M_\odot$ of gas remaining in the spiral galaxy compared to the 7.43 $\times 10^9$ $M_\odot$ in the no-spiral galaxy. Between 300 and 800 Myr (after the initial starburst and before the bar forms in the spiral galaxy), the spiral galaxy has an average SFR 2.6 times higher than the no-spiral galaxy. This result alone shows that the presence of spiral arms in galaxies can cause a significant increase in the star formation rate.

The lower panel of figure 4.5 shows the Kennicutt-Schmidt relation for each model, which is calculated by dividing the galaxy into 100 pc sized patches and summing the total mass of stars formed within the last 10 Myrs. To ensure a large enough sample, the calculation is done on 30 outputs from 500-650 Myr, and the mean SFR surface density is plotted in each bin. In both models there is a scatter of over 6 orders of magnitude, but the mean SFR surface densities are generally quite similar at a given gas surface density. There are some minor differences. At surface densities of 10 $M_\odot/pc^2$, the spiral model has a factor of 2 higher SFR, and at 200 $M_\odot/pc^2$, the no-spiral model has a factor of 2 higher SFR.

To understand the SFRs, the 3D density must also be taken into account because SFR is based on the local density via a Schmidt-law. In figure 3.3, we show gas density histograms. The spiral galaxy has more gas at densities above 100 cm^{-3}, which is the star formation threshold. This is required to enable the overall higher SFR. As noted above, we do not see a higher star formation rate for a given gas column density in figure 4.5 in the spiral case. This is slightly counterintuitive: given the significant contribution of the vertical gravity field from the stellar disk, one might expect the gas to have smaller scale heights within the spirals, meaning higher 3D densities and higher SFRs for the same gas column. However, turbulence injected by stellar feedback supports the gas against gravity so that the average midplane 3D density is moderately higher in the quieter no-spiral model. For example, at a surface density of 10 $M_\odot/pc^2$, the no-spiral model has a average midplane density of 0.067 $M_\odot/pc^3$, and the spiral model has an average midplane density of 0.036 $M_\odot/pc^3$ (higher scale heights). This is consistent with the spiral galaxy having more turbulence in this gas, with an average velocity dispersion of 12 km/s vs 6.5 km/s in the no-spiral galaxy. The increased turbulence in the spiral galaxy also drives more clumping to enable the higher star formation rate here. This

illustrates how complicated it is to connect column densities with star formation rates even with a relatively simple star formation model.

Thus the differences in SFR are mainly driven by the overall amount of high-column density gas, of which there is much more in the spiral model, seen gathered along the spiral arms in figure 3.1). The spirals sweep up gas and increase the surface density without decreasing the depletion time. This favours the argument that spiral arms simply *gather* star-forming gas (Elmegreen and Elmegreen; 1986; Querejeta et al.; 2024; Sun et al.; 2024), rather than acting as a mechanism to trigger more star formation at a fixed gas column. The difference in star formation rates plays a role in the magnetic field amplification due to increased turbulence injected from the stellar feedback, powering the small-scale dynamo.

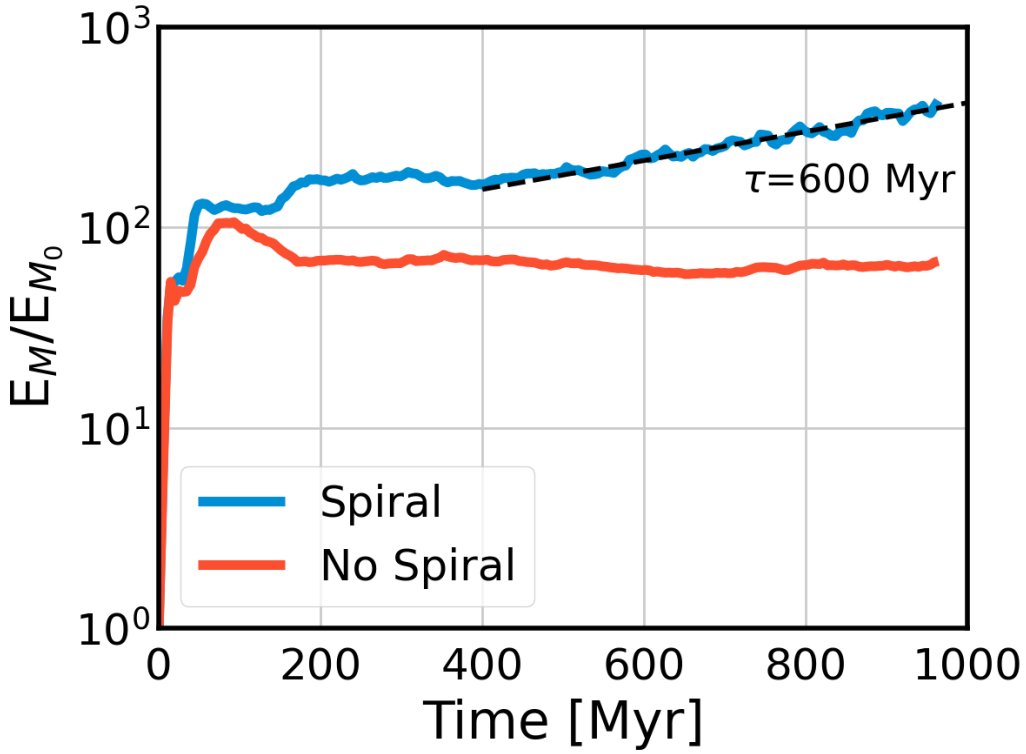

FIGURE 3.4: Total magnetic energy evolution in each galaxy. Magnetic energy saturates in the no spiral galaxy after 200 Myr, but slower growth continues in the spiral galaxy. Dashed line shows exponential growth that goes as $E_M \propto \exp(t/\tau)$.

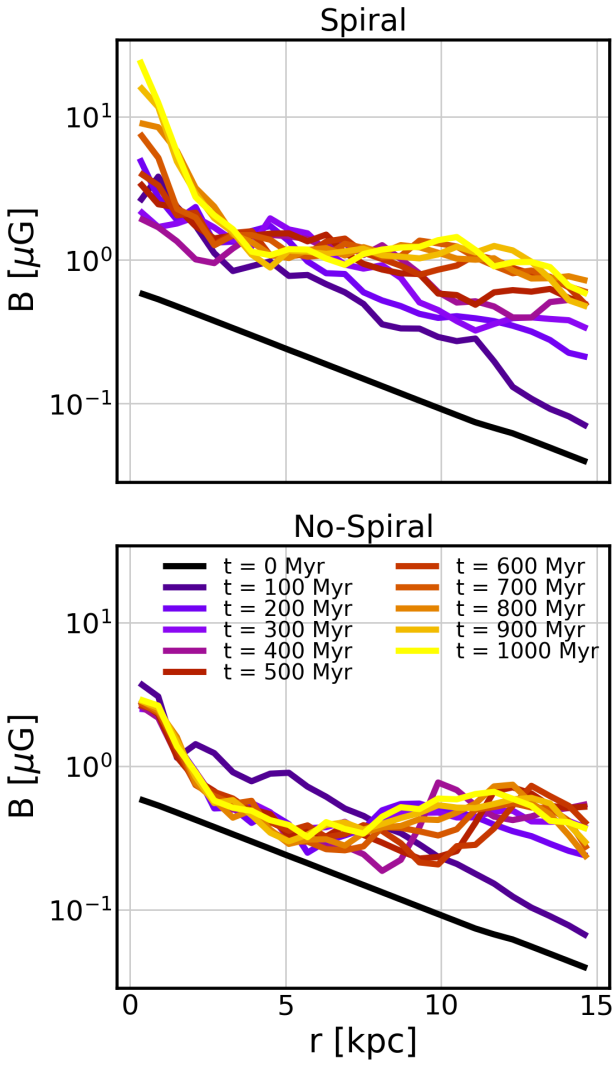

FIGURE 3.5: Volume-averaged magnetic Field Strength versus radius over time in each galaxy. The spiral galaxy saturates with stronger fields than the no-spiral galaxy.

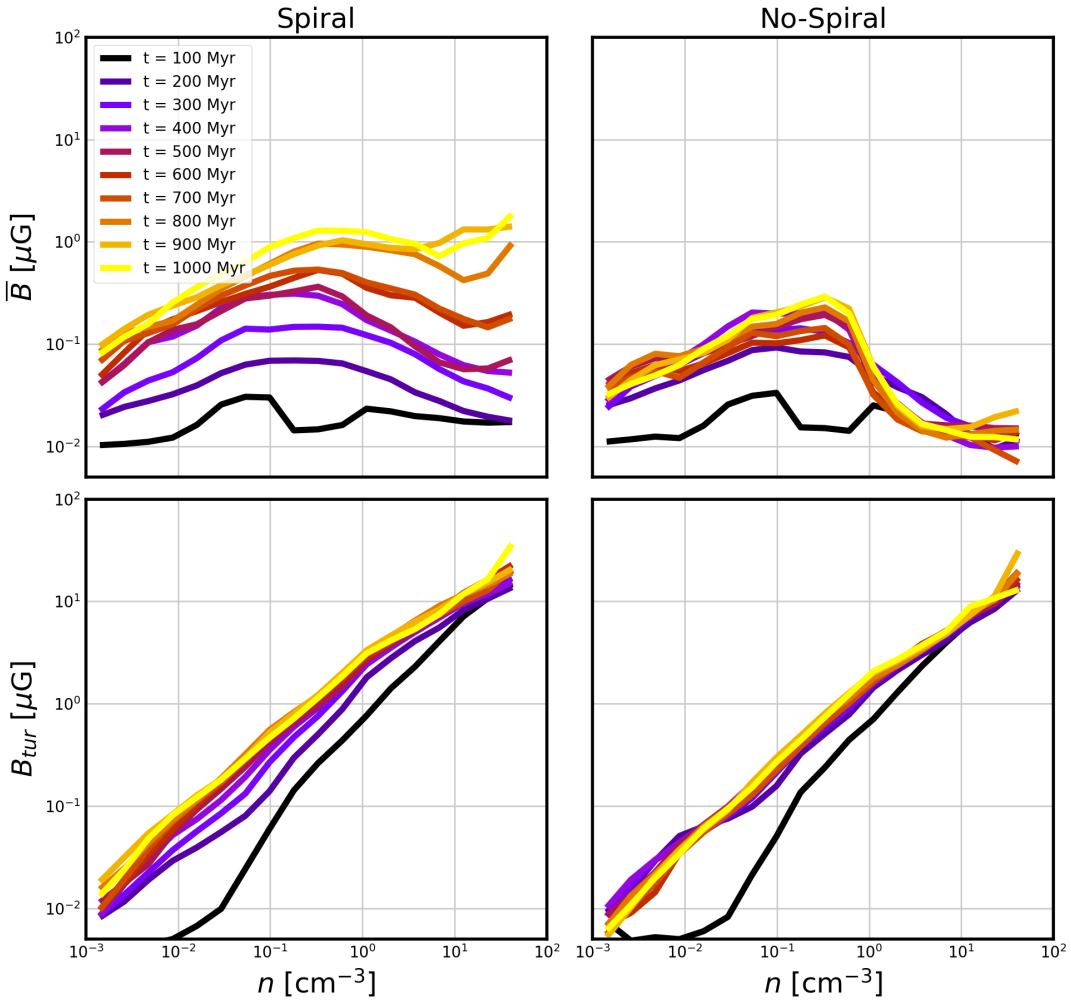

FIGURE 3.6: Strength of the mean field (upper panels) and turbulent field (lower panels) versus density in each galaxy over time. Amplification of the mean field can be seen in the spiral galaxy in the upper-left panel. The mean field is calculated by applying a median filter over scales of 500 pc. Plotted values are are calculated within a disk of radius 15 kpc and height 1 kpc.

3.3.2 Magnetic Field Evolution

We now examine the evolution of the magnetic fields. Figure 3.4 shows the evolution of the total magnetic energy within the whole simulation. In both galaxies, there is rapid growth during the first 100 Myr, coinciding with heightened turbulence associated with a moderate starburst. This is consistent with the presence of an efficient small-scale dynamo (Rieder and Teyssier; 2016). The spiral galaxy field grows due to second burst of star formation near t=180 Myr. At late times, (500-1000 Myr), the spiral galaxy enters a phase of steady growth, with an exponential growth timescale of $\tau = 600$ Myr. This is indicative of the presence of a slower, large-scale dynamo, as outlined in the following sections.

This growth can also be seen in figure 3.5, which shows the volume-averaged magnetic field strength as a function of radius in each simulation over time. For this analysis we choose to use volume-weighted fields as they reflect the total magnetic energy present and the support provided by magnetic pressure. It also allows us to characterize the typical strength at a given radius as volume averages are less affected by the transient passage of density feature such as spirals. Typical volume-averaged values are low ($\sim$ 1 μG) compared to mass-weighted spiral arm values ($\sim$ 3-30 μG) shown in figure 3.1. Weighting choices were previously evaluated in Robinson and Wadsley (2024), who noted that the strength ratio is fairly consistent between mass and volume weighting. Thus volume weighting is a straight-forward way to examine the relative differences between the spiral and no-spiral cases.

Figure 3.5 demonstrates how the magnetic fields amplify quickly during the first 200 Myr in both models, but they subsequently saturate outside $\sim$ 3 kpc. Saturation occurs earlier in the no-spiral, while the spiral grows further to around 1 μG. At late times (600 Myr-1 Gyr), the resulting volume weighted average magnetic field strength in the spiral galaxy is 1 μG outside of the central 5 kpc. The no-spiral galaxy has weaker field strengths overall, with values ranging from 0.3-0.5 μG past 5 kpc. In both models, the stronger fields correspond to regions of higher SFR. For example, in both models the fields are stronger in the center of the galaxy where star formation is concentrated, and in the no-spiral galaxy the field strengths increase in the outer disk where star formation is ongoing (see figure 3.1). This shows that the small-scale dynamo plays an important role in setting the overall magnetic field strengths in both cases.

3.3.3 Large-scale vs. Small-scale Field Evolution

To further examine the large-scale dynamo, we decompose the magnetic field into mean and turbulent components, defined as $\mathbf{B_{turb}} = \mathbf{B} - \bar{\mathbf{B}}$, where the mean field $\bar{\mathbf{B}}$ is calculated using a median filter applied over 500 pc. Figure 3.6 shows the mean and turbulent field vs. gas number density in each galaxy over time.

The upper left panel shows that the large-scale dynamo in the spiral galaxy has continuously enhanced the mean field at all densities. At 1 Gyr, intermediate density gas has reached a mean field strength of 1 μG. The upper right panel shows the mean field in the no-spiral galaxy, which has limited long-term amplification. We note that $\sim$1 cm^{-3} marks a transition from diffuse to dense gas structures.

The bottom panels show the turbulent component, which is stronger above $\sim$ 0.3 cm^{-3} in both galaxies. The turbulent field follows similar saturation behaviour to the total field shown in figure 3.5, saturating earlier in the no-spiral at a lower value for a given density. It remains saturated in both cases from $\sim$ 500 Myr. The higher turbulent field at saturation in the spiral case is expected due to the higher levels of turbulence and feedback in that case.

The turbulent field retains power-law behaviour similar to the 2/3 power law that was included in the initial condition and flattening to a roughly 1/2 power law at moderate to higher densities. A power-law relationship between field strength and gas density, $B \propto \rho^{\alpha}$, is seen in both observations and in a wide range of MHD simulations of processes in the interstellar medium (Whitworth et al.; 2025). It is found to vary typically between 1/2 and 2/3 . Field growth at fixed density, as shown in figure 3.6, is a clear signal of dynamo action.

3.3.4 Magnetic Field Power Spectra

To better understand the scale dependence of the magnetic field evolution, we calculate the power spectra of the magnetic field and its cylindrical components. In figure 3.7, we plot the total angle-averaged power spectrum of the magnetic field defined as

$$P(k) = \langle \tilde{B}(k) \cdot \tilde{B}(k)^{*} \rangle \tag{3.3}$$

where $\tilde{B}$ is the Fourier transform of the magnetic field, k is the wavevector, and * indicates the complex conjugate. The angled brackets indicate an 'angle-average' which yields a one-dimensional power spectrum by binning $P(k)$ in wavevectors $k = |k|$ and

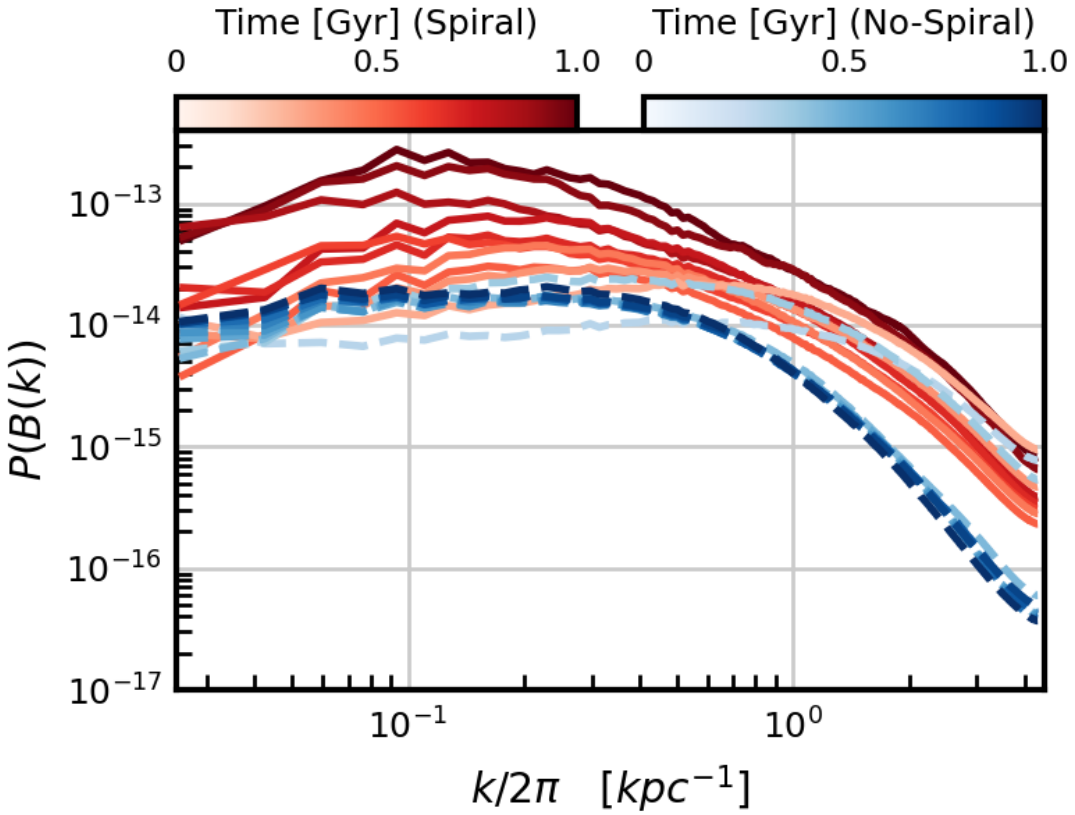

FIGURE 3.7: Total magnetic field power spectra in each galaxy. Each line shows a different time, going from 100 Myr (light shaded) to 1 Gyr (dark shaded). Power spectra are calculated in a cube of side-length 9.375 kpc centered on the galaxy. The power spectrum in the spiral galaxy shows continued growth up to 1 Gyr, while in the no-spiral galaxy there is no long-term growth. The power spectrum in the spiral galaxy peaks at scales near 10 kpc, which is a similar scale to those of spiral arms.

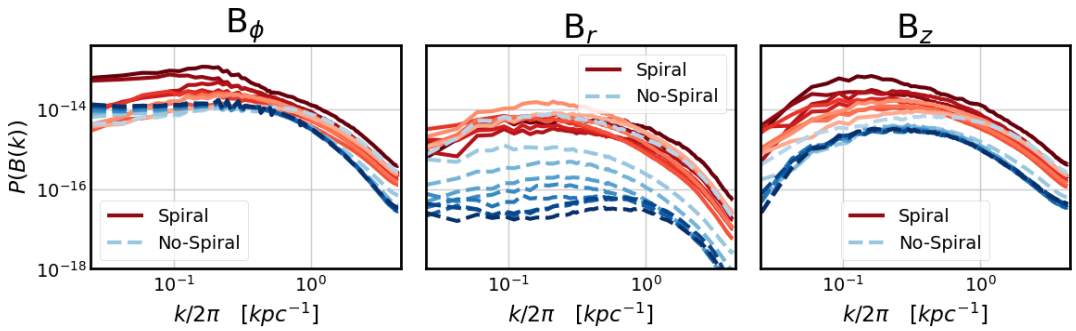

FIGURE 3.8: Power spectra of the azimuthal, radial, and vertical field components over time. Each line shows a different time, going from 100 Myr (light shaded) to 1 Gyr (dark shaded).

dividing by the number of points in each bin (Joung and Mac Low; 2006). The power spectra are calculated on an 18.3 pc resolution cube of side-length 10 kpc centered on the galaxy.

In figure 3.7, the magnetic field continues to grow on all scales in the spiral galaxy throughout the 1 Gyr of evolution, compared to the no-spiral model which shows little to no growth at all scales. This reflects the stronger magnetic fields in the spiral galaxy discussed in the previous section spiral galaxy. However, at late times there is more growth in the spiral galaxy on large ($>$ 10 kpc) scales, which implies a large scale ordering of the field on the scale of spiral arms.

Figure 3.8 breaks the magnetic field power spectrum into its three cylindrical components: vertical, radial, and azimuthal. In the left panel, the toroidal component can be seen steadily growing in the spiral galaxy, but in the no-spiral galaxy there is little growth. In the radial component, the power spectrum of the spiral galaxy remains steady, but the no-spiral galaxy consistently loses power at all scales over time. The z-component steadily grows in the spiral galaxies, and slightly loses power in the no-spiral galaxy.

After 1 Gyr of evolution, the field is dominated by the azimuthal component in both galaxies. The vertical (z) component is a factor of two weaker than the toroidal at 10 kpc scales in the spiral galaxy, and a factor of five less in the no-spiral galaxy. Power in the z-component drops steeply at large scales, which implies that the largest-scale vertical field is created by kpc-scale feedback events that drag magnetic fields upwards. These events are galactic fountains with material reaching heights of 3-5 kpc, which is

consistent with the peak of the z-component power spectrum. The radial field component is the weakest, being almost two orders of magnitude lower than the toroidal component in the spiral galaxy, and almost 3 orders of magnitude lower in the no-spiral galaxy.

The components of the field are visualized in figure 3.9. In the top row, the toroidal component of the field shows ordered fields in the spiral galaxy. In the upper left panel, there is a coherent field with strengths near 10 μG following the spiral arm structure, disrupted only by the formation of a superbubble, and there are field reversals in the inter-arm regions. In the no-spiral galaxy, there is no spiral structure to follow and the field becomes increasingly wound up in the central 10 kpc, which is a region that has low star formation rates. The z-component of the field is more randomly distributed in both galaxies, with no visible structure linked to the spiral arms. This supports the idea that the vertical component of the field is associated with localized turbulence. The overall strength of the vertical field is weaker in the no-spiral galaxy, because of the lower star formation rate sustains weaker feedback-driven turbulence. The radial components of the field are shown in the bottom row, which also shows large scale structure associated with the spiral arms, which was reflected in the power spectrum.

3.3.5 Dynamo Mechanism

The field strengths in figure 3.5 and the bottom panel of figure 3.6 provide convincing evidence for a small-scale dynamo powered by turbulent motions, which were in turn generated via feedback from star formation.

In the earliest phases, the fields are not strong enough to affect the gas flows, so the small-scale dynamo operates in the kinetic regime which leads to exponential growth rates. The small-scale dynamo saturates when the fields become strong enough to back-react onto the flow. Rapid field growth followed by saturation or slower growth rates is consistent with the two phases of amplification demonstrated in simulations by Rieder and Teyssier (2016, 2017).

In addition to the small-scale dynamo, a mean-field dynamo similar to that proposed by Sellwood and Binney (2002) can explain the mean-field amplification and power spectra. In this mechanism, the dynamo is powered by radial flows driven by the spiral arms.

This process will generate large-scale radial fields as the primarily toroidal fields are dragged radially by large-scale gas flows near spiral arms. In the no-spiral galaxy there are no coherent motions to regenerate these radial fields, and the radial field

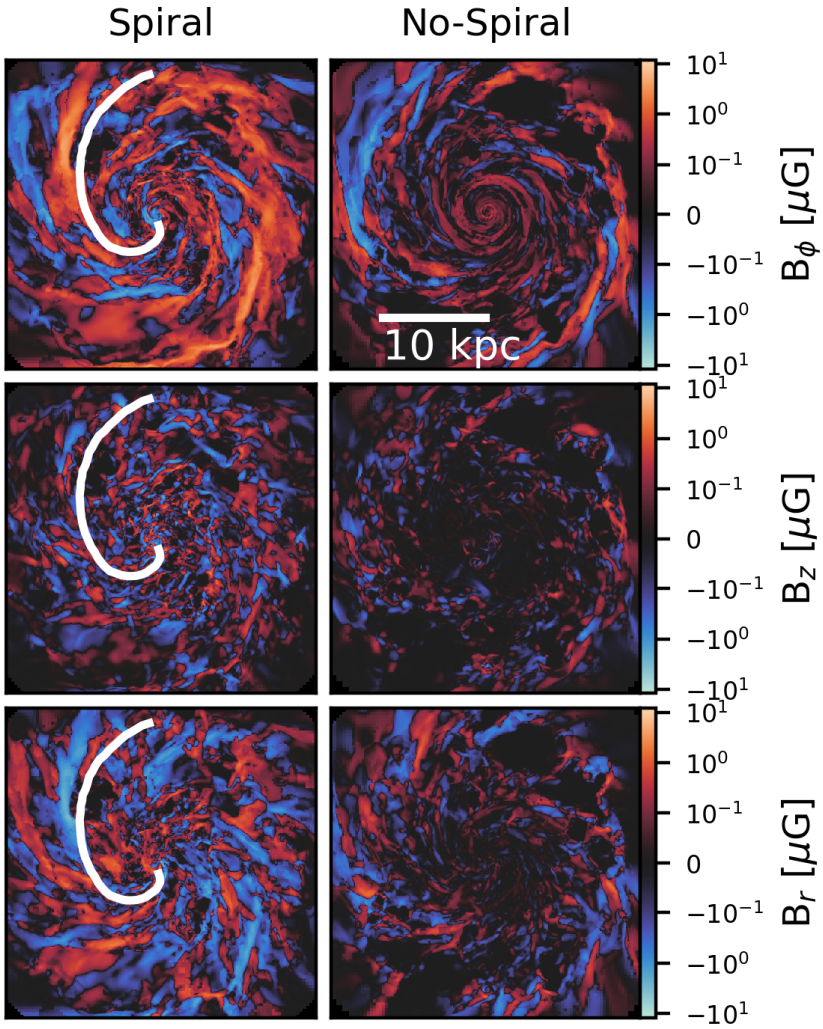

FIGURE 3.9: Projections of azimuthal (top row), vertical (middle row), and radial (bottom row) magnetic field components, at time t = 600 Myr. The white solid line shows the location of the left spiral arm in the stellar surface density shown in fig. 3.1.

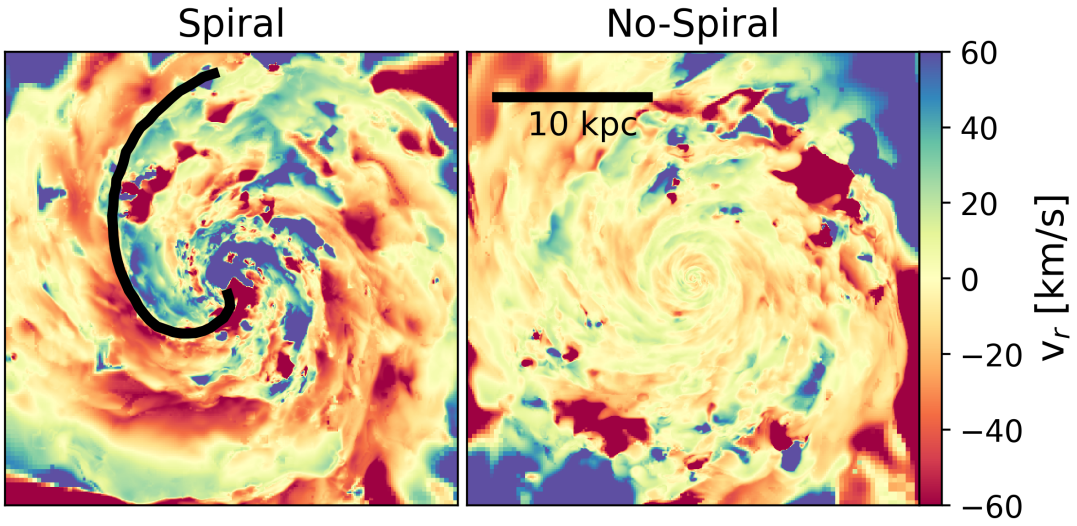

FIGURE 3.10: Mass-weighted vertical average of the radial velocity of gas inside a disk of 1 kpc height at t= 600 Myr. Radial velocities are in the plane of the disk, and are positive for outward motion. The solid line shows the location of a spiral arm identified in the stellar surface density shown in fig. 3.1.

components continually decay as they are sheared into toroidal fields by the Ω effect. In essence, the mean-field growth is limited because large scale radial fields have no generation mechanism. In the spiral galaxy, radial fields are also sheared out by the Ω effect, however the spiral arms provide a mechanism that can constantly replenish the radial fields at the same time they are being sheared out.

Figure 3.10 shows the radial velocity in each simulation at 600 Myr, with the location of one spiral arm shown by a solid line. The spiral is created by the streaming flows of stars and gas around the galaxy converging as they approach the arm and diverging again after passing through it. The motion is predominantly azimuthal, with circular velocities near 200 km/s through most of the disk, with the spiral potential adding a coherent radial part, with speeds up to $\sim$ 50 km/s that cause the stream lines to converge and diverge at the appropriate phases. These flows are completely absent in the no-spiral galaxy due to the absence of spiral arms. In the spiral galaxy, the small but coherent radial flows will drag magnetic fields with them, constantly replenishing the radial fields, which is a key process in maintaining the mean-field dynamo.

We can compare these results with established mean-field dynamo theories. Classical $\alpha - \Omega$ dynamo theory predicts a quadrupolar field being generated in the galactic halo

(Stix; 1975; Shukurov et al.; 2019), which has been demonstrated in simulations by Ntormousi et al. (2020). We do not see evidence for quadrupolar fields in the galactic halo of our simulations, nor the presence of individual Parker loops twisting above the spirals. The material 3-5 kpc above the disk is associated with galactic fountains from local feedback events. However, because of the lower numerical resolution in the halo due to the refinement scheme used in RAMSES, we cannot make strong claims about behaviour in the galactic halo. Another factor is that our simulations were only evolved for 1 Gyr which may not be long enough for the $\alpha - \Omega$ dynamo to fully develop. A clear similarity to the $\alpha - \Omega$ dynamo that we have shown is a conversion of fields between radial and toroidal components, resulting in a net-increase of toroidal field strength.

Despite the strong turbulent fields in high-density gas, the majority of magnetic energy resides in the mean field, due to the low density gas having a much higher volume. This means that the mean-field plays a dominant role in the large-scale dynamo amplification from 600-1000 Myr. The radial fields that are used in the dynamo are the large-scale mean-field created by the spiral flows, rather than turbulent fields created by local feedback events

Our simulations manifest spiral driven radial flows that we identify as promoting the large-scale dynamo, but they lack the resolution to fully capture the dynamics of a realistically clumpy ISM. The radial migration of gas clouds in response to transient spirals, predicted by (Sellwood and Binney; 2002) and described here in the introduction, would provide a further driver of large-scale turbulence, and perhaps lead to more vigorous growth of large scale mean field.

3.4 Discussion

This work shows that star formation and magnetic field amplification are qualitatively different when spiral arms are included. However, there are several caveats.

We primarily employ volume-weighted field measurements (typical values ~ 1 μG) for the reasons discussed in section 3.3.2. Mass-weighted measures are typically higher, in the range $3-30$ μG (as shown in figure 3.1). Volume-weighted averages of $3-30$ μG can also be inferred for denser gas > 1 cm^{-3}, as shown in figure 3.6. For comparison, large-scale field strengths of order 10-20 μG commonly reported in observations of nearby spiral galaxies (Fletcher et al.; 2011; Basu and Roy; 2013; Beck and Wielebinski; 2013). Those values reflect specific emission processes and assumptions that were made to interpret them and do not correspond directly to either of our weighting scheme (Basu and Roy;

2013; Ponnada et al.; 2022). Synchrotron observations, in particular, often assume an equipartition of energy between magnetic fields and cosmic rays, which may lead to the magnetic field strengths being overestimated (Dacunha et al.; 2025).

Additionally, the simulations do not resolve high-density gas which has the strongest fields. This is the gas probed with Zeeman effect measurements (Crutcher et al.; 2010; Whitworth et al.; 2025). It would be interesting to explore detailed mock-observations in future work.

This work also does not account for the evolution of cosmic rays or non-ideal MHD effects like ambipolar diffusion. Ambipolar diffusion operates on scales that are small compared to these simulations so it is unlikely to be important. Cosmic rays are closely associated with magnetic field evolution and affect overall gas support (Semenov et al.; 2021). There is still considerable uncertainty in modeling cosmic rays, but including them in these simulations is another future direction.

Our result that the generated fields are mainly toroidal may be influenced by the initial condition which contains a weak toroidal field. Toroidal fields are the natural choice because any initial radial or vertical components would rapidly be sheared out into a toroidal field. Nonetheless, it would be an interesting study to begin with several different field morphologies, and determine if the results remain the same. We also do not include more advanced stellar feedback models such as the superbubble model (Keller et al.; 2014), which may drive turbulence more effectively and effect the small-scale dynamo. Stronger feedback may also drive larger-scale outflows and galactic fountains, which could generate large-scale z-component fields, or affect the development of quadrupolar fields in the halo.

3.5 Conclusions

In this work, we simulated two magnetized disk galaxies that are manifestly the same except for the presence or absence of stellar spiral arms. This is a novel addition to the recent literature concerning global MHD galaxy simulations (e.g. Rieder and Teyssier; 2017; Butsky et al.; 2017; Pakmor et al.; 2020; Ntormousi et al.; 2020; Steinwandel et al.; 2020; Ponnada et al.; 2022; Liu et al.; 2022; Wissing and Shen; 2023; Wibking and Krumholz; 2023; Zhao, Pudritz, Pillsworth, Robinson and Wadsley; 2024; Martin-Alvarez et al.; 2024).

We follow the methods of Robinson and Wadsley (2024) and examine the effects of spiral arms on both magnetic field amplification and star formation. The spiral arms were allowed to naturally evolve in the first galaxy, and in the second, a fixed gravitational potential acted on the star particles to keep the stellar disk axisymmetric. The spiral galaxy has higher star formation, driving a stronger small-scale dynamo. A slower, large-scale dynamo is linked to gas flows along the spiral arms.

We summarize our conclusions as follows:

- Spiral arms promote star formation. The simulated spiral galaxy maintains a 2.6 times higher SFR. This is due to high column gas being swept up by the spiral arms (even though there is less gas remaining overall). The star formation rate efficiency remains similar at a given gas column, which supports the conceptual picture that spiral arms *gather* star formation.
- The turbulent component of the magnetic field dominates at early times (< 200 Myr) and remains stronger at higher densities. The magnetic field energy tracks the star formation rate and associated turbulence for the first ~ 200 Myr. The spiral galaxy generates early field strengths that are a factor of 2-3 stronger in the disk than in the no spiral case due to higher star formation.
- The small-scale dynamo generates field in all directional components. However, radial fields are converted to toroidal fields by shear, which produces a long-lived toroidal field. This progressively weakens the radial field in the no-spiral case.
- In the spiral galaxy, the mean-field is amplified by a large-scale dynamo. The mean field strength rises to 1 μG (volume-averaged) over the Gyr of evolution, with an e-folding time of 600 Myr. The no-spiral galaxy mean field saturates at ~ 0.2 μG after 400 Myr, and has no ongoing amplification.
- The spiral large-scale dynamo seen here operates by converting toroidal fields into radial fields and back again. Coherent, large-scale radial gas flows associated with the spiral arms drag the toroidal field to create radial field. Net additional toroidal field is generated after shearing out the radial field. No large-scale vertical field is created.

Acknowledgements

HR is supported by an NSERC postgraduate scholarship, and JW and REP are supported by Discovery Grants from NSERC of Canada. Computational resources for this project were enabled by a grant to JW from Compute Canada/Digital Alliance Canada and carried out on the Niagara Supercomputer. JAS acknowledges the continuing hospitality and support of Steward Observatory.

3.6 Appendix

Our initial disk+bulge+halo model is, like the AGORA model (Kim et al.; 2014), designed to resemble an axisymmetric Milky Way. It differs from their model by having a more massive disk and bulge, in order that it will support fewer spiral arms, while the dense bulge component makes the model less prone to bar instabilities. The equilibrium model has three massive components that are all realized with collisionless particles. Our simulations with the Ramses code employ a smooth gas component that had a mass of 10% of the disk. We therefore reduced the masses of each disk particle by 10% in order to maintain gravitational equilibrium. Alternatively, if the user prefers a code that employs gas particles, the appropriate particle fraction may be labeled by the user as gas particles as desired.

3.6.1 Disk

The disk is a thickened exponential with radial scale length R_d having the volume density

$$\rho_d(R,z) = \frac{M_d}{(2\pi)^{3/2}R_d^2} e^{-R/R_d} \exp\left(\frac{-z}{2z_0}\right)^2, \tag{3.4}$$

with z_0 being the constant disk scale height.

3.6.2 Bulge

The spherical bulge has the cusped density profile proposed by Hernquist (1990)

$$\rho(r) = \frac{M_b a_b}{2\pi r(r+a_b)^3}, \tag{3.5}$$

with M_b being the bulge mass and a_b a scale radius. Hernquist also supplied an isotropic distribution function (DF) for this isolated mass distribution.

3.6.3 Halo

We start from a second, more extensive and massive spherical Hernquist model for the halo component, having mass M_h and radial scale a_h, and impose an outer boundary at $r = 8a_h$ to the otherwise infinite halo. Since the central attraction of the disk and bulge, which are embedded at the center of the halo, destroy the radial balance of the isotropic DF supplied by Hernquist, we must derive a revised equilibrium DF for the halo of the composite model.

Our method to achieve this is a follows: We start from a known DF for the halo with no embedded disk or bulge and compute its density change assuming that the masses of the disk and bulge were increased adiabatically from zero. As was pointed out by Young (1980), adiabatic changes to the total mass profile can be calculated semi-analytically, since the actions (Binney and Tremaine; 2008) of the halo particles do not change as the potential well changes slowly; therefore the DF expressed as actions is the same after the adiabatic change as before.

Blumenthal et al. (1986) assumed angular momentum alone, one of the actions of an orbit, was conserved, but their formula would apply only if the orbits of all particles were initially and remained precisely circular. The orbits of particles in all reasonable spherical models librate radially, and therefore one must take conservation of radial action into account when computing the density response to adiabatic changes to the potential, and the pressure of radial motions makes a realistic halo more resistant to compression than the naïve model with no radial action would predict.

Young (1980) and Sellwood and McGaugh (2005) describe procedures, which we employ here, to include radial action conservation as the potential well changes adiabatically. An initially isotropic DF becomes mildly radially biased, which can still be represented by the unchanged actions. Note that the procedure assumes the potential remains spherically symmetric, so we must approximate the disk potential by the monpole only term, *i.e.* using only the disk mass enclosed in a sphere of radius r. Sellwood and McGaugh (2005) found, from a comparison with a simulation in which a disk was grown slowly inside a spherical halo that the ashperical part of the disk potential caused negligibly small changes to the spherically averaged halo potential.

With the compressed halo potential and DF in hand, we have the global potential of the thickened disk, bulge and halo, and can set the orbital motions of the particles in the usual way Sellwood (2024). Hernquist's isotropic DF adequately describes the bulge equilibrium, since that component dominates the potential in the center.

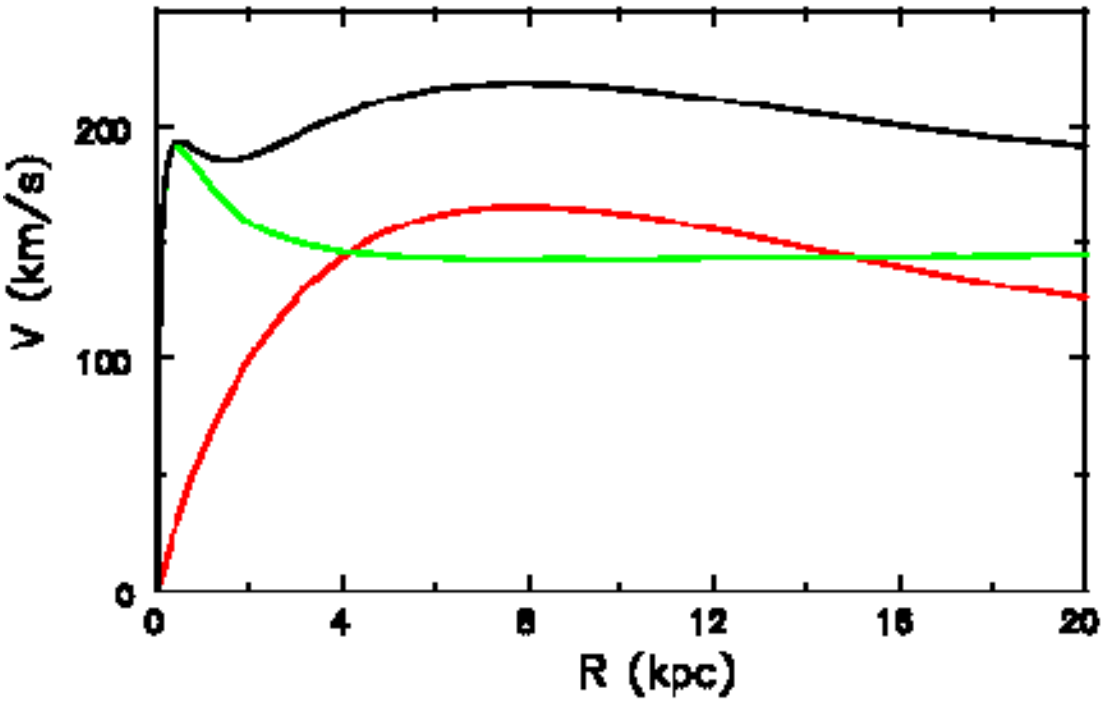

FIGURE 3.11: The black line gives the total rotation curve of our model, after halo compression, with the separate contributions of the thickened disk (red line) and spherical bulge (green line).

TABLE 3.1: Our Milky Way model

Disk	mass	$M_d = 6.10 \times 10^{10}$ M$_\odot$
	scalelength	$R_d = 3.5$ kpc
	vertical thickness	$z_0 = 350$ pc
	in-plane motion	$Q = 1.2$
	gravity softening	$\epsilon = 70$ pc
Bulge	mass	$M_b = 4.07 \times 10^{10}$ M$_\odot$
	scale radius	$a_b = 0.35$ kpc
Initial halo	mass	$M_h = 73.21 \times 10^{10}$ M$_\odot$
	scale radius	$a_h = 52.5$ kpc

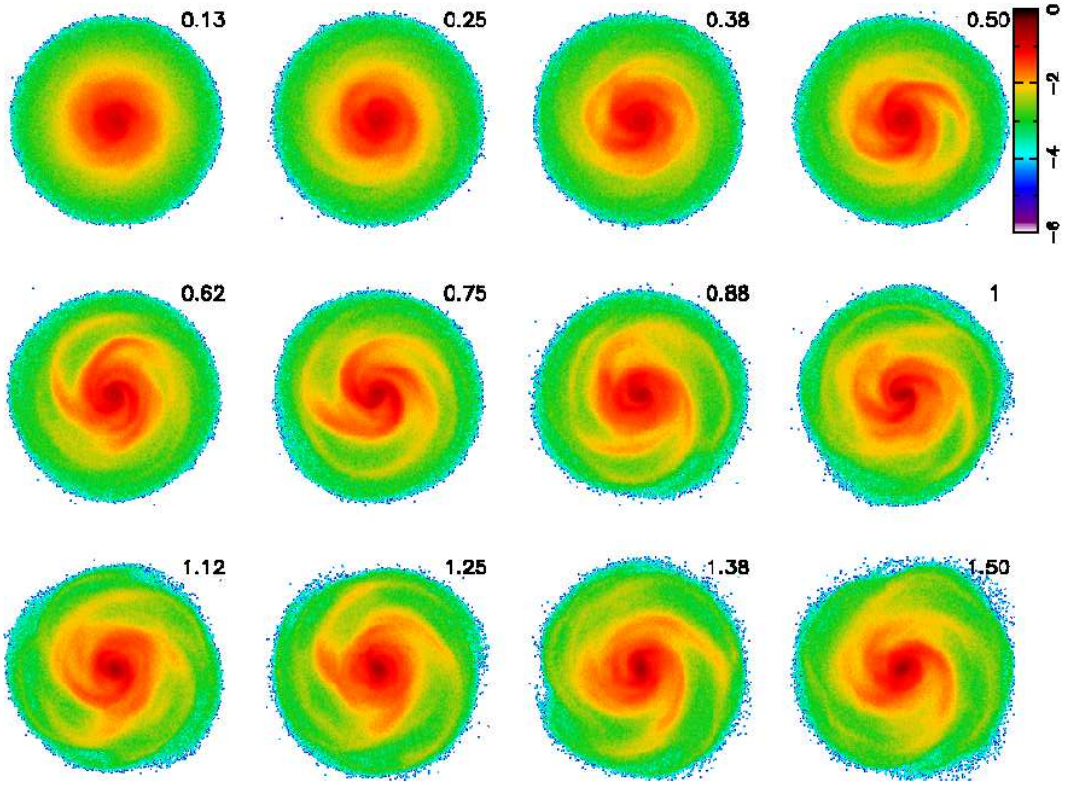

FIGURE 3.12: The first 1.5 Gyr of evolution of a model having no gas particles. The outer radius of the disk in 20 kpc. Notice the strong, open spirals and the absence of a large bar.

3.6.4 Selection of parameters and scaling

Our choices for the parameters of the model are given in Table 3.1 which, after halo compression result in the rotation curve shown in Fig. 3.11.

We can realize this model with any number of particles in each component, and find that it is very close to equilibrium with $T/|W| \simeq 0.504$. Fig. 3.12 illustrates the first 1.5 Gyr of evolution of the disk, which is modeled by 1M star particles and no gas component. The bulge and halo are not shown but are represented by 0.1M and 0.5M particles respectively.

Bibliography

Agertz, O., Teyssier, R. and Moore, B. (2011). The formation of disc galaxies in a ΛCDM universe, **410**(2): 1391–1408.

Balbus, S. A. and Hawley, J. F. (1991). A Powerful Local Shear Instability in Weakly Magnetized Disks. I. Linear Analysis, **376**: 214.

Basu, A. and Roy, S. (2013). Magnetic fields in nearby normal galaxies: energy equipartition, **433**(2): 1675–1686.

Beck, R., Berkhuijsen, E. M., Gießübel, R. and Mulcahy, D. D. (2020). Magnetic fields and cosmic rays in M 31. I. Spectral indices, scale lengths, Faraday rotation, and magnetic field pattern, **633**: A5.

Beck, R., Chamandy, L., Elson, E. and Blackman, E. G. (2019). Synthesizing Observations and Theory to Understand Galactic Magnetic Fields: Progress and Challenges, *Galaxies* **8**(1): 4.

Beck, R. and Wielebinski, R. (2013). Magnetic Fields in Galaxies, *in* T. D. Oswalt and G. Gilmore (eds), *Planets, Stars and Stellar Systems. Volume 5: Galactic Structure and Stellar Populations*, Vol. 5, p. 641.

Bell, A. R. (2004). Turbulent amplification of magnetic field and diffusive shock acceleration of cosmic rays, **353**(2): 550–558.

Berrier, J. C. and Sellwood, J. A. (2015). Smoothing Rotation Curves and Mass Profiles, **799**(2): 213.

Bhat, P., Subramanian, K. and Brandenburg, A. (2016). A unified large/small-scale dynamo in helical turbulence, **461**(1): 240–247.

Bigiel, F., Leroy, A., Walter, F., Brinks, E., de Blok, W. J. G., Madore, B. and Thornley, M. D. (2008). The Star Formation Law in Nearby Galaxies on Sub-Kpc Scales, **136**(6): 2846–2871.

Binney, J. and Tremaine, S. (2008). *Galactic Dynamics: Second Edition.*

Blumenthal, G. R., Faber, S. M., Flores, R. and Primack, J. R. (1986). Contraction of Dark Matter Galactic Halos Due to Baryonic Infall, **301**: 27.

Brandenburg, A. and Subramanian, K. (2005). Astrophysical magnetic fields and nonlinear dynamo theory, **417**(1-4): 1–209.

Butsky, I., Zrake, J., Kim, J.-h., Yang, H.-I. and Abel, T. (2017). Ab Initio Simulations of a Supernova-driven Galactic Dynamo in an Isolated Disk Galaxy, **843**(2): 113.

Chyży, K. T. and Buta, R. J. (2008). Discovery of a Strong Spiral Magnetic Field Crossing the Inner Pseudoring of NGC 4736, **677**(1): L17.

Crutcher, R. M., Wandelt, B., Heiles, C., Falgarone, E. and Troland, T. H. (2010). Magnetic Fields in Interstellar Clouds from Zeeman Observations: Inference of Total Field Strengths by Bayesian Analysis, **725**(1): 466–479.

Dacunha, T., Martin-Alvarez, S., Clark, S. E. and Lopez-Rodriguez, E. (2025). The Fallibility of Equipartition Magnetic Field Strengths from Synchrotron Emission Using Synthetically Observed Galaxies, **980**(2): 197.

Daniel, K. J. and Wyse, R. F. G. (2018). Constraints on radial migration in spiral galaxies - II. Angular momentum distribution and preferential migration, **476**(2): 1561–1580.

Elmegreen, B. G. and Elmegreen, D. M. (1986). Do Density Waves Trigger Star Formation?, **311**: 554.

Evans, C. R. and Hawley, J. F. (1988). Simulation of Magnetohydrodynamic Flows: A Constrained Transport Model, **332**: 659.

Federrath, C., Chabrier, G., Schober, J., Banerjee, R., Klessen, R. S. and Schleicher, D. R. G. (2011). Mach Number Dependence of Turbulent Magnetic Field Amplification: Solenoidal versus Compressive Flows, **107**(11): 114504.

Ferland, G. J., Chatzikos, M., Guzmán, F., Lykins, M. L., van Hoof, P. A. M., Williams, R. J. R., Abel, N. P., Badnell, N. R., Keenan, F. P., Porter, R. L. and Stancil, P. C. (2017). The 2017 Release Cloudy, **53**: 385–438.

Fletcher, A., Beck, R., Shukurov, A., Berkhuijsen, E. M. and Horellou, C. (2011). Magnetic fields and spiral arms in the galaxy M51, **412**(4): 2396–2416.

Frankel, N., Sanders, J., Ting, Y.-S. and Rix, H.-W. (2020). Keeping It Cool: Much Orbit Migration, yet Little Heating, in the Galactic Disk, **896**(1): 15.

Frick, P., Stepanov, R., Beck, R., Sokoloff, D., Shukurov, A., Ehle, M. and Lundgren, A. (2016). Magnetic and gaseous spiral arms in M83, **585**: A21.

Geach, J. E., Lopez-Rodriguez, E., Doherty, M. J., Chen, J., Ivison, R. J., Bendo, G. J., Dye, S. and Coppin, K. E. K. (2023). Polarized thermal emission from dust in a galaxy at redshift 2.6, *arXiv e-prints* p. arXiv:2309.02034.

Goldsmith, P. F., Heyer, M., Narayanan, G., Snell, R., Li, D. and Brunt, C. (2008). Large-Scale Structure of the Molecular Gas in Taurus Revealed by High Linear Dynamic Range Spectral Line Mapping, **680**(1): 428–445.

Gressel, O., Elstner, D. and Ziegler, U. (2013). Towards a hybrid dynamo model for the Milky Way, **560**: A93.

Henriksen, R. N. (2017). Magnetic spiral arms in galaxy haloes, **469**(4): 4806–4830.

Hernquist, L. (1990). An Analytical Model for Spherical Galaxies and Bulges, **356**: 359.

Hockney, R. W. and Eastwood, J. W. (1981). *Computer Simulation Using Particles*.

Joung, M. K. R. and Mac Low, M.-M. (2006). Turbulent Structure of a Stratified Supernova-driven Interstellar Medium, **653**(2): 1266–1279.

Keller, B. W., Wadsley, J., Benincasa, S. M. and Couchman, H. M. P. (2014). A superbubble feedback model for galaxy simulations, **442**(4): 3013–3025.

Khoperskov, S. A. and Khrapov, S. S. (2018). Global enhancement and structure formation of the magnetic field in spiral galaxies, **609**: A104.

Kim, C.-G., Kim, W.-T. and Ostriker, E. C. (2006). Interstellar Turbulence Driving by Galactic Spiral Shocks, **649**(1): L13–L16.

Kim, J.-h., Abel, T., Agertz, O., Bryan, G. L., Ceverino, D., Christensen, C., Conroy, C., Dekel, A., Gnedin, N. Y., Goldbaum, N. J., Guedes, J., Hahn, O., Hobbs, A., Hopkins, P. F., Hummels, C. B., Iannuzzi, F., Keres, D., Klypin, A., Kravtsov, A. V., Krumholz, M. R., Kuhlen, M., Leitner, S. N., Madau, P., Mayer, L., Moody, C. E., Nagamine, K., Norman, M. L., Onorbe, J., O'Shea, B. W., Pillepich, A., Primack,

J. R., Quinn, T., Read, J. I., Robertson, B. E., Rocha, M., Rudd, D. H., Shen, S., Smith, B. D., Szalay, A. S., Teyssier, R., Thompson, R., Todoroki, K., Turk, M. J., Wadsley, J. W., Wise, J. H., Zolotov, A. and AGORA Collaboration29, t. (2014). The AGORA High-resolution Galaxy Simulations Comparison Project, **210**(1): 14.

Kim, W.-T., Kim, C.-G. and Ostriker, E. C. (2020). Local Simulations of Spiral Galaxies with the TIGRESS Framework. I. Star Formation and Arm Spurs/Feathers, **898**(1): 35.

Korpi, M. J., Käpylä, P. J. and Väisälä, M. S. (2010). Influence of Ohmic diffusion on the excitation and dynamics of MRI, *Astronomische Nachrichten* **331**(1): 34.

Krumholz, M. R., Burkhart, B., Forbes, J. C. and Crocker, R. M. (2018). A unified model for galactic discs: star formation, turbulence driving, and mass transport, **477**(2): 2716–2740.

Ledos, N., Ntormousi, E., Takasao, S. and Nagamine, K. (2024). Magnetising galaxies with cold inflows, **691**: A280.

Liu, Y., Kretschmer, M. and Teyssier, R. (2022). A subgrid turbulent mean-field dynamo model for cosmological galaxy formation simulations, **513**(4): 6028–6041.

Lopez-Rodriguez, E., Borlaff, A. S., Beck, R., Reach, W. T., Mao, S. A., Ntormousi, E., Tassis, K., Martin-Alvarez, S., Clark, S. E., Dale, D. A. and del Moral-Castro, I. (2023). Extragalactic Magnetism with SOFIA (SALSA Legacy Program): The Magnetic Fields in the Multiphase Interstellar Medium of the Antennae Galaxies, **942**(1): L13.

Lovelace, R. V. E. and Hohlfeld, R. G. (1978). Negative mass instability of flat galaxies., **221**: 51–61.

Martin-Alvarez, S., Devriendt, J., Slyz, A., Sijacki, D., Richardson, M. L. A. and Katz, H. (2022). Towards convergence of turbulent dynamo amplification in cosmological simulations of galaxies, **513**(3): 3326–3344.

Martin-Alvarez, S., Lopez-Rodriguez, E., Dacunha, T., Clark, S. E., Borlaff, A. S., Beck, R., Rodríguez Montero, F., Jung, S. L., Devriendt, J., Slyz, A., Roman-Duval, J. C., Ntormousi, E., Tahani, M., Subramanian, K., Dale, D. A., Marcum, P. M., Tassis, K., del Moral-Castro, I., Tram, L. N. and Jarvis, M. J. (2024). Extragalactic Magnetism with SOFIA (SALSA Legacy Program). VII. A Tomographic View of Far-infrared and Radio Polarimetric Observations through MHD Simulations of Galaxies, **966**(1): 43.

Ntormousi, E., Tassis, K., Del Sordo, F., Fragkoudi, F. and Pakmor, R. (2020). A dynamo amplifying the magnetic field of a Milky-Way-like galaxy, **641**: A165.

Pakmor, R., van de Voort, F., Bieri, R., Gómez, F. A., Grand, R. J. J., Guillet, T., Marinacci, F., Pfrommer, C., Simpson, C. M. and Springel, V. (2020). Magnetizing the circumgalactic medium of disc galaxies, **498**(3): 3125–3137.

Parker, E. N. (1955). Hydromagnetic Dynamo Models., **122**: 293.

Pfrommer, C., Werhahn, M., Pakmor, R., Girichidis, P. and Simpson, C. M. (2022). Simulating radio synchrotron emission in star-forming galaxies: small-scale magnetic dynamo and the origin of the far-infrared-radio correlation, **515**(3): 4229–4264.

Planck Collaboration (2016). Planck intermediate results. XXXV. Probing the role of the magnetic field in the formation of structure in molecular clouds, **586**: A138.

Ponnada, S. B., Panopoulou, G. V., Butsky, I. S., Hopkins, P. F., Loebman, S. R., Hummels, C., Ji, S., Wetzel, A., Faucher-Giguère, C.-A. and Hayward, C. C. (2022). Magnetic fields on FIRE: Comparing B-fields in the multiphase ISM and CGM of simulated L_* galaxies to observations, **516**(3): 4417–4431.

Pudritz, R. E. and Silk, J. (1989). The Origin of Magnetic Fields and Primordial Stars in Protogalaxies, **342**: 650.

Querejeta, M., Leroy, A. K., Meidt, S. E., Schinnerer, E., Belfiore, F., Emsellem, E., Klessen, R. S., Sun, J., Sormani, M., Bešlić, I., Cao, Y., Chevance, M., Colombo, D., Dale, D. A., García-Burillo, S., Glover, S. C. O., Grasha, K., Groves, B., Koch, E. W., Neumann, L., Pan, H.-A., Pessa, I., Pety, J., Pinna, F., Ramambason, L., Razza, A., Romanelli, A., Rosolowsky, E., Ruiz-García, M., Sánchez-Blázquez, P., Smith, R., Stuber, S., Ubeda, L., Usero, A. and Williams, T. G. (2024). Do spiral arms enhance star formation efficiency?, **687**: A293.

Rieder, M. and Teyssier, R. (2016). A small-scale dynamo in feedback-dominated galaxies as the origin of cosmic magnetic fields - I. The kinematic phase, **457**(2): 1722–1738.

Rieder, M. and Teyssier, R. (2017). A small-scale dynamo in feedback-dominated galaxies - II. The saturation phase and the final magnetic configuration, **471**(3): 2674–2686.

Riquelme, M. A. and Spitkovsky, A. (2009). Nonlinear Study of Bell's Cosmic Ray Current-Driven Instability, **694**(1): 626–642.

Robinson, H. and Wadsley, J. (2024). Regulating star formation in a magnetized disk galaxy, .

Roškar, R., Debattista, V. P., Quinn, T. R., Stinson, G. S. and Wadsley, J. (2008). Riding the Spiral Waves: Implications of Stellar Migration for the Properties of Galactic Disks, **684**(2): L79.

Sellwood, J. A. (2024). Particle selection from an equilibrium DF, **529**(3): 3035–3043.

Sellwood, J. A. and Balbus, S. A. (1999). Differential Rotation and Turbulence in Extended H I Disks, **511**(2): 660–665.

Sellwood, J. A. and Binney, J. J. (2002). Radial mixing in galactic discs, **336**(3): 785–796.

Sellwood, J. A. and Masters, K. L. (2022). Spirals in Galaxies, **60**.

Sellwood, J. A. and McGaugh, S. S. (2005). The Compression of Dark Matter Halos by Baryonic Infall, **634**(1): 70–76.

Semenov, V. A., Kravtsov, A. V. and Caprioli, D. (2021). Cosmic-Ray Diffusion Suppression in Star-forming Regions Inhibits Clump Formation in Gas-rich Galaxies, **910**(2): 126.

Shukurov, A., Rodrigues, L. F. S., Bushby, P. J., Hollins, J. and Rachen, J. P. (2019). A physical approach to modelling large-scale galactic magnetic fields, **623**: A113.

Smith, B. D., Bryan, G. L., Glover, S. C. O., Goldbaum, N. J., Turk, M. J., Regan, J., Wise, J. H., Schive, H.-Y., Abel, T., Emerick, A., O'Shea, B. W., Anninos, P., Hummels, C. B. and Khochfar, S. (2017). GRACKLE: a chemistry and cooling library for astrophysics, **466**(2): 2217–2234.

Steinwandel, U. P., Dolag, K., Lesch, H., Moster, B. P., Burkert, A. and Prieto, A. (2020). On the origin of magnetic driven winds and the structure of the galactic dynamo in isolated galaxies, **494**(3): 4393–4412.

Stix, M. (1975). The galactic dynamo., **42**(1): 85–89.

Su, K.-Y., Hayward, C. C., Hopkins, P. F., Quataert, E., Faucher-Giguère, C.-A. and Kereš, D. (2018). Stellar feedback strongly alters the amplification and morphology of galactic magnetic fields, **473**(1): L111–L115.

Sun, B., Calzetti, D. and Battisti, A. J. (2024). The Role of Spiral Arms in Galaxies, **973**(2): 137.

Teyssier, R. (2002). Cosmological hydrodynamics with adaptive mesh refinement. A new high resolution code called RAMSES, **385**: 337–364.

Toomre, A. (1964). On the gravitational stability of a disk of stars., **139**: 1217–1238.

Whitworth, D. J., Srinivasan, S., Pudritz, R. E., Mac Low, M. M., Eadie, G., Palau, A., Soler, J. D., Smith, R. J., Pattle, K., Robinson, H., Pillsworth, R., Wadsley, J., Brucy, N., Lebreuilly, U., Hennebelle, P., Girichidis, P., Gent, F. A., Marin, J., Sánchez Valido, L., Camacho, V., Klessen, R. S. and Vázquez-Semadeni, E. (2025). On the relation between magnetic field strength and gas density in the interstellar medium: a multiscale analysis, **540**(3): 2762–2786.

Wibking, B. D. and Krumholz, M. R. (2023). The global structure of magnetic fields and gas in simulated Milky Way-analogue galaxies, **521**(4): 5972–5990.

Wissing, R. and Shen, S. (2023). Numerical dependencies of the galactic dynamo in isolated galaxies with SPH, **673**: A47.

Young, P. (1980). Numerical models of star clusters with a central black hole. I - Adiabatic models., **242**: 1232–1237.

Zhao, B., Pudritz, R. E., Pillsworth, R., Robinson, H. and Wadsley, J. (2024). Filamentary Hierarchies and Superbubbles: Galactic Multiscale Magnetohydrodynamic Simulations of Giant Molecular Cloud to Star Cluster Formation, **974**(2): 240.

Zhao, M., Zhou, J., Baan, W. A., Hu, Y., Lazarian, A., Tang, X., Esimbek, J., He, Y., Li, D., Ji, W., Chang, Z. and Tursun, K. (2024). Magnetic Field of Molecular Gas Measured with the Velocity Gradient Technique. II. Curved Magnetic Field in kpc-scale Bubble of NGC 628, **967**(1): 18.

Chapter 4

The Effects of Initial Field Morphology on Isolated Galaxy Simulations

Abstract

Magnetic fields are importa nt in galactic evolution, and numerical simulations are one of the primary methods used to test them. In this work, we investigate the influence of initial magnetic field configurations on the evolution of isolated disk galaxies using magnetohydrodynamic (MHD) simulations. Three initial geometries are considered: uniform, dipolar, and toroidal. We find that while the dipole and uniform cases evolve toward similar magnetic saturation levels, the toroidal case leads to the spontaneous development of a central bar with stronger fields. This bar-driven inflows promote centralized star-formation which enhances dynamo action in the central few kiloparsecs. The final fields in the toroidal galaxy also reflect the direction they are initialized in, with fewer field reversals within the disk. All three models produce magnetic spirals with pitch angle distributions peaking near 10 degrees, but the toroidal model produces slightly lower pitch angles. Our study demonstrates that formation of bars is sensitive to the morphology of magnetic fields, either due to azimuthal fields suppressing radial transport, or vertical fields enabling it through magnetic braking.

Keywords: *Methods: numerical – MHD – ISM: magnetic fields*

4.1 Introduction

Magnetic fields are an important component of galaxies, particularly on the scale of the Interstellar Medium (ISM). The fields within present-day galaxies are the product of billions of years of evolution acting on primordial seed fields. Their influence depends not only on their strength and amplification processes, but also on their spatial configuration. Our previous simulation work has explored the growth and regulation of magnetic fields in late disk galaxies (Robinson and Wadsley; 2024; Robinson et al.; 2025), but all used similar geometries for the initial magnetic field. It is of interest whether the fields generated in those simulations always a natural outcome, or to what extent bias was introduced by the setup. Understanding whether different initial geometries lead to qualitatively distinct galactic outcomes is therefore a natural step in assessing the robustness of MHD galaxy model predictions.

There are several different approaches for designing the initial fields in simulations. In cosmological simulations, the initial setup is relatively straightforward: very weak ($B \sim 10^{-20}$ G) seed fields pointing uniformly in one direction(Rieder and Teyssier; 2017b). The subsequent billions of years of amplification by the small-scale dynamo erase any memory of the original seed fields. Isolated galaxy simulations begin in an already evolved state, and can therefore have more complicated field setups. Some commonly used choices include uniform fields, (Steinwandel et al.; 2020; Wissing and Shen; 2023) toroidal fields (Körtgen et al.; 2019; Ntormousi et al.; 2020; Wissing and Shen; 2023; Wibking and Krumholz; 2023), dipole fields (Rieder and Teyssier; 2017a; Ntormousi; 2018), quadrupole fields (Rieder and Teyssier; 2016; Ntormousi; 2018), or some combination of those. Approaches that begin with zero magnetic fields but inject them during feedback have also been employed (Butsky et al.; 2017; Steinwandel et al.; 2020). Another option is to use random seed fields, but those are more often employed in local shearing-box or cloud-scale simulations (Heitsch et al.; 2009; Mocz et al.; 2017) where the focus is on turbulent dynamo growth, and they are not typically adopted for full isolated galaxy disks. A constraint in designing the field configuration is maintaining the divergence-free condition, ($\nabla \cdot \vec{B} = 0$) while ensuring numerical stability; this is one reason why relatively simple morphologies remain most commonly used.

A general rule of thumb when initializing fields is to start as weak as possible. Turbulent dynamos will amplify the fields naturally, and beginning from a state of weak fields will ensure they converge towards a realistic saturated state. However, in isolated galaxies an important consideration is timescale. These types of simulation are

often limited to ∼1 Gyr of evolution due to the finite gas supply; after this point, the ISM is no longer in a self-regulated steady state. Because of the limitations in time, it is desirable for the fields reach their saturated state relatively quickly. If the weak field persists on timescales comparable to 1 Gyr, the effect of the magnetic fields within galaxy may not be felt until late into its evolution. This has motivated some groups to start with field strengths reflecting a saturated, or near-saturated state (Körtgen et al.; 2019). The risk of this approach is that fields that are too strong may bias the results, especially in ideal-MHD simulations where there is no way for excess magnetic energy to be dissipated (Robinson and Wadsley; 2024). These design choices are especially important when testing large-scale dynamo action. These dynamos have slow growth rates (e-folding time hundreds of Myr to a few Gyr) which is comparable to the total runtime of the simulations (Brandenburg and Subramanian; 2005).

Observations provide valuable clues about the morphology of the saturated state of galactic magnetic fields. The observations therefore provide us with a final state to compare against, and it would be valuable to show, via simulations, that we can produce them from a variety of reasonable initial states. Radio polarization mapping often reveals ordered magnetic spirals in disk galaxies, but these organized fields frequently align more closely with inter-arm regions than with optical arms. In cases like NGC 6946 and IC 342, distinct "magnetic arms" emerge with high polarization fractions, likely driven by dynamo-generated anisotropies (Frick et al.; 2000; Beck; 2015b; Weżgowiec et al.; 2016). Studies of M31 and IC 342 have also uncovered large-scale field reversals and helical flux loops, features associated with Parker instability and complex dynamo behavior (Beck et al.; 2020). In edge-on galaxies, X-shaped halo fields are ubiquitous, suggesting structured outflows or large-scale dynamo modes shaping field topology. Polarization stacking of 28 nearby spiral galaxies confirms X-shaped morphologies are a widespread feature (Krause et al.; 2020; Stein et al.; 2025).

Another reason to consider magnetic morphologies lies in their impact on angular momentum transport within galactic disks. Magnetic fields exert stresses through their tension and pressure, captured in the Maxwell stress tensor, that can redistribute angular momentum both radially and vertically (Balbus and Hawley; 1998; Parker; 1979). In practice, the most important component is the $T_{r\phi}$ stress, which links radial and azimuthal field components (Hawley et al.; 1995; Kulsrud; 2005). Configurations with strong toroidal fields tend to enhance angular momentum exchange within the disk plane, thereby influencing the stability of bars and spiral arms (Machida et al.; 2013). Vertical components, on the other hand, can provide vertical coupling between the disk and its

surrounding halo, enabling angular momentum to be extracted through a process known as magnetic braking. (Beck; 2015b; Pakmor et al.; 2020). In this way, the morphology of the field is not just a technical detail of the setup, but a factor that can shape disk structure, thickness, and long-term evolution.

Some simulations have studied the effectiveness of magnetic fields in transporting angular momentum. Whittingham et al. (2023) studied this in the context of cosmological MHD galaxy mergers, and found the transport of angular momentum by the fields suppressed the formation of bars. Martin-Alvarez et al. (2020) studied magnetic braking in galactic disks and found it to be capable of altering the sizes of young galactic disks.Kim and Stone (2012) found that the inclusion of magnetic fields increased the mass-inflow rates within already existing bars. These studies have highlighted that the morphology of magnetic fields can subsequently effect the morphology of their host galaxy.

In this work we investigate whether the morphology of the initial magnetic field can lead to qualitatively distinct galactic behaviors, or whether memory of the initial geometry is erased by subsequent evolution. By comparing simulations initialized with different configurations, we aim to clarify how sensitive galaxy-scale angular momentum transport and magnetic support are to their initial conditions, with possible knock-on effects on ISM structure and star formation regulation. The remainder of this paper is organized as follows: In Section 4.2 we describe our numerical methods and simulation setup, in Section 4.3.1 we present the results of the simulations, in Section 4.4 we make conclusions and discuss the implications.

4.2 Methods

Our simulations largely follow the methodology described in Robinson and Wadsley (2024) and Robinson et al. (2025). We use the adaptive mesh refinement (AMR) code Ramses (Teyssier; 2002) to solve the ideal magnetohydrodynamic (MHD) equations with an HLLD approximate Riemann solver (Miyoshi and Kusano; 2005). Ramses enforces $\nabla \cdot \mathbf{B} = 0$ via the constrained transport method (Evans and Hawley; 1988). The gravitational dynamics of stars and dark matter are solved using a particle-mesh approach (Hockney and Eastwood; 1981), and gas cooling and photoelectric heating are included through the Grackle chemistry and cooling library (Smith et al.; 2017). Star formation and supernova feedback follow the stochastic Schmidt-law and delayed-cooling prescription of Agertz et al. (2011).

The galaxy models are based on the spiral galaxy from Robinson et al. (2025) with a dark matter halo, stellar bulge, and mixed gas-plus-stellar disk . The AMR grid allows for a maximum spatial resolution of 9.15 pc. Each galaxy is evolved for 1 Gyr, long enough to reach a quasi-steady state of self-regulated star formation before gas depletion begins to dominate.

4.2.1 Initial Field Configuration

The main variable we test in this work is the initialization of the magnetic field. We simulate three different magnetic field morphologies: uniform, toroidal, and dipolar. The toroidal model is exactly the spiral galaxy from Robinson et al. (2025), with fields given by

$$\vec{B} = B_0 \frac{\rho(r,z)}{\rho_0} \hat{e_\phi} \tag{4.1}$$

here $\hat{e_\phi}$ is the unit vector in the azimuthal direction, B_0=0.85 μG, and $\rho_0 = 1.15 \times 10^{-23}$ g cm^{-3}. The uniform field is of the form

$$\vec{B} = \begin{pmatrix} 0 \ \hat{x} \\ 0 \ \hat{y} \\ 0.01 \ \mu\text{G} \ \hat{z} \end{pmatrix} \tag{4.2}$$

Note that the uniform field does not have any scaling with ρ, meaning the plasma beta ($\beta = P_{\text{thermal}}/P_{\text{mag}}$) varies greatly in different density regions. However, we have chosen a relatively weak field strength to avoid large values of β above the disk. The dipole field is defined using a vector potential

$$\vec{A} = B_0 \left(\frac{\rho}{\rho_0}\right)^{2/3} \vec{r} \ \hat{e_\phi} \tag{4.3}$$

The field is then attained by $\vec{B} = \vec{\nabla} \times \vec{A}$. The dipole field has both a vertical and radial component, being primarily vertical near the disk midplane and bending radially above the disk. We note that the dipole field only has an approximate $\rho^{2/3}$ scaling; due to the r dependence it has weaker fields in the central region and stronger fields in the outer disk, compared to the toroidal model. All of the initial fields are visualized in Figures 4.1 and 4.2, face-on and edge-on respectively.

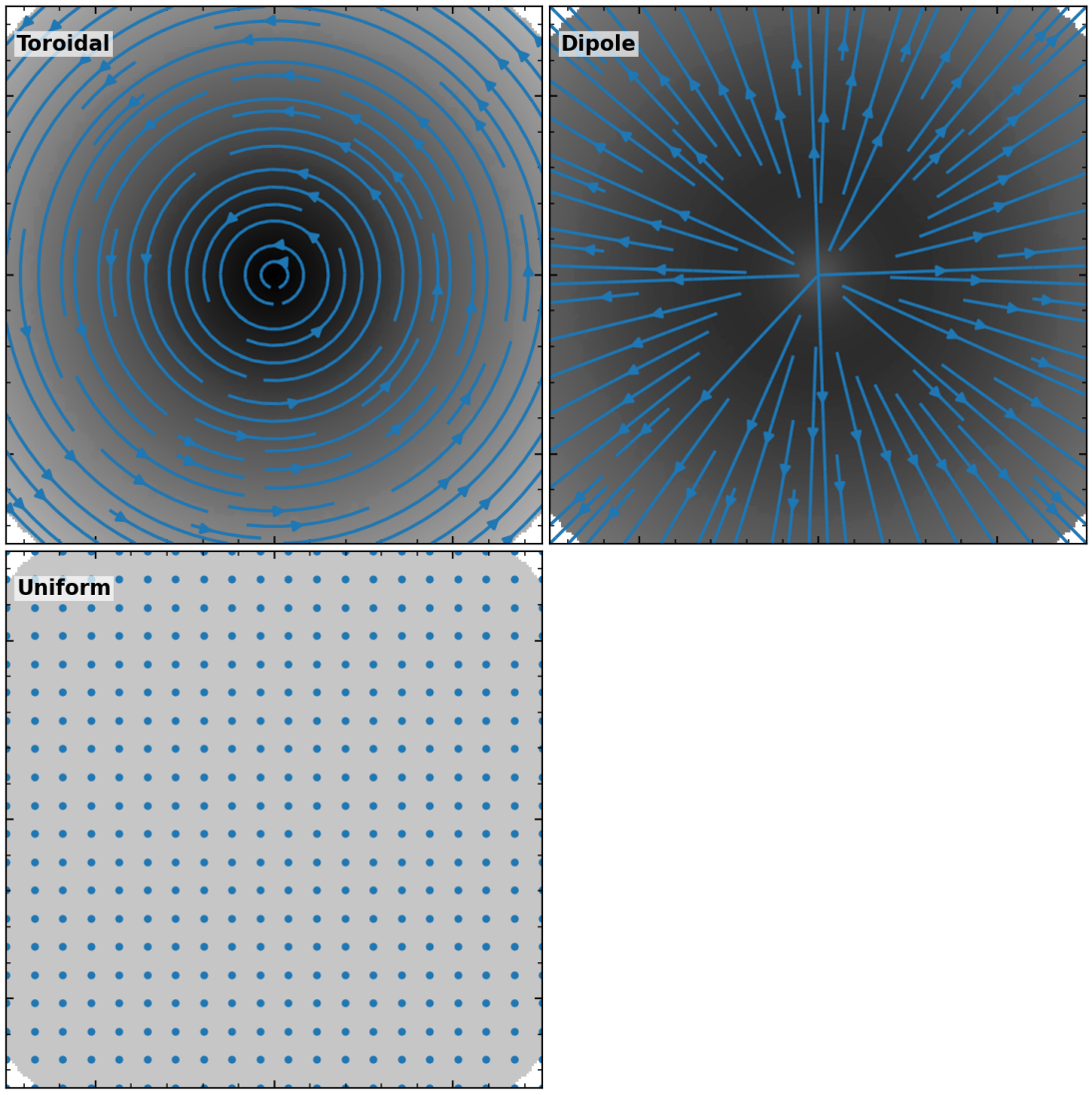

FIGURE 4.1: Visualizations of the initial magnetic field in the x-y plane (face-on). Background colour is scaled by the logarithm of the magnetic field strength. The uniform model has no fields in the x-y plane, so the dots represent field lines into the page.

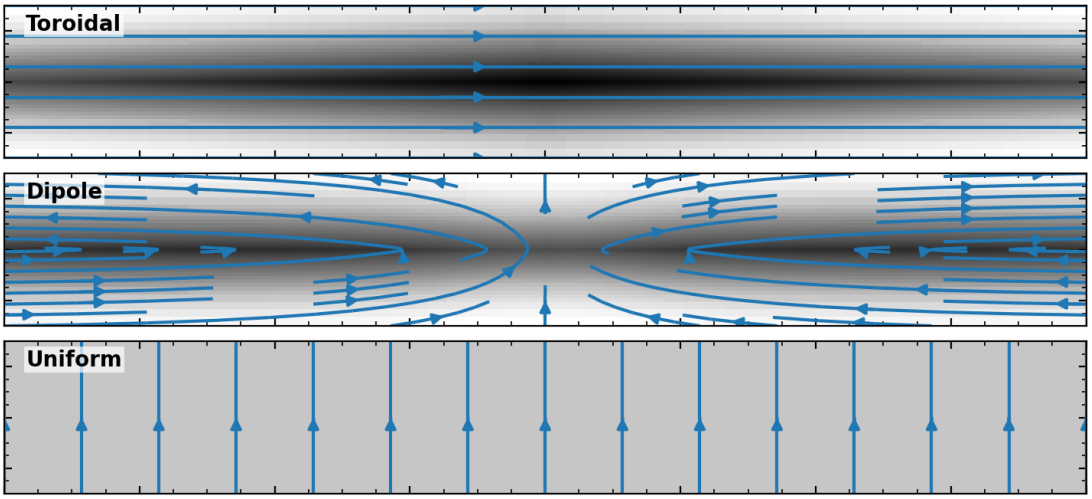

FIGURE 4.2: Visualizations of the initial magnetic field in the x-z plane (edge-on). Background colour is scaled by the logarithm of the magnetic field strength.

4.3 Simulation Results

4.3.1 Evolution and Bar Formation

All three galaxies begin their evolution with an initial starburst, followed by a more quiescent phase. Initially, the evolution of each galaxy appears quite similar, but major differences begin to appear at t=500 Myr. At this time, the toroidal model develops a strong central bar in both the stars and gas, but the uniform and dipole galaxies do not. This can be seen in Figures 4.3 and 4.4, which show projections of each galaxy's stellar surface density, star formation rate (SFR), gas surface density, and magnetic field strength at t=0.4 Gyr and t=1 Gyr respectively. We choose these times to visualize the galaxies before and after the formation of the bar. After 1 Gyr, the toroidal galaxy has high surface densities of gas in the central region, which results in the star formation becoming centrally concentrated. At this time the bar is visible in the stellar and gas surface densities. Due to the transient nature of the spiral arms, the spiral structure is different in the two snapshots, having more of a grand design (m=2) at t=1 Gyr. The toroidal galaxy hosts stronger magnetic fields throughout the disk, seen in the bottom row.

Figure 4.5 shows the star formation history of each galaxy. In each galaxy, star formation peaks at 10 $M_\odot$/yr at t=100 Myr, followed by a gradual decline reaching 1

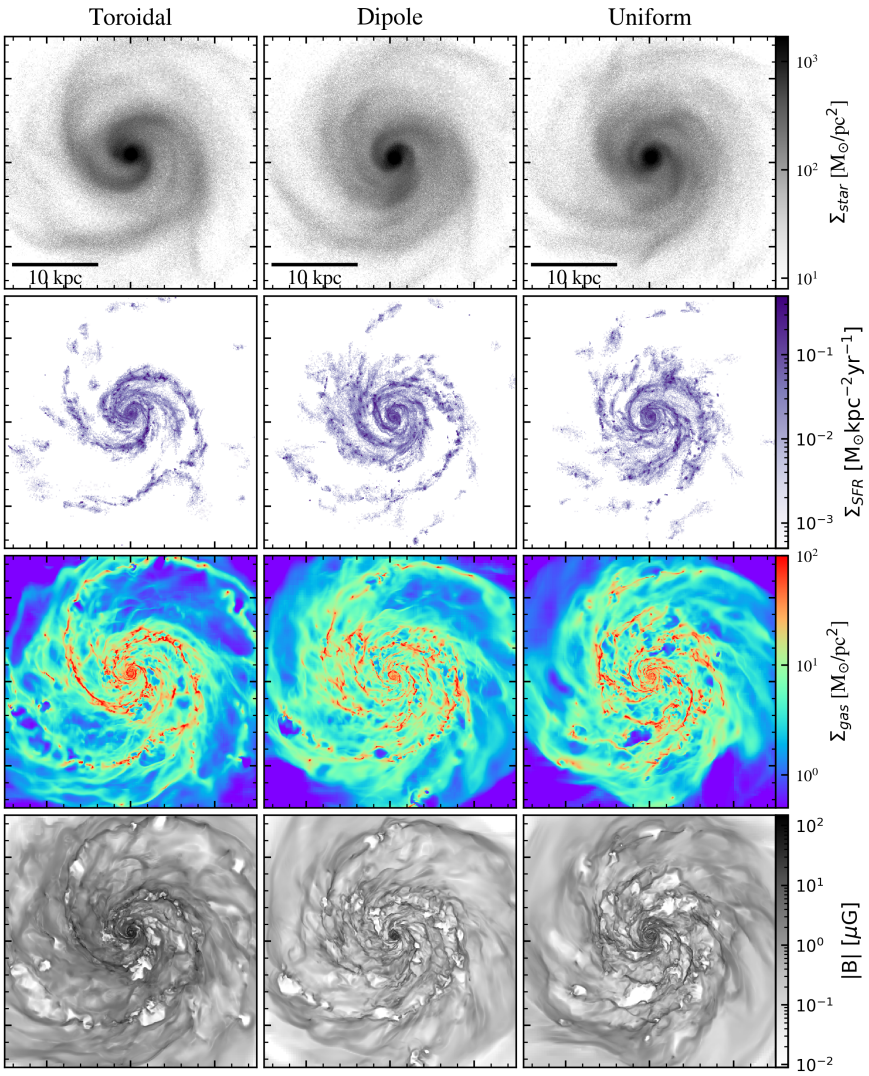

FIGURE 4.3: Visualizations of stellar surface density (top row), star formation rate surface density (second row), gas surface density (third row), and mass-weighted magnetic field strength (bottom row) for each galaxy at t=400 Myr. Gas surface density and magnetic field strength are calculated using gas within 1 kpc of the midplane. SFR is calculated using all star particles that formed during the previous 100 Myr.

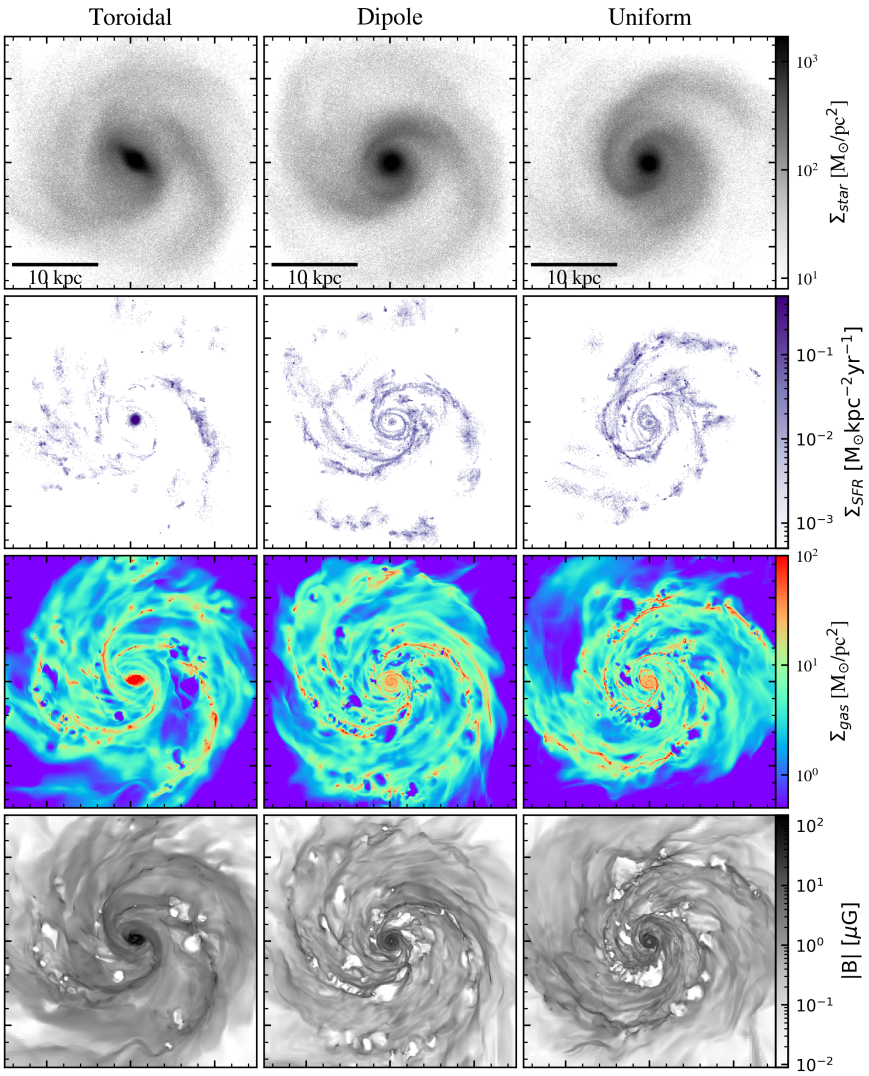

FIGURE 4.4: Visualizations of stellar surface density (top row), star formation rate surface density (second row), gas surface density (third row), and mass-weighted magnetic field strength (bottom row) for each galaxy at t=1 Gyr. Gas surface density and magnetic field strength are calculated using gas within 1 kpc of the midplane. SFR is calculated using all star particles that formed during the previous 100 Myr.

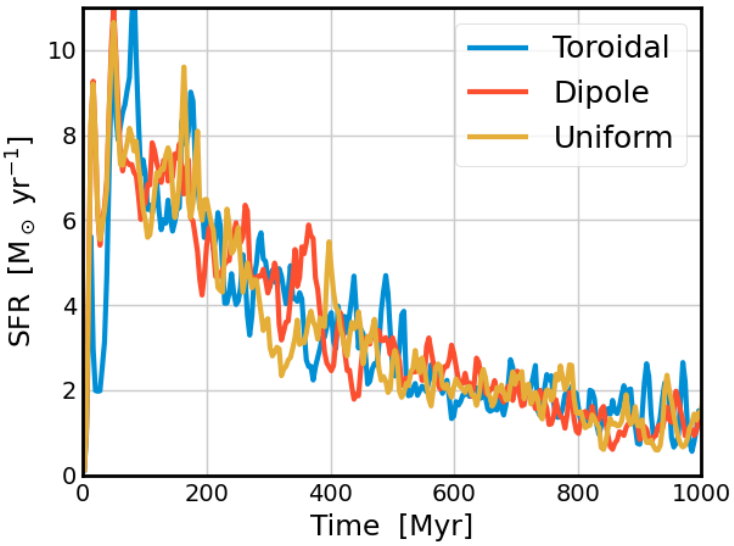

FIGURE 4.5: Total SFR for each galaxy. SFR is calculated by summing the mass of stars formed in each time bin and dividing by the bin size. Despite the differences in the distribution of star formation, the total SFR history in each galaxy remains similar.

$M_\odot$/yr at t=1000 Myr. The star formation histories show regular bursty fluctuations in all three galaxies, but the underlying trends do not vary significantly among the galaxies, despite the differences in the distribution of star formation.

To further inspect the distribution of gas density and magnetic fields, we plot the radial profiles of each throughout the 1 Gyr of evolution in Figure 4.6. The top row shows the surface density of gas vs. radius. In the dipole and uniform galaxy, the surface density steadily declines in the central 10 kpc of the disk as gas is converted into stars. In the toroidal galaxy, differences in the gas surface density profile begin to appear at t=450 Myr. Afterwards, the gas becomes increasingly centrally concentrated, reaching surface densities of 100 $M_\odot/pc^2$ in the center at t=1 Gyr. The value is the same as the t=0 gas surface density, despite the highest gas consumption occurring in this region. This suggests the bar is driving inflows of gas into the galactic center.

The second, third and fourth rows of Figure 4.6 shows the radial profile volume-averaged absolute value of radial, azimuthal and vertical field components respectively. We examine the absolute values of the field to determine the relative importance of each component, and leave the analysis of field reversals to section 4.3.3. In the toroidal galaxy, the azimuthal component of the field is the strongest, reaching strengths of 1

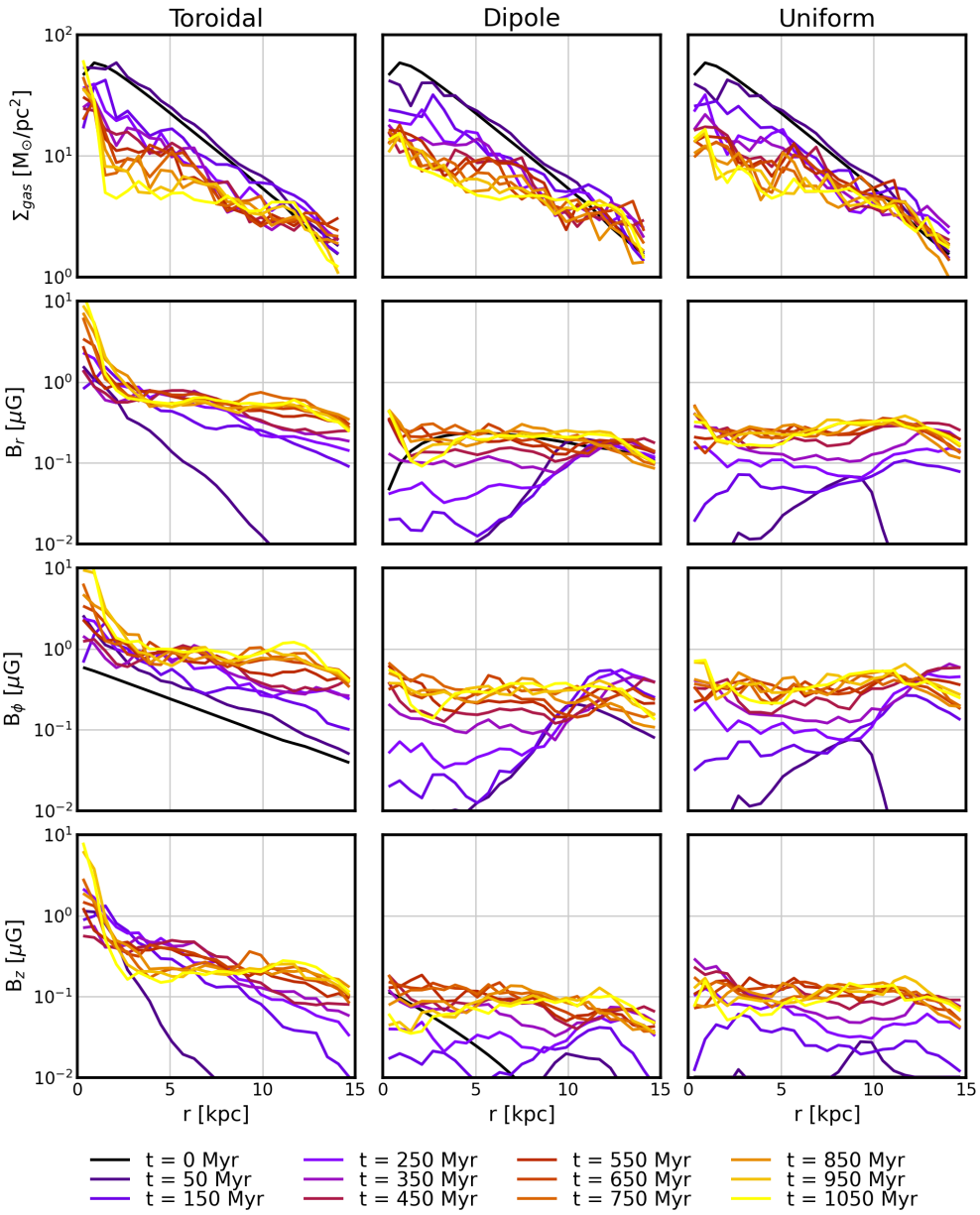

FIGURE 4.6: Radial profiles of gas surface density (top row), radial magnetic field strength (second row), azimuthal magnetic field strength (third row), and vertical magnetic field strength (bottom row). Magnetic field values are calculated using a volume-weighted average of the absolute values of all cells within 1 kpc of the disk midplane. This does not show field reversals, but the overall strength of each component.

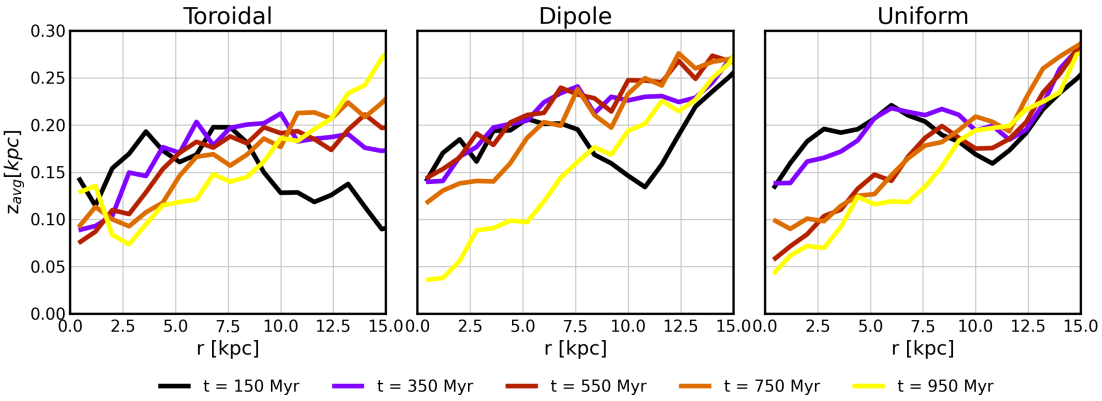

FIGURE 4.7: Radial profiles of the mass-weighted average $|z|$ value of all gas in each galaxy at 5 times.

μG throughout the disk, followed by the radial component which reaches strengths of 0.8 μG, and the vertical field saturates at ~ 0.2 μG. In the dipole and uniform galaxies, the radial and azimuthal component are similar, both reaching values of ~ 0.5 μG. The toroidal galaxy also shows strong magnetic field growth in the central 2 kpc, reaching strengths of ~ 10 μG by the end of the simulation. The toroidal galaxy has consistently stronger fields throughout the disk than the other two galaxies, which shows the initial conditions have changed the final saturated state of the fields, as well as the development of a bar.

We now examine the thickness of the gas disk. Figure 4.7 shows the mass-weighted average |z| of gas cells vs radius each galaxy, which we use as a measure of disk thickness, as in Robinson and Wadsley (2024). At t=950 Myr, all three models have similar thickness profiles, with the exception of the central 3 kpc of the toroidal model, where the strong feedback in the central region has thickened the gas disk. At earlier times there are more significant differences between the galaxies. Before 550 Myr, the toroidal galaxy has the thinnest disk in the inner 3 kpc. Here the toroidal galaxy has a thickness of 100 pc, compared to the other two cases which have thicknesses of 150 pc. This may aid in the development of the bar because thinner disks are more unstable to bar instabilities (Ghosh et al.; 2023). However, this is likely not the only reason it formed a bar, because the dipole and uniform galaxies end up with final thicknesses of 50 pc in the central 2.5 kpc, and yet do not form a bar. There are also differences between the uniform and dipole galaxies in the final 500 Myr. The uniform galaxy reaches its final thickness profile by t= 550 Myr, while the dipole galaxy does not until 950 Myr.

To further examine the development of the bar, we plot the surface density profiles

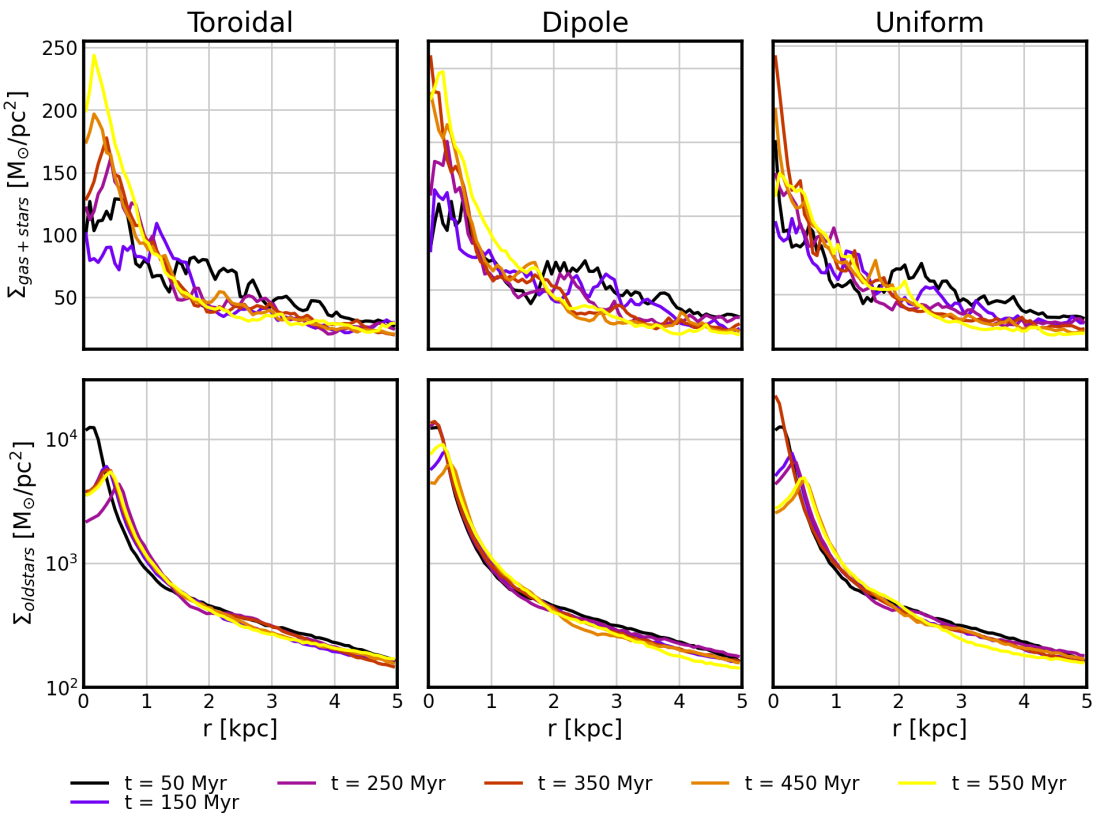

FIGURE 4.8: Radial profile of surface density before gas and newly formed stars (top row), and stars in the initial stellar disk (bottom row) in the central 5 kpc during the development of the bar.

within the central 5 kpc of the disk before the development of the bar, for both gas plus newly formed stars, and stars from the initial stellar disk. At t=350 Myr, the gas distributions of the dipole and uniform galaxies are centrally peaked, reaching surface densities of 200 and 250 $M_\odot/pc^2$ respectively. In contrast, the toroidal galaxy has central surface densities of 125 $M_\odot/pc^2$, and it peaks at r=0.5 kpc with a surface density of 175 $M_\odot/pc^2$. While these differences may seem subtle, they are consistent with results from Whittingham et al. (2023), which shows similar increases in central concentrations stabilizing against bar formation in MHD galaxies. In this process, the increased mass concentration generates strong inner Lindblad-resonances which suppress bar formation. This begs the question of what causes the differences in central concentration. The toroidal galaxy's initial fields peak at the center and are purely azimuthal, meaning magnetic tension acts strongly in the radial direction, preventing inflows. The results from Whittingham et al. (2023) showed that magnetic fields stabilized against bar formation in galaxies both with azimuthal and non-azimuthal dominated fields. However, in our case we see azimuthal fields result in bar formation, while uniform and dipole fields stabilize against it. Another possibility is that the vertical fields in the dipole and uniform cases cause magnetic braking which drives mass inwards.

4.3.2 Magnetic field Evolution

We now examine the evolution of the fields during the simulations. Figure 4.9 shows the total magnetic energy vs. time in each simulation. Values are calculated by summing the total magnetic energy in the simulations domain. The toroidal galaxy shows fast initial growth, followed by large-scale dynamo growth after t=500 Myr, as reported in Robinson et al. (2025). The initial saturation at t=200 Myr is at a level a factor of five higher than the dipole and uniform galaxies. They do not saturate until t=500 Myr, and show no large-scale dynamo at late times. The fact that they saturate at lower total energies means that the central star formation may be linked to higher saturation levels. The dipole and uniform galaxies converge to similar saturation levels despite having over an order of magnitude difference in their initial energies.

To examine the effect of the bar on the total energy evolution, Figure 4.9 also plots the total energy excluding the central 3 kpc (dashed line). This shows that the late time growth in the toroidal case is mostly contained to the central 3 kpc, near the bar. Outside of 3 kpc, all three galaxies behave similarly, there is some growth from t=500-1000 Myr, but with long growth timescales. The dynamo of Robinson et al. (2025) depended on non-axisymmetric features driving radial flows. These results shows the

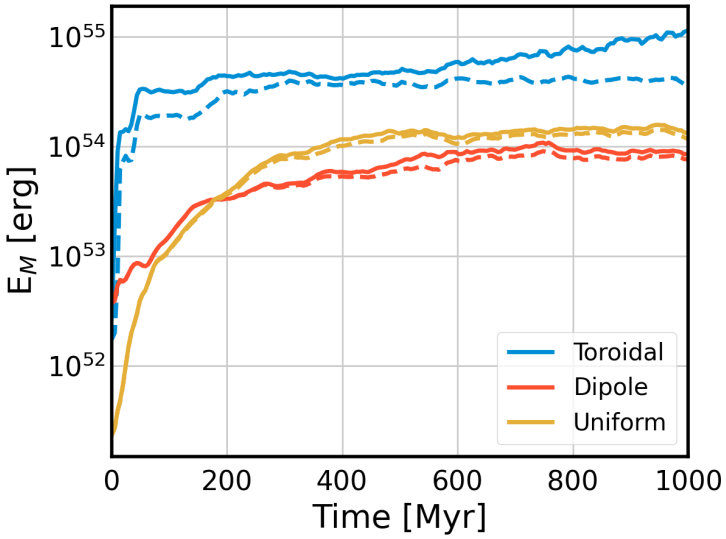

FIGURE 4.9: Total magnetic energy evolution in each galaxy. Magnetic energy saturates in the dipole and uniform after 600 Myr. The toroidal galaxy initially saturates at 200 Myr, but continued dynamo growth begins around t=500 Myr. Dashed lines show the total energy excluding the central 3 kpc.

bar plays a major role in that mechanism, likely because is has shorter timescales than spirals, and is centrally concentrated.

The evolution of the cylindrical components of the magnetic field can be seen in Figure 4.10, which plots their total angle-averaged power spectrum. In each galaxy, each component grows throughout the 1 Gyr of evolution, but there is subtle differences. The toroidal galaxy has stronger fields overall, but has a flat spectrum at large scales in its azimuthal fields, which the dipole uniform galaxies do not. This excess power at large scales is evidence that the initial fields have not been erased in the toroidal galaxy. All three galaxies have more power in their z-component than in their radial component. This contradiction with the weaker z-fields in Figure 4.6 is because the calculation of the power spectrum was in a cube region that contains gas in the CGM above the disk, which means the fields in the CGM are preferentially oriented in the z-direction. The uniform galaxy shows increased power at large scales in its z-component than the dipole case, which means some remnants of the original seed field may still remain in the CGM.

Additionally, none of the galaxies have continually diminishing power in the r-component as seen in the no-spiral model of Robinson et al. (2025), which confirms the spirals sustain

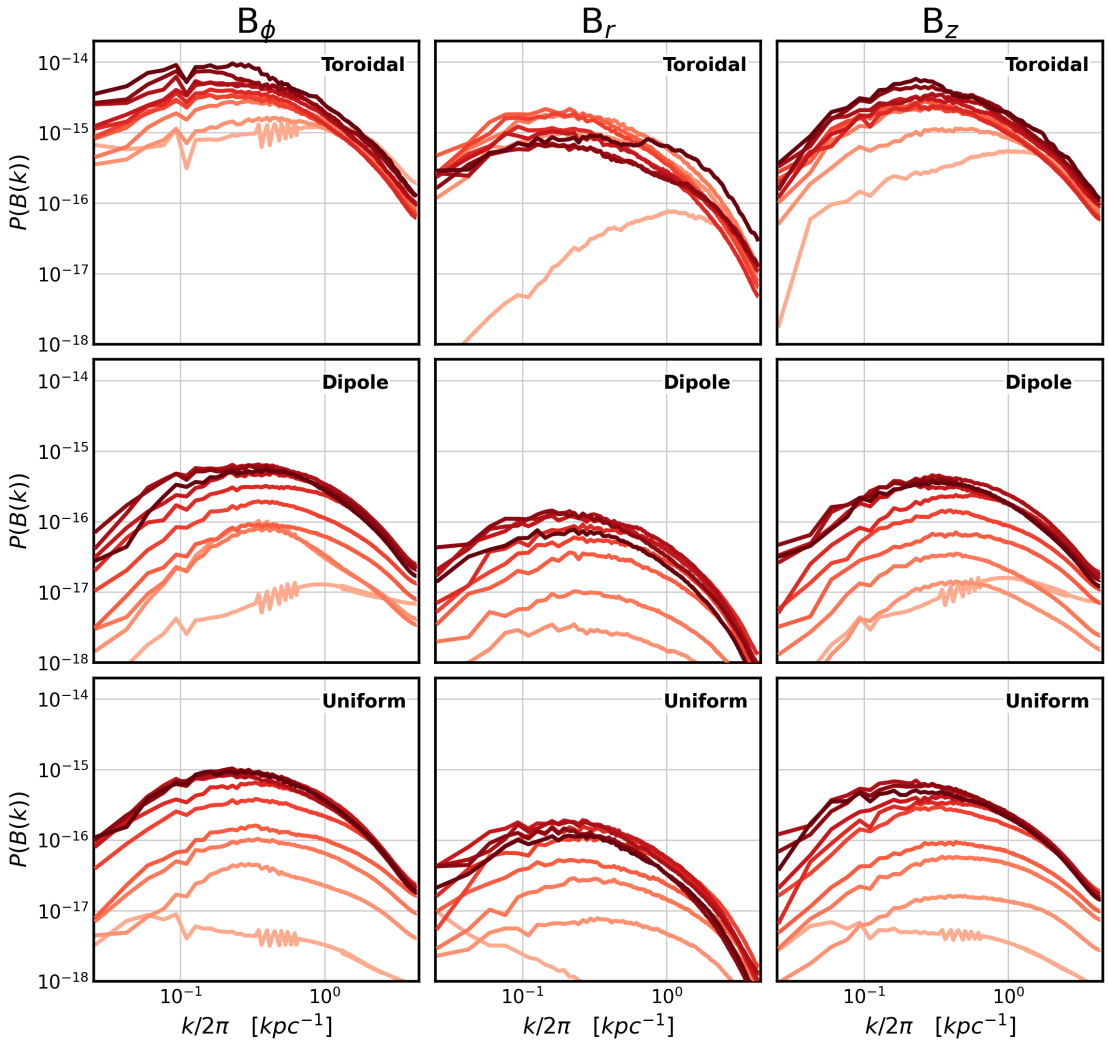

FIGURE 4.10: Fourier power spectra of the azimuthal, radial, and vertical field components in each galaxy over time. Power spectra are calculated in a cube of side-length 9.375 kpc centered on the galaxy. Each line shows a different time, going from 50 Myr (light shaded) to 1050 Myr (dark shaded)

the radial fields as they are sheared out by differential rotation.

4.3.3 Final Magnetic Configuration

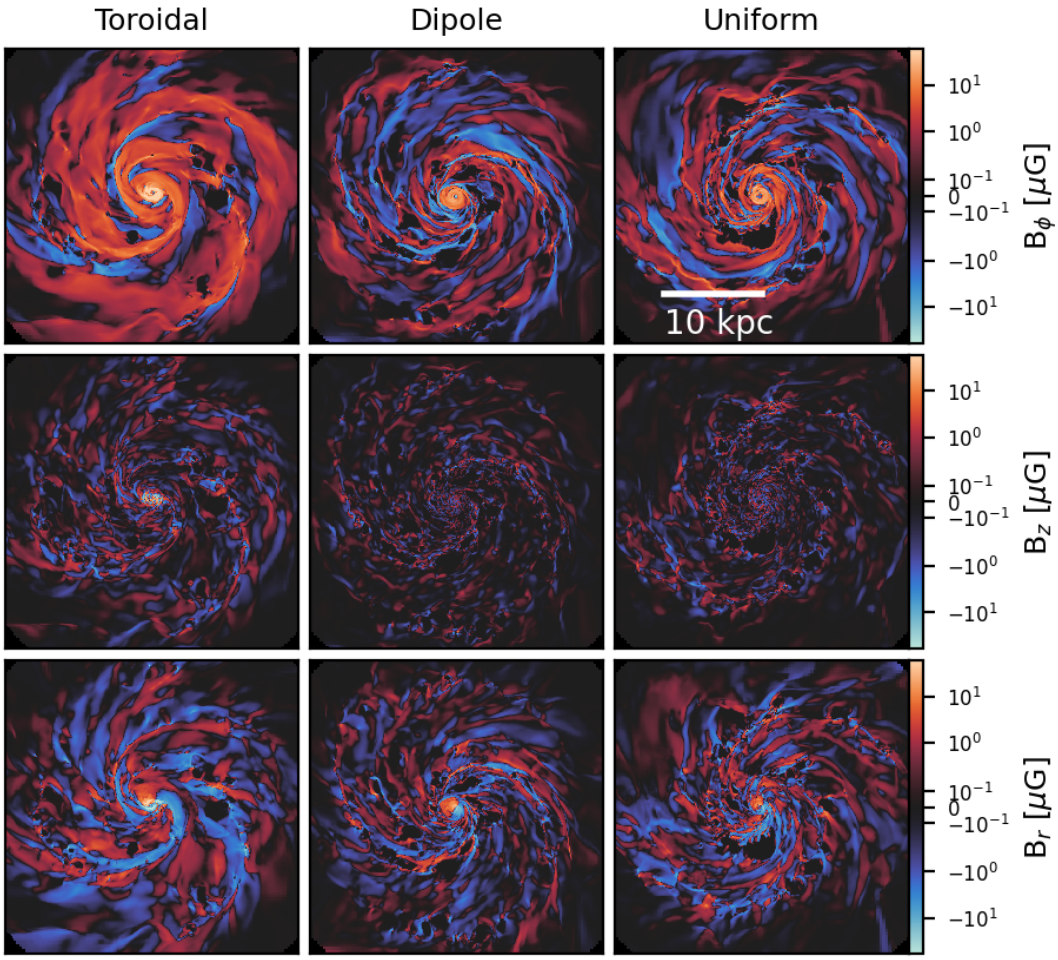

FIGURE 4.11: Projections of azimuthal (top row), vertical (middle row), and radial (bottom row) magnetic field components, of the final magnetic field configuration at t=1 Gyr.

We now examine the final morphologies of the fields, to determine which of the galaxies produce fields similar to those observed in galaxies. There are three major observational results to compare to: magnetic spirals in the plane of the disk, field reversals in the plane of the disk, and x-shaped fields in the CGM (Van Eck et al.; 2011; Beck; 2015a; Krause et al.; 2020).

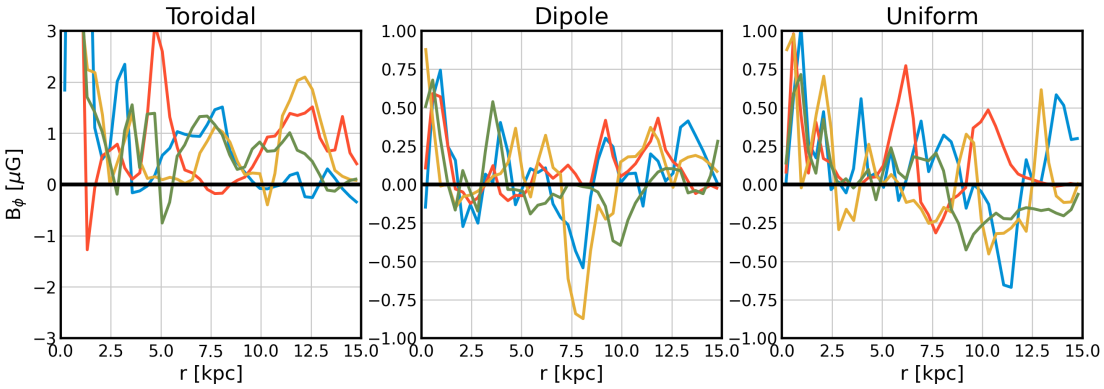

FIGURE 4.12: B_ϕ vs. r for each model at t=1 Gyr. Each line represents a wedge region spanning $\pi/8$ radians. In the toroidal galaxy, the fields are primarily aligned in the positive direction, which is the same direction as in the initial condition.

Face-on visualizations of the three cylindrical components at t=1 Gyr are shown in Figure 4.11. The upper left panel clearly shows the strong azimuthal fields that were generated in the toroidal galaxy, along with strong radial fields, both associated with spiral arms. The toroidal galaxy also shows minimal field reversals compared to the dipole and uniform galaxies. This is shown further in Figure 4.12, which plots the volume-averaged azimuthal field strength as a function of radius in each galaxy. Because the field reversals are non-axisymmetric, each line shows the radial profile of a wedge region corresponding to $\pi/8$ radians. The azimuthal field in the toroidal galaxy is clearly biased towards the positive direction, even after 1 Gyr of evolution. The uniform and dipole galaxy have fields in both the positive and negative ϕ direction, and show at least two major reversals per wedge.

All of the models produce magnetic spirals, and we show an example of the fields in the x-y plane in Figure 4.13. To the eye, all three cases appear, so we show a single visualization and quantify differences between each case in the following figure. The magnetic fields can be seen aligning with the spiral arms on average, with local excursions near feedback events. To compare the magnetic pitch angles to those of the density spirals, we calculate the pitch angle α of both the magnetic fields and the density gradients. The pitch angle is defined as the angle between each vector and a line tangent to a circle at its given radius. For the density spirals, we use the angle perpendicular to the density gradient (rotated by 90 degrees), which gives the direction parallel to density contours, which run along the spiral arms. We calculate both pitch angles on a pixel by pixel basis, and plot histograms of the pitch angles in Figure 4.14. Because observations

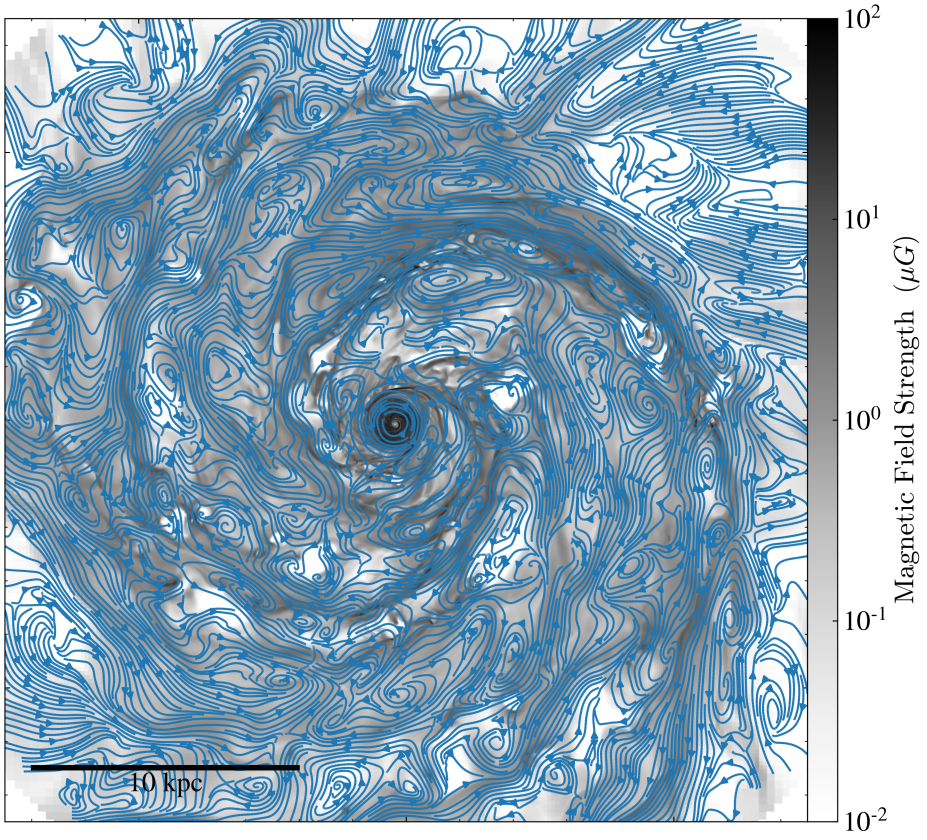

FIGURE 4.13: Face-on visualization of magnetic fields in the dipole galaxy at t=1 Gyr. Greyscale shows a mass-weighted average total magnetic field strength, and streamlines show the morphology of the field in the x-y plane. The magnetic fields largely trace out the spiral arms, with local excursions.

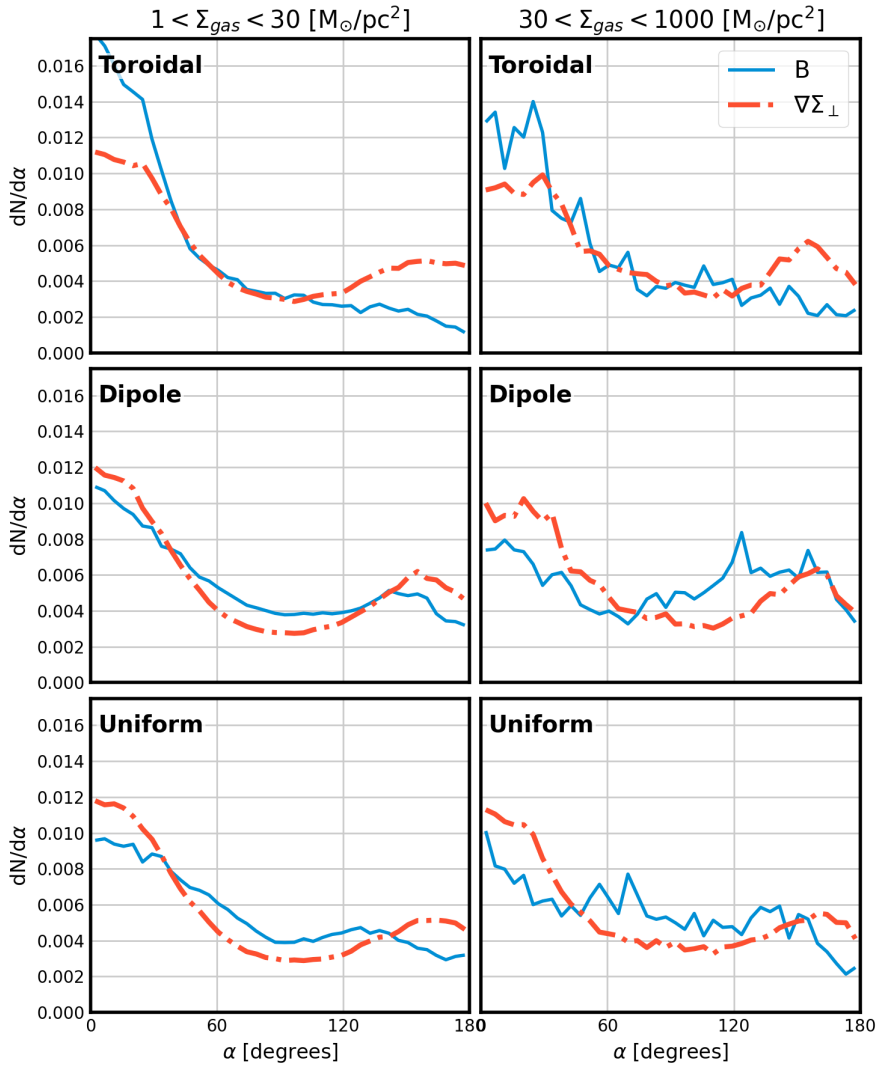

FIGURE 4.14: Histogram of pitch angle α for all three models in surface densities correpsonding to interarm regions (left panels), and arm regions (right panels). Calculated on volume-weighted average magnetic fields along the z-axis of a 9.15 pc resolution grid. $\nabla\Sigma_\perp$ is the vector perpendicular to the surface-density gradient, which was calculated with a 3x3 kernel on the same grid.

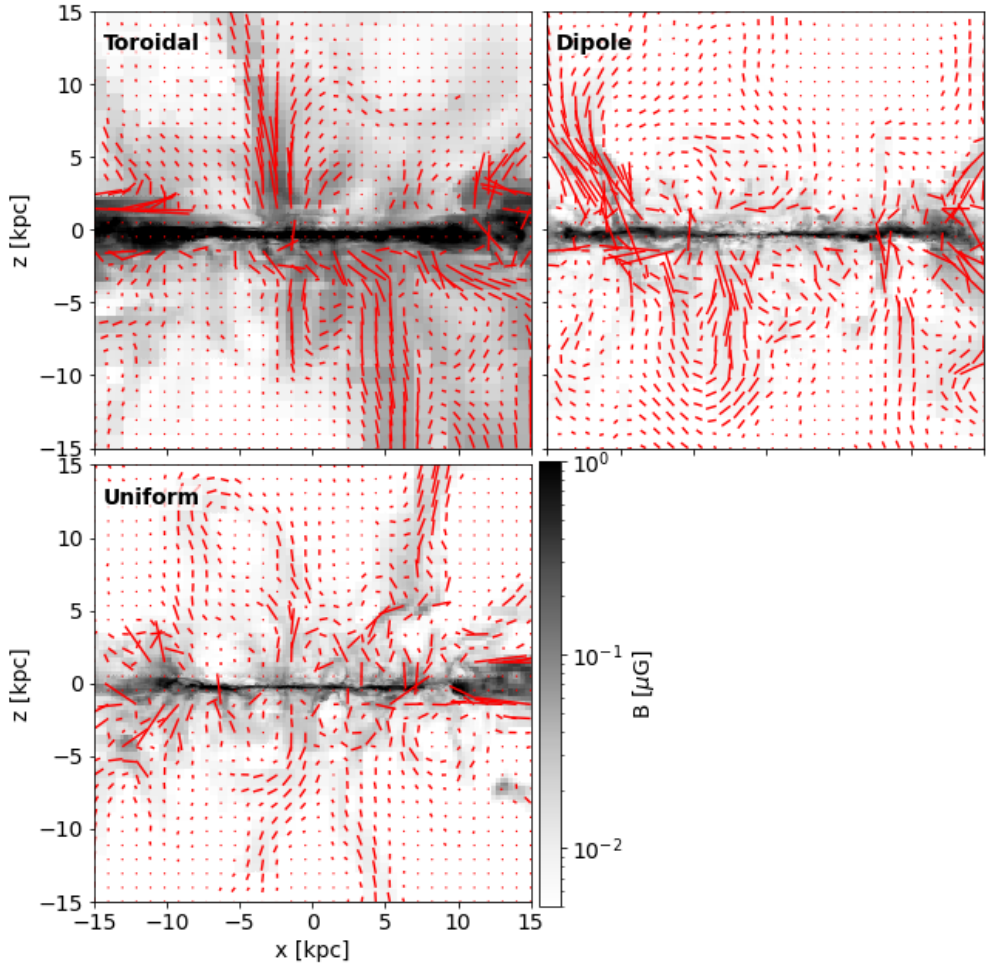

FIGURE 4.15: Edge-on view of the magnetic fields in each galaxy at t=1Gyr. Greyscale shows a volume-average magnetic field strength along the y-axis, and red lines show the directions of the field. The lines within the central 1 kpc are omitted.

show differences between magnetic pitch angle patterns within spiral arms and interarm regions (Beck; 2015a), we separate the histograms into surface densities corresponding to those regions. We define interarm regions as those in the surface density region $1 < \Sigma_{gas} < 30$, and arm regions as those in the range $30 < \Sigma_{gas} < 1000$, where Σ_{gas} is in units of $M_{\odot}/\mathrm{pc}^2$. On this plot, spirals appear as peaks in the pitch angle distribution. The density spirals show a peak from 0-20 degrees in all cases, which we interpret as a spiral arm with a pitch angle of 10 degrees. There is a corresponding peak at 170 degrees in each case. In the interarm regions, magnetic spirals match the density spiral distribution more closely than within the spiral arms. The magnetic spirals in the dipole and uniform galaxies show a preference towards 90 degrees, and the toroidal galaxy has a preference to more tightly wound magnetic spirals. Within the arms, the signals become noisier as local feedback events and self-gravitating regions have more complex structure. The toroidal galaxy still has a preference towards being more tightly wound, but overall the magnetic spirals have weaker signals in the arm regions. This is consistent with observations that show the strongest magnetic spirals in interarm regions.

The magnetic fields extending above the disk are seen in Figure 4.15, which shows magnetic field strengths volume average along the y-axis, and the directions of the field in the x-z plane. The toroidal galaxy produces the strongest fields in the CGM, as the strongly magnetized ISM gas is launched in outflows. The uniform galaxy clearly shows an x-shaped field, and the toroidal galaxy shows one as well. The dipole galaxy does not. In all cases, the magnetic fields in the CGM run parallel to density structures, meaning the fields are likely dragged upwards in outflows.

4.4 Discussion and Conclusions

In this work, we have investigated the role of initial magnetic field configurations in isolated galaxy simulations. Our results demonstrate that the morphology and strength of the initial field can influence the subsequent dynamical evolution of the system. In particular, the toroidal field geometry had stronger initial magnetic fields in the galactic center, which led to the formation of a central bar. The toroidal case ended with more magnetic energy overall, due to additional dynamo action driven by the bar instability, and centrally concentrated star formation. In contrast, galaxies initialized with dipole and uniform fields contained less magnetic energy overall and evolved toward lower, but similar, saturation levels. This convergence suggests that the magnetic state of those galaxies may be relatively robust to substantial variations in the initial conditions in the absence of bar formation.

Our results also indicate that bars and spirals affect dynamo growth in distinct ways. The radial magnetic fields are sustained in both the barred and spiral galaxies, compared to galaxies lacking such structures where they are efficiently sheared out (Robinson et al.; 2025). The sustaining of radial fields indicates large-scale dynamos may be active in the galaxies without bars, albeit with slower amplification rates. In the toroidal model that developed a bar, magnetic energy growth with e-folding timscales of ~ 600 Myr is confined to the inner few kiloparsecs, suggesting the bar plays a primary role. These results highlight the need to disentangle the relative roles of bars and spiral arms in large-scale dynamos.

Some of the simulations produce fields that match observational constraints. All three of them have density spirals with pitch angle distributions that peak at 10 degrees. The magnetic spirals in the uniform and dipole galaxies follow that distribution, but the toroidal galaxy produces preferentially lower pitch angles. The toroidal galaxy also produces fewer field reversals. The toroidal and uniform galaxy shows evidence of X-shaped fields in the CGM, while the dipole does not. Whether these results are consistent and reproducible remain to be seen. The use of observational results remains essential for developing predictive, physically grounded models of magnetic field evolution in galaxies.

Several open questions remain, such as how exactly the fields triggered the formation of the bar. Gravity likely provides the dominant torque, but as discussed in Whittingham et al. (2023), small changes in central concentrations of can trigger gravitational instabilities. There are two plausible explanations for the fields increasing the central concentration, either the strong azimuthal fields resist radial flows, triggering the bar instability, or the vertical fields drove the inflow through magnetic torques, thus stabilizing against bar instability. These scenarios could be tested with more initial configurations, for example: would weaker toroidal fields still trigger bar formation, or is there a threshold strength for such instabilities? There remain more questions as well, such as how sensitive are the saturation levels to details of the initial topology. More extensive parameter studies, including additional field morphologies are still required.

Bibliography

Agertz, O., Teyssier, R. and Moore, B. (2011). The formation of disc galaxies in a ΛCDM universe, **410**(2): 1391–1408.

Balbus, S. A. and Hawley, J. F. (1998). Instability, turbulence, and enhanced transport in accretion disks, *Reviews of Modern Physics* **70**(1): 1–53.

Beck, R. (2015a). Magnetic fields in spiral galaxies, **24**: 4.

Beck, R. (2015b). Magnetic fields in the nearby spiral galaxy IC 342: A multi-frequency radio polarization study, **578**: A93.

Beck, R., Berkhuijsen, E. M., Gießübel, R. and Mulcahy, D. D. (2020). Magnetic fields and cosmic rays in M 31. I. Spectral indices, scale lengths, Faraday rotation, and magnetic field pattern, **633**: A5.

Brandenburg, A. and Subramanian, K. (2005). Astrophysical magnetic fields and nonlinear dynamo theory, **417**(1-4): 1–209.

Butsky, I., Zrake, J., Kim, J.-h., Yang, H.-I. and Abel, T. (2017). Ab Initio Simulations of a Supernova-driven Galactic Dynamo in an Isolated Disk Galaxy, **843**(2): 113.

Evans, C. R. and Hawley, J. F. (1988). Simulation of Magnetohydrodynamic Flows: A Constrained Transport Model, **332**: 659.

Frick, P., Beck, R., Shukurov, A., Sokoloff, D., Ehle, M. and Kamphuis, J. (2000). Magnetic and optical spiral arms in the galaxy NGC 6946, **318**(3): 925–937.

Ghosh, S., Fragkoudi, F., Di Matteo, P. and Saha, K. (2023). Bars and boxy/peanut bulges in thin and thick discs. II. Can bars form in hot thick discs?, **674**: A128.

Hawley, J. F., Gammie, C. F. and Balbus, S. A. (1995). Local Three-dimensional Magnetohydrodynamic Simulations of Accretion Disks, **440**: 742.

Heitsch, F., Stone, J. M. and Hartmann, L. W. (2009). Effects of Magnetic Field Strength and Orientation on Molecular Cloud Formation, **695**(1): 248–258.

Hockney, R. W. and Eastwood, J. W. (1981). *Computer Simulation Using Particles*.

Kim, W.-T. and Stone, J. M. (2012). Two-dimensional Magnetohydrodynamic Simulations of Barred Galaxies, **751**(2): 124.

Körtgen, B., Banerjee, R., Pudritz, R. E. and Schmidt, W. (2019). Global dynamics of the interstellar medium in magnetized disc galaxies, **489**(4): 5004–5021.

Krause, M., Irwin, J., Schmidt, P., Stein, Y., Miskolczi, A., Carolina Mora-Partiarroyo, S., Wiegert, T., Beck, R., Stil, J. M., Heald, G., Li, J.-T., Damas-Segovia, A., Vargas, C. J., Rand, R. J., West, J., Walterbos, R. A. M., Dettmar, R.-J., English, J. and Woodfinden, A. (2020). CHANG-ES. XXII. Coherent magnetic fields in the halos of spiral galaxies, **639**: A112.

Kulsrud, R. M. (2005). *Plasma Physics for Astrophysics*.

Machida, M., Nakamura, K. E., Kudoh, T., Akahori, T., Sofue, Y. and Matsumoto, R. (2013). Dynamo Activities Driven by Magnetorotational Instability and the Parker Instability in Galactic Gaseous Disks, **764**(1): 81.

Martin-Alvarez, S., Slyz, A., Devriendt, J. and Gómez-Guijarro, C. (2020). How primordial magnetic fields shrink galaxies, **495**(4): 4475–4495.

Miyoshi, T. and Kusano, K. (2005). An MHD Simulation of the Magnetosphere Based on the HLLD Approximate Riemann Solver, *AGU Fall Meeting Abstracts*, Vol. 2005, pp. SM51B–1295.

Mocz, P., Burkhart, B., Hernquist, L., McKee, C. F. and Springel, V. (2017). Moving-mesh Simulations of Star-forming Cores in Magneto-gravo-turbulence, **838**(1): 40.

Ntormousi, E. (2018). Magnetic fields in massive spirals: The role of feedback and initial conditions, **619**: L5.

Ntormousi, E., Tassis, K., Del Sordo, F., Fragkoudi, F. and Pakmor, R. (2020). A dynamo amplifying the magnetic field of a Milky-Way-like galaxy, **641**: A165.

Pakmor, R., van de Voort, F., Bieri, R., Gómez, F. A., Grand, R. J. J., Guillet, T., Marinacci, F., Pfrommer, C., Simpson, C. M. and Springel, V. (2020). Magnetizing the circumgalactic medium of disc galaxies, **498**(3): 3125–3137.

Parker, E. N. (1979). *Cosmical magnetic fields. Their origin and their activity*.

Rieder, M. and Teyssier, R. (2016). A small-scale dynamo in feedback-dominated galaxies as the origin of cosmic magnetic fields - I. The kinematic phase, **457**(2): 1722–1738.

Rieder, M. and Teyssier, R. (2017a). A small-scale dynamo in feedback-dominated galaxies - II. The saturation phase and the final magnetic configuration, **471**(3): 2674–2686.

Rieder, M. and Teyssier, R. (2017b). A small-scale dynamo in feedback-dominated galaxies - III. Cosmological simulations, **472**(4): 4368–4373.

Robinson, H. and Wadsley, J. (2024). Regulating star formation in a magnetized disk galaxy, .

Robinson, H., Wadsley, J., Sellwood, J. A. and Pudritz, R. E. (2025). Star Formation and Magnetic Field Amplification due to Galactic Spirals, **989**(2): 205.

Smith, B. D., Bryan, G. L., Glover, S. C. O., Goldbaum, N. J., Turk, M. J., Regan, J., Wise, J. H., Schive, H.-Y., Abel, T., Emerick, A., O'Shea, B. W., Anninos, P., Hummels, C. B. and Khochfar, S. (2017). GRACKLE: a chemistry and cooling library for astrophysics, **466**(2): 2217–2234.

Stein, M., Kleimann, J., Adebahr, B., Dettmar, R. J., Fichtner, H., English, J., Heesen, V., Kamphuis, P., Irwin, J., Mele, C., Bomans, D. J., Li, J., Skeggs, N. B., Wang, Q. D. and Yang, Y. (2025). CHANG-ES: XXXIV. Magnetic field structure in edge-on galaxies: Characterising large-scale magnetic fields in galactic halos, **696**: A112.

Steinwandel, U. P., Dolag, K., Lesch, H., Moster, B. P., Burkert, A. and Prieto, A. (2020). On the origin of magnetic driven winds and the structure of the galactic dynamo in isolated galaxies, **494**(3): 4393–4412.

Teyssier, R. (2002). Cosmological hydrodynamics with adaptive mesh refinement. A new high resolution code called RAMSES, **385**: 337–364.

Van Eck, C. L., Brown, J. C., Stil, J. M., Rae, K., Mao, S. A., Gaensler, B. M., Shukurov, A., Taylor, A. R., Haverkorn, M., Kronberg, P. P. and McClure-Griffiths, N. M. (2011). Modeling the Magnetic Field in the Galactic Disk Using New Rotation Measure Observations from the Very Large Array, **728**(2): 97.

Weżgowiec, M., Ehle, M. and Beck, R. (2016). Hot gas and magnetic arms of NGC 6946: Indications for reconnection heating?, **585**: A3.

Whittingham, J., Sparre, M., Pfrommer, C. and Pakmor, R. (2023). The impact of magnetic fields on cosmological galaxy mergers - II. Modified angular momentum transport and feedback, **526**(1): 224–245.

Wibking, B. D. and Krumholz, M. R. (2023). The global structure of magnetic fields and gas in simulated Milky Way-analogue galaxies, **521**(4): 5972–5990.

Wissing, R. and Shen, S. (2023). Numerical dependencies of the galactic dynamo in isolated galaxies with SPH, **673**: A47.

Chapter 5

Summary and Future Work

In this thesis, we have studied the magnetic fields within spiral galaxies. We model the co-evolution of magnetic fields and star formation within isolated disk galaxies with a variety of different setups using the AMR code Ramses (Teyssier; 2002). Here we summarize and synthesize our work, and present ideas for future progress in this field.

Magnetic fields are now recognized as a fundamental component of galaxies, influencing star formation and gas dynamics across a wide range of scales. The theoretical framework for their evolution within galaxies is dynamo theory, with both small and large-scale dynamos driven by turbulence in the ISM. Observationally, there is widespread evidence for field strengths of 1-10 μG that are structured over 10 kpc scales, consistent with dynamo theory. Numerical simulations have become indispensable tools for bridging theory and observation by enabling controlled experiments on the role of magnetic fields in galaxy formation and evolution. Questions remain about the sensitivity of dynamo growth within the galactic environment, the detailed impact of magnetic fields in star formation, and the ability of simulations to produce fields reflective of those observed in nature. In each chapter of this thesis we answered some of those questions.

In Chapter 2, we simulated disk galaxies based on the Agora Isolated Galaxy (Kim et al.; 2016) with the addition of magnetic fields of varying strength. Here we focused on the combined role of magnetic fields and stellar feedback in limiting star formation to produce a self-regulating ISM. We showed that magnetic fields can increase the disk thickness, limit the size of superbubbles, contribute to the stability of the gas disk, and consequently reduce star formation rates. Increasing the strength of the initial fields decreased the overall star formation rates accordingly. We also saw evidence for dynamo amplification that primarily occurred in the warm-phase ISM. We concluded that beginning with weak fields allows the galaxy to produce a realistic steady-state ISM where fields contribute significantly to the overall support, while beginning with strong

fields ($B > 1$ μG at $n \sim 1$ cm^{-3}) locked the galaxy into unrealistic field configurations that are set by the initial conditions.

In Chapter 3, we varied the structure of the galactic disk rather than the magnetic fields, by simulating a galaxy with and without spiral arms. This requires a new initial condition with a heavier stellar disk that is unstable to forming spirals. These simulations were analyzed with an emphasis on the interplay between spiral arms and dynamo amplification. The spiral arms gathered gas into high surface density regions, causing the SFR to increase by a factor of 2.6 in the spiral galaxy. The extra star formation caused the small-scale dynamo to be more effective and the fields saturated at higher levels, resulting in volume-weighted averages of 1 μG. We also saw evidence of a slower, large-scale dynamo in the spiral galaxy, with an exponential growth (e-folding time) of 600 Myr. We presented a novel large-scale dynamo mechanism in which the radial fields generated by non-axisymmetric features power the amplification. The mean-fields that were generated tended to align with the spiral arms and were coherent on scales of up to 10 kpc.

In Chapter 4 we varied the initial morphology of the fields. We compared cases with uniform, dipolar, and toroidal fields. The previous chapters had all assumed a toroidal morphology. We found that the toroidal case formed of a central bar, which in turn enhanced magnetic amplification. The dipole and uniform configurations did not form a bar, but converged toward similar but lower saturation levels, suggesting a degree of insensitivity to the initial conditions when bar formation does not occur. We also compared the morphologies of the fields after 1 Gyr of evolution to those seen in observations of real galaxies. All three models produce magnetic spirals with pitch angle distributions peaking near 10 degrees, but the toroidal model produced slightly lower pitch angles. More detailed analysis is required to determine the exact interplay between non-axisymmetric structure, magnetic fields, and angular momentum transport. An important question that remains is how exactly did the magnetic fields cause the formation of the bar? It could either be that strong azimuthal fields inhibit any radial flows causing the bar instability, or the vertical fields redistributed mass through magnetic torques, thus stabilizing against instability.

Taken together, this thesis demonstrates that magnetic fields are deeply intertwined with the dynamical state and morphology of galaxies. Not only do they play a pivotal role in the determining the star formation rates and distributions, they can influence the distribution of gas density, the size of superbubbles, and affect large-scale galaxy morphology.

We showed evidence for both small and large scale dynamos in our simulations. While the small-scale dynamo behaviour is quite robust, there remains uncertainty in modeling large-scale dynamos. Our models did not show evidence of the classical $\alpha\Omega$ dynamo being active, but rather a mechanism that depended on non-axisymmetric bars and spirals that produce faster growth rates. Spiral driven dynamos therefore have the potential to explain observations of ordered fields in young galaxies Geach et al. (2023). However, they lack analytical theories that predict their behaviour. There is some similarities between these dynamos and the spiral-driven GI dynamo that has been applied in accretion disks Riols and Latter (2019), which shows a promising angle to study them. However that exact mechanism is unlikely to be active in galaxies due to its low R_M regime.

There are some caveats that apply to all of our work. For one, there is physics relevant to galaxy evolution that our simulations do not include. One that is directly relevant is cosmic rays, whose dynamics are closely tied to those of magnetic fields. Cosmic rays can contribute significantly to gas support (Semenov et al.; 2021), and their dynamics can back-react onto the evolution of magnetic fields as well. There still remains uncertainty regarding cosmic rays, especially concerning how to include them in galaxy simulations, but they would be an interesting future direction.

A common theme in all of this work was the design of the initial conditions. We conducted three separate studies that altered the initial field strengths, field morphologies, and the spiral arms within the disk. Combining the results from each gives us insight into how to design optimal simulations going forwards. Most importantly, we caution against using fields that are too strong initially. Results from both Chapter 2 and 4 show that initially strong fields can bias the final outcome. The primary argument for using strong initial fields is so that they quickly reach strengths near those observed in real galaxies, since isolated galaxy simulations are meant to approximate an evolved state from the beginning. However, non-ideal MHD cannot effectively dissipate energy, making it possible to over-saturate the initial fields.

There are several interesting avenues for future work that address the constraints of isolated galaxy simulations. All of our simulations have a time limit of about $\sim$1 Gyr, because after that a substantial fraction of gas in the disk has been consumed. A possible solution to this problem is a stellar feedback model that redistributes mass back into the ISM. This would need to be designed in such a way that the gas is returned smoothly throughout the ISM and does not cause runaway star formation. With such a method, the simulations could be run for much longer which would allow starting with

significantly weaker seed fields, and also allow for large-scale dynamos to fully develop. While this method would technically break mass-conservation, it would approximate smooth inflows of gas into galaxies which in reality, build up their mass over time.

Another interesting direction would be to study the role of galactic environment. All of our simulations were perfectly isolated galaxies, but it is of interest how magnetic fields affect galaxies in denser environments too. One approach is to put the isolated galaxy setup into a wind-tunnel, which approximates the galaxy falling into a hot inter-cluster medium. This would allow for the study of magnetic fields in different environments, while also providing an inflow of gas to sustain star formation in the disk. There has been some recent progress in this direction by Lee et al. (2025), who showed magnetized ICM winds can strip gas from the disk more effectively than winds without magnetic fields, aiding in the creation of so-called jellyfish galaxies. Even without wind tunnels, the CGM is a region to refine in isolated galaxies simulations. Our models do not include any material in the CGM initially which does not reflect the reality of most galaxies, and it would be interesting to study magnetic effects in that environment too.

A final interesting direction is to go down in scale. There remain many questions as to how magnetic fields affect cloud and bubble scale properties. Zhao et al. (2024) used simulations similar to ours, but with a novel-zoom in method that allowed characterization of a wide-range smaller scale ISM properties, while being informed by the large-scale galactic fields and dynamics. It would be interesting to use methods such as these to investigate the effect of magnetic fields in bubble and cloud populations. With the advent of JWST there is now detailed superbubble populations that could be compared against Watkins et al. (2023). The upcoming Square Kilometer Array will be able to characterize magnetic fields in galaxies with unprecedented resolution, allowing for further comparison against high-resolution simulations.

Bibliography

Geach, J. E., Lopez-Rodriguez, E., Doherty, M. J., Chen, J., Ivison, R. J., Bendo, G. J., Dye, S. and Coppin, K. E. K. (2023). Polarized thermal emission from dust in a galaxy at redshift 2.6, *arXiv e-prints* p. arXiv:2309.02034.

Kim, J.-h., Agertz, O., Teyssier, R., Butler, M. J., Ceverino, D., Choi, J.-H., Feldmann, R., Keller, B. W., Lupi, A., Quinn, T., Revaz, Y., Wallace, S., Gnedin, N. Y., Leitner, S. N., Shen, S., Smith, B. D., Thompson, R., Turk, M. J., Abel, T., Arraki, K. S., Benincasa, S. M., Chakrabarti, S., DeGraf, C., Dekel, A., Goldbaum, N. J., Hopkins,

P. F., Hummels, C. B., Klypin, A., Li, H., Madau, P., Mandelker, N., Mayer, L., Nagamine, K., Nickerson, S., O'Shea, B. W., Primack, J. R., Roca-Fàbrega, S., Semenov, V., Shimizu, I., Simpson, C. M., Todoroki, K., Wadsley, J. W., Wise, J. H. and AGORA Collaboration (2016). The AGORA High-resolution Galaxy Simulations Comparison Project. II. Isolated Disk Test, **833**(2): 202.

Lee, J., Kimm, T., Blaizot, J., Devriendt, J., Martin-Alvarez, S., Rhee, J., Rey, M. and Slyz, A. (2025). Jellyfish Galaxies in Magnetic Fields: Insights from Numerical Simulations, *arXiv e-prints* p. arXiv:2507.03127.

Riols, A. and Latter, H. (2019). Gravitoturbulent dynamos in astrophysical discs, **482**(3): 3989–4008.

Semenov, V. A., Kravtsov, A. V. and Caprioli, D. (2021). Cosmic-Ray Diffusion Suppression in Star-forming Regions Inhibits Clump Formation in Gas-rich Galaxies, **910**(2): 126.

Teyssier, R. (2002). Cosmological hydrodynamics with adaptive mesh refinement. A new high resolution code called RAMSES, **385**: 337–364.

Watkins, E. J., Barnes, A. T., Henny, K., Kim, H., Kreckel, K., Meidt, S. E., Klessen, R. S., Glover, S. C. O., Williams, T. G., Keller, B. W., Leroy, A. K., Rosolowsky, E., Lee, J. C., Anand, G. S., Belfiore, F., Bigiel, F., Blanc, G. A., Boquien, M., Cao, Y., Chandar, R., Chen, N. M., Chevance, M., Congiu, E., Dale, D. A., Deger, S., Egorov, O. V., Emsellem, E., Faesi, C. M., Grasha, K., Groves, B., Hassani, H., Henshaw, J. D., Herrera, C., Hughes, A., Jeffreson, S., Jiménez-Donaire, M. J., Koch, E. W., Kruijssen, J. M. D., Larson, K. L., Liu, D., Lopez, L. A., Pessa, I., Pety, J., Querejeta, M., Saito, T., Sandstrom, K., Scheuermann, F., Schinnerer, E., Sormani, M. C., Stuber, S. K., Thilker, D. A., Usero, A. and Whitmore, B. C. (2023). PHANGS-JWST First Results: A Statistical View on Bubble Evolution in NGC 628, **944**(2): L24.

Zhao, M., Zhou, J., Baan, W. A., Hu, Y., Lazarian, A., Tang, X., Esimbek, J., He, Y., Li, D., Ji, W., Chang, Z. and Tursun, K. (2024). Magnetic Field of Molecular Gas Measured with the Velocity Gradient Technique. II. Curved Magnetic Field in kpc-scale Bubble of NGC 628, **967**(1): 18.